Università degli studi di Ferrara

Dottorato di Ricerca in
"FISICA"
ciclo xxvii
Coordinatore Prof. Vincenzo Guidi

Raindrop Size Distribution variability from high resolution disdrometer networks

Settore Scientifico Disciplinare: FIS/06

Dottorando:
Dott. Leo Pio D'Adderio

Tutore:
Dott. Federico Porcú
Dott. Ali Tokay

Anni 2012/2014

Contents

Introduction **v**

1 The Drop Size Distribution (DSD) **1**

1.1 The precipitation formation 3

1.1.1 Cloud particles formation 3

1.1.2 Cloud particles interactions 7

1.1.3 The rain drop formation mechanisms 9

1.2 The collisional break-up 14

1.3 The equilibrium drop size distribution (ED) 19

1.4 The DSD parameterization 24

1.5 DSD and radar parameters 28

1.6 DSD Variability 31

2 Instrumentation and field campaigns **37**

2.1 Instruments overview 38

2.2 Instruments description 41

2.2.1 Pludix 41

2.2.2 2DVD 50

2.2.3 Particle Size Velocity disdrometer (Parsivel) 53

2.2.4 Micro Rain Radar (MRR) 57
2.2.5 Joss-Waldvogel (JW) 60
2.3 Field campaigns 61

3 Collisional Break-up: detection and analysis 69
3.1 Pludix power spectrum 70
3.2 Break-up detection algorithms 71
3.2.1 Power Spectrum (PS) algorithm 72
3.2.2 DSD Spectrum (DS) algorithm 74
3.3 Dependence of collisional break-up on altitude 75
3.3.1 PS algorithm: results 82
3.3.2 CKE limiting value 84
3.3.3 DS algorithm: results 86
3.4 Break-up: case studies 89

4 Collisional Break-up and Equilibrium DSD 95
4.1 SLOPE algorithm 96
4.1.1 SLOPE algorithm: 2DVD results 98
4.1.2 SLOPE algorithm: Parsivel results 103
4.2 Evaluation of gamma fit 105
4.3 Integral rain and DSD parameters 108

5 Small scale DSD spatial variability 115
5.1 Methodology 116
5.2 Results: Wallops dataset 118
5.2.1 Dataset description 118
5.2.2 Correlation distance analysis 124

5.2.3 Sensitivity Studies - Partial beam filling 135
5.3 Results: MC3E dataset 137
5.3.1 Dataset description 137
5.3.2 Correlation distance analysis 142
5.3.3 Sensitivity Studies - Partial beam filling 148

Conclusions and Outlooks **151**

Acknowledgments **155**

Bibliography **157**

Introduction

The characteristics of the raindrop size distribution (DSD) have been widely studied since Marshall and Palmer (1948) introduced specific version of exponential distribution for the observed size spectra, based on Marshall et al. (1947) measurements of raindrops records on dyed filter papers. Across the decades, interest in measuring and studying rain DSD has grown due to applications in cloud physics studies, in calibration of space-borne and ground-based microwave active precipitation sensors and in soil science and agriculture. Fernandez-Raga et al. (2011) show that since 1963, there has been an increase in the number of articles published on disdrometers, which in the last 20 years triplicated in number with respect to the previous decade.

The study of DSD and of the processes that determine it, are always been challenging from both theoretical and experimental point of view: experimental difficulties are, from one side, due to the impossibility to fully reproduce the cloud environment in laboratory, and to collect high quality and consistent measurements in natural rain. Even if many projects addressing different aspects of the DSD have been carried out, the data collected by disdrometer networks are very limited, due to the difficulties (logistic and economic) in the management of such networks. In the last years, the Atmospheric Physics group of the University of Ferrara took part in several experimental projects and collaborations that made available a large, high quality disdrometric data amount.

In particular, the participation to the CEOP-AEGIS project and the collaboration with NASA, in the frame of GPM mission GV program, supplied unprecedented disdrometric datasets for both number of installed instrument and for their geographic position. Based on this unprecedented dataset, this Thesis work aims to contribute in characterize, from a microphysical point of view, the precipitation structure and the processes that generate it. In particular, the vertical and horizontal DSD variability is analyzed, starting from the study of effects on the DSD of the collisional break-up mechanism in natural rain. The signature of collisional break-up, first evidenced by particular shape of Doppler power spectrum of a microwave disdrometer, is then searched and characterized in DSD spectrum, assessing its variability with altitude. The horizontal variability of DSD is studied both analyzing the occurrence of equilibrium DSD among the different datasets available and evaluating the correlation of integral and non-integral DSD parameters at small scale.

Chapter 1 gives an overview on past and recent studies on different aspects of DSD, from the main mechanisms that govern the rain development (both from experimental and theoretical/laboratory point of view) to its parameterization up to the DSD variability in natural rain.

Chapter 2 describes the characteristics of instruments, of the field campaigns and of the data used in the Thesis.

Chapter 3 analyzes the signature of collisional break-up both on the Pludix Doppler power spectrum and on DSD spectrum. The analysis is carried out developing two algorithms, that detect the collisional break-up as well as estimate the break-up diameter as function of altitude. In this chapter the evolution of rain events highlighting the development of break-up up to the reaching of equilibrium DSD is also shown.

In the chapter 4 the analysis is focused on the 2DVD DSD properties to evaluate the occurrence of equilibrium DSD in natural rain. Another algorithm, based on 2DVD

characteristics, is set up to automatically detect the equilibrium DSD. The results are also analyzed to estimate the goodness of fitting of the equilibrium DSD by a three parameter gamma distribution. The behavior of the integral rain parameters is studied as function of break-up occurrence.

In the chapter 5 the data collected from two disdrometric dataset are used to study the horizontal DSD spatial variability at small scale. The size of the measuring fields are comparable with a ground radar pixel or satellite footprint. The rainfall rate and other DSD parameters are analyzed using a three parameter exponential function to estimate their correlation at small scale.

In the last section the conclusions about this Thesis are reported.

Chapter 1

The Drop Size Distribution (DSD)

The knowledge of Particle Size Distribution (PSD) is of fundamental importance for the study of cloud and precipitation microphysics. The hydrometeors of different phase and shape within a cloud or a precipitation layer, are characterized by a peculiar PSD , which is the results of the physical processes that originated their formation. In this Thesis the liquid phase of precipitation has been analyzed with particular interest to the properties and characteristics of Drop Size Distribution (DSD). The DSD, often indicated as $N(D)$, is defined as the number of drops as function of drop diameter and it is usually referred to unitary volume, and generally its unit of measure is $m^{-3}mm^{-1}$, that is, the number of drops per cubic meter per millimeter diameter interval.

Even if the intensity and the amount of a rainfall episode are the most relevant parameters in most of the applications, from the physical point of view the property that best characterizes the rainfall is the DSD. The DSD is the starting point to calculate all the parameters that characterize a precipitation episode (i.e. the DSD integral parameters, such as rainfall rate, liquid water content, reflectivity, drops kinetic energy, etc...) that have many practical applications, and are strongly correlated to the precipitation for-

mation processes and the cloud structure.

Interest in DSD has developed sporadically through the years since about 1895 (Weisner,1895), while the main mechanisms responsible of precipitation formation have been studied since the late 1940's when Marshall and Palmer (1948) were the first to quantitatively measure the DSD from natural rain. They found that the distribution of number of drops as function of drop size was roughly exponential (Figure 1.1).

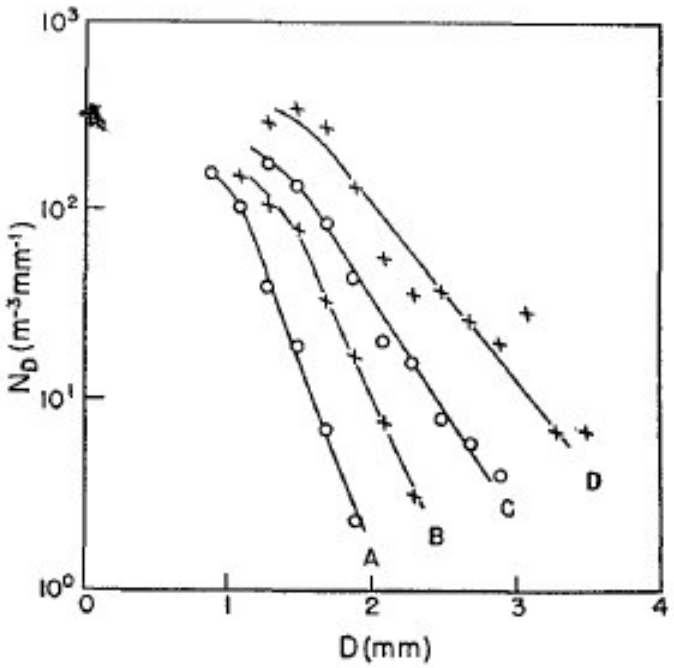

Figure 1.1: DSD measured by Marshall and Palmer (1948).

This chapter gives an overview on past studies on different aspects of DSD, from the main mechanisms that govern the rain development (both from experimental and theoretical/laboratory point of view) to its parameterization up to the DSD variability in natural rain.

1.1 The precipitation formation

1.1.1 Cloud particles formation

To understand how the processes involved in the rain formation can modify the DSD, it is important to have an overview of the mechanisms involved in the cloud development that define the microphysical properties of the cloud. Since the aim of this Thesis is the study of the characteristics of raindrops population, regardless the cloud type from which they were formed, only the main cloud properties will be discuss here.
Since the clouds can be made by particles in ice or liquid phase, there can be two different processes that lead to the cloud formation:

- condensation of water vapor;
- direct formation of ice crystals by water vapor sublimation.

Here, we are interested to analyze the processes that lead a population of water/ice particle to evolve in rain. A cloud is formed when warm/moist air is raised above the *Lifted Condensation Level (LCL)*, where the water vapor becomes saturated and, in presence of a suitable aerosol population, the two above processes can start. A first, basic classification of cloud structure can be done according the vertical velocity of the raising air. Generally, a cloud with higher speed of the vertical air motion has a deeper vertical development, while a cloud with lower values has a less vertical development. Both cloud types can overpass the freezing level (0°C level) and are usually formed by particles both in solid and in liquid phase. It can be remarked that this statement is referred to mid-latitude clouds, since the data used for this Thesis were collected at the mid-latitude; while, for example, the clouds in the tropics usually have a deeper vertical development and can also be made up by particle in liquid phase only. However, example of clouds formed by just one particles phase are found also at mid-latitude, like

the cirrus (high and thin clouds composed by ice crystals) or the fair weather cumulus (clouds composed by particle in liquid phase only). Regardless if clouds are formed by particles in liquid or solid phase, at the first stage of the cloud development they are both characterized by diffusive growth.

The cloud development processes occur in supersaturated air (the saturation is defined as the ratio between the water vapor pressure and the saturated vapor pressure over a plane surface of water) and are characterized by a transition phase, that is possible if the nucleation takes place. The nucleation can be homogeneous if the transition phase occur inside a pure substance, water vapor in this case, otherwise if the water vapor contains aerosol particles the nucleation is called heterogeneous. The rate of formation of drops deriving from the nucleation process is the nucleation rate.

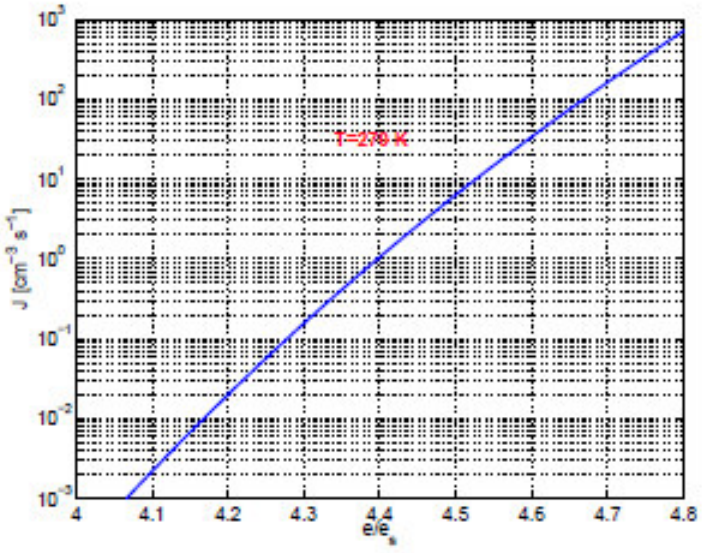

Figure 1.2: Nucleation rate as function of the saturation ratio for a temperature T=270 K (Prodi and Battaglia, 2002).

The figure 1.2 reports the nucleation rate as function of the saturation value calculated for a temperature T=270 K. The nucleation rate increases from undetectably

small values to extremely large values over a very narrow range of saturation values. The saturation value at which this rise occurs is in the range of 4-5, thus the air must be supersaturated by 300-400% for a drop of pure water to be nucleated homogeneously. Since saturation in the atmosphere seldom exceeds 100%, one concludes that homogeneous nucleation of water drops plays no role in natural clouds.

Homogeneous nucleation of ice from the liquid phase is analogous to nucleation of drops from the vapor phase. Theoretical and empirical results indicate that homogeneous nucleation of liquid water occurs at temperatures lower than about -35 to -40°C, depending on the size of the drops. This threshold lies within the temperature range of natural clouds, which may have cloud-top temperatures below -80°C (Houze, 1993). It is therefore possible, in a natural cloud, to have unfrozen liquid, *supercooled* drops in the temperature range of 0°C to about -40°C, while any liquid drop freezes spontaneously by homogeneous nucleation below this temperature.

In principle, an ice particle may be nucleated directly from the vapor phase in the same manner as a drop. Theoretical estimates of the rate at which molecules in the vapor phase aggregate to form ice particles indicate, however, that nucleation occurs only at temperatures below -65°C and at supersaturations ∼1000%. Such high supersaturations do not occur in the atmosphere.

Heterogeneous nucleation, therefore, is the process whereby cloud drops actually form. If the surface tension between the water and the nucleating particle is relatively low, the nucleus is said to be wettable, and the water may form a spherical cap on the surface of the particle. A particle onto which the molecules collect in this manner is referred to as a*Cloud Condensation Nucleus* (CCN). Different particles type can be assumed as CCN and depending on their properties the nucleation rate efficiency changes. So, for example, the nucleation on ions requires supersaturation values much smaller than nucleation on uncharged particles (especially for small drop diameter); or, for example,

if a CCN is insoluble in water, the physics governing the survival of an embryonic cloud droplet are the same as in the case of homogeneous nucleation and the nucleation rate decreases with respect to the case the CCN is a soluble particle.

If the aggregated water molecules form a liquid film completely surrounding a particle, then a complete droplet is formed whose radius is larger than it would be in the absence of the nucleus. The larger such a nucleus is, the more likely is the survival of a drop formed by a film around it. For this reason, the larger the aerosol particle, the more likely it is to act as a CCN. There are generally more than enough wettable aerosol particles in the air to accommodate the formation of cloud droplets. However, the physics of the nucleation process just described indicate that the first droplets in a cloud will tend to form around the largest and most soluble CCN (for example NaCl crystals are efficient CCN). The sizes and compositions of the aerosol particles in the air thus have a key role on the size distribution of particles nucleated in a cloud.

The cloud droplets formed by nucleation grow for vapor diffusion producing a fairly uniform distribution where the droplet radius generally ranges between 1 and 10 μ m. In the convective clouds, with high vertical velocity (updraft), the diffusive growth maintains its efficiency for droplet radius up to 50 μm. Once the droplets reach these dimensions, they begin to have a not negligible fall velocity that allows the drops to interact with each others.

Unlike the liquid heterogeneous nucleation, the ice crystals do not form on all the aerosol particle types found in air because the molecules of the solid phase should have a lattice structure similar to that of ice to support the nucleation; an ice nucleus composed by amorphous material cannot nucleate the ice phase fron the vapour phase. As for CCN, particles in the air on which ice crystals are able to form are called *Ice Nuclei (IN)*. Depending on aerosol composition, type and size distribution, there are several processes that lead to the formation of an ice particle. An ice nucleus contained within

a supercooled drop may initiate heterogeneous freezing when the temperature of the drop is lowered to the value at which the nucleus can be activated and the ice phase nucleation starts. This process is referred to as *immersion freezing*. Drops may also be frozen at the time that an ice nucleus in the air comes into contact with a supercooled drop: this process is called *contact nucleation*.

Finally, the ice may be formed on a nucleus directly from the vapor phase, in which case the process is called *deposition nucleation*. This process requires the supersaturation of air with respect to ice. The probability of ice particle nucleation increases with decreasing temperature and that substances possessing a crystal lattice structure similar to that of ice is the most likely to serve as a nucleating surface. In this respect, ice itself provides the best nucleating surface; whenever a supercooled drop at any temperature ≤ 0°C comes into contact with a surface of ice it immediately freezes. The diffusion growth of ice crystals is similar to the diffusion growth of droplets, but the parameterization of the great variety of crystals shape increases the difficulty to analytically describe the process. Like for the liquid phase case, when the ice crystal reaches dimension such that to have an appreciable fall velocity, the aero dynamic capture processes became important.

1.1.2 Cloud particles interactions

When the cloud droplets falling at different vertical velocity interact, the first process that takes place is the collision. As a result of collision, the drops can coalesce or bounce off, according to the energetic balance of the collision. The coalescence takes place when the two colliding drops merge in one larger drops. So, for example two very small colliding drops have lower probability to coalesce compared to two colliding drop

with more marked size difference .

In the same way, the collection growth of ice crystal happens when they begin to move with respect to the air flow, but its description is more complicated than for water droplets because of the greater number of crystal shapes that can be formed and the resulting greater number of possible interactions.

While the drop-drop collision leads to the formation of a particle of the same type of the merging particles (drop), if an ice crystal is involved in the collection process, the resulting particle can be different from the colliding particles. The different collision types result in different final particles, as listed below:

- drop-crystal: if the drop mass is lower than ice crystal, the result is a new ice crystal, otherwise graupel or ice pellet are formed, as function of the air temperature;
- drop-snowflake: if the drop mass is lower than snowflake, the result is a new snowflake, otherwise graupel or hail are formed, as function of the air temperature;
- drop-graupel: graupel or hail are formed as function of the air temperature;
- drop-hail: the result is hail;
- ice crystal-ice crystal: the result is a snowflake;
- ice crystal-snowflake: the result is a snowflake;
- snowflake-snowflake: the result is a snowflake;
- graupel-ice crystal or graupel-snowflake: the result is graupel or ice crystal or snowflake.

The collection of ice crystals by other ice crystals is called *aggregation*, while the collection of supercooled drops by ice crystals is called *riming*.

Aggregation depends strongly on temperature. The probability of collection of colliding ice particles becomes much greater when the temperature increases to above -5°C, at which the surfaces of ice crystals become sticky. Another factor affecting aggregation is crystal type: for instance, dendrite shapes increase the collection probability. About the riming, its efficiency collection is greater than the drop-drop collision because the higher fall speed difference between drops and ice crystals. When a supercooled drop impacts an ice crystal, latent heat is released during the icing of drop. If the latent heat is completely dissipated, and the whole drop mass freezes, the new ice crystal is called *rime* with a low density ($\lesssim 0.15\ g/cm^3$) and the accretion process is called *dry growth*; while if not all the latent heat is dissipated the accretion process is called *wet growth* a liquid film can remain entrapped in the ice core (*"spongy"*) or can surround the ice core and eliminated aero dynamically during the fall (*"shedding"*). In both cases the new particle has higher density ($\sim 0.9\ g/cm^3$). The riming process can also lead to the formation of hail, that has higher density than graupel (generally hail has density higher than $0.9\ g/cm^3$, while graupel density ranges between 0.15 and $0.8\ g/cm^3$) and also larger dimension (the maximum size measured is an hailstone of 20 cm of diameter, while the graupel has diameter generally below 5 mm).

1.1.3 The rain drop formation mechanisms

After the growth of a population of precipitating cloud particles, there are two different accepted mechanisms for raindrop formation: in the first one the rain originates from the melting of ice particle while in the second one, known as "warm rain", the rain originates from collision and coalescence of cloud drops first, and then between rain drops.

As mentioned above, the growth of precipitation by capture and collision of cloud drops plays an important role in the precipitation development, but here we are interested to the possible interactions between the drops: the collision of rain drops (Magarvey and Geldart 1962, McTaggart-Cowan and List 1975a), together with the evaporation process, are the main physical mechanism that influence the DSD shape. Collision of rain drops can lead to two different results: the colliding drops can merge in one larger drop, this process is known as coalescence, or the two colliding drops can break in a higher number of different size drops, this process is known as collisional break-up.
The evaporation process affects the precipitation structure, and it is effective when the drops fall in sub saturated air; this situation usually characterizes the initial stage of rainfall. Generally, small size drops are more affected by evaporation process, due to the inverse dependence of the vapour saturation pressure on the curvature radius of the water/vapour interface (i.e. the drop surface). Therefore, the lower end of DSD can be modified showing a depletion of small drops.
The coalescence has been extensively studied both from a theoretical point of view (Twomey, 1965; Svrivastava, 1971) and from an experimental point of view (Montgomery, 1971; Low and List, 1982a,b). The results highlight that the effect of coalescence is the production of a DSD that is roughly exponential both at small and large diameter while it presents a slightly bump at intermediate diameters (Svrivastava, 1971), due to the increase of their number as consequence of coalescence of small drops. The figure 1.3 shows the modification of an initial Marshall and Palmer DSD considering the coalescence process only and the effect of both the coalescence and the break-up process. In particular, from the coalescence process it is evident the depletion of small size drops with relative increase of medium drops diameter.

Generally, the effects of break-up process on the DSD are an increase of very small

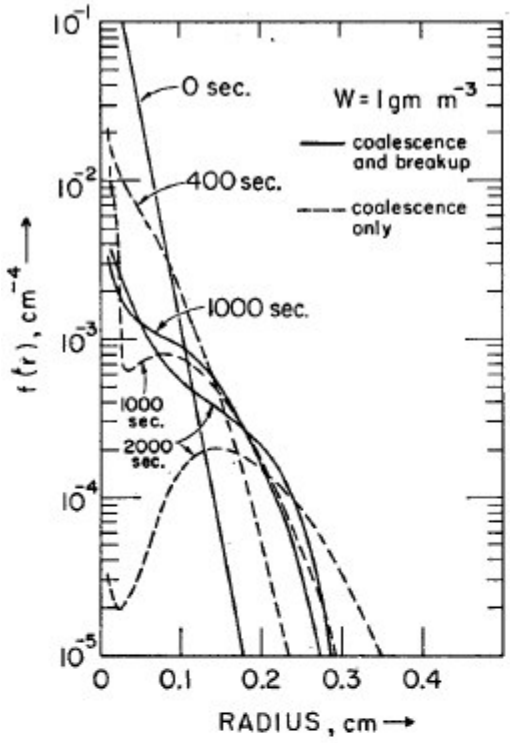

Figure 1.3: Effect of coalescence and break-up on an initial Marshall and Palmer DSD (Srivastava, 1971)

size drops and relative decrease of large drops, as shown by figure 1.3 (solid line).The break-up process can be of two types: the spontaneous break-up, or aero dynamical break-up, when the drop reaches a size such that the internal forces are not able to hold up the drop that breaks under aero dynamical forces, in a lightly turbulent flux; and the collisional break-up, introduced above, when two colliding drops break because the energy of the collision is too high to create a new drop and is not absorbed by viscous deformations and oscillations (Porcú et al., 2013).

The aero dynamic break-up is the result of hydrodynamic instability of large single drop. Different experiments, some studying the falling drop through a column of air at

rest (Blanchard and Spencer, 1970; Alusa and Blanchard, 1971) and some with drops suspended in wind tunnels (Beard and Pruppacher, 1969), have demonstrated that a single drop can reach 9 mm diameter before breaking-up in air at rest. A large drop like this, has internal oscillations and then develops a depression to its base that leads the drop to assume an unstable bag shape and then to break into several smaller fragments. Considering the aero dynamic break-up as a simple balance of the forces effecting on the falling drop in air at rest, the maximum reachable diameter can be estimated as (Pruppacher and Klett, 1969):

$$D_{max} = \frac{4\pi^2 x\sigma}{3C_D\rho_A v_\infty^2} \tag{1.1}$$

where x is the drop axis ratio, σ is the surface tension of water, C_D is the Drag coefficient, ρ_A is the air density and v_∞ is the drop terminal velocity. Since ρ_A and v_∞ are function of air pressure, the 1.1 can be calculated at different altitudes. The D_{max} value depends on which model is chosen to estimate the x value, but the most challenging problem is that a theoretical relationship between the Drag coefficient C_D and the Reynolds Number (Re) does not exist for such large drops. Using the experimental C_D-Re relationship proposed by Loth (2008), the maximum reachable diameter, at sea level, obtained by 1.1 is 10.7 mm.

There are different opinions about the efficiency in DSD modification of aero dynamical break-up rather than collisional one. Villermaux and Bossa (2009) assert that is the aero dynamical break-up that plays the most important role in DSD shape formation. They studied the aero dynamic break-up in a counter-ascending air current generated by a big jet. Figure 1.4 shows a 6 mm diameter drop that in the first stage assumes the bag shape and then breaks into smaller stable fragments. They studied also the probability to have fragments as function of the fragments diameter, for drops of 6

and 12 mm diameter, highlighting an inverse exponential trend from smaller to larger diameter.

There are different points that do not support the dominant role of aero dynamic break-

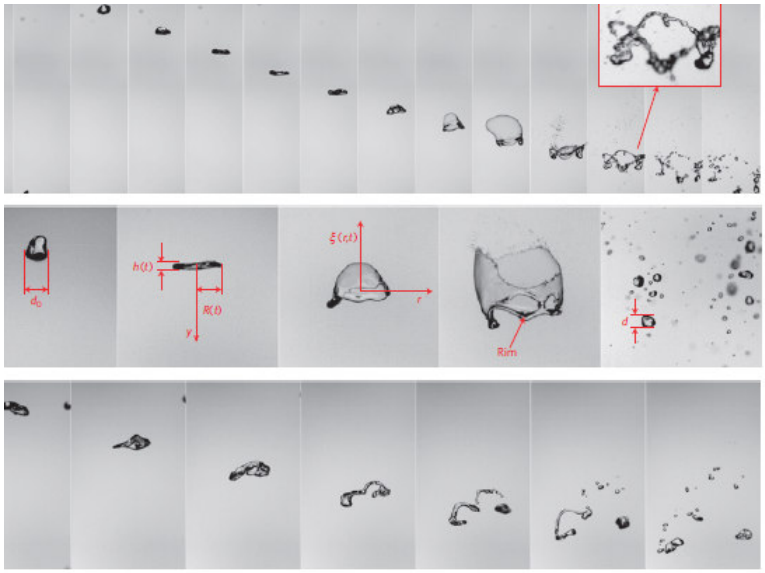

Figure 1.4: Deformation and break of a 6 mm drop diameter due to the aero dynamical break-up. (Villermaux and Bossa, 2009).

up with respect to collisional one. First of all, such large drops are rarely observed in natural rain, where the largest measured drop is about 8.5 mm. The probability, in a natural rain, to not have collisions for such large drops is very low. In fact, it is demonstrated that the mean free path for a drop-drop collision is comparable to the average distance covered by drops larger than 6 mm before to spontaneously break (Prat and Barros, 2009). Prat and Barros (2009) calculated also the collision rate as function of rainfall rate finding an increase of collisions increasing the rainfall rate. They found that for rainfall rate (RR) interval between 10 and 20 mmh^{-1} the collision rate ranges from 1 to 100 collision per cubic meter per second. Furthermore, while the aero dynam-

ical break-up takes place only when drops reach very large dimension, the collisional break-up takes place over a wide size range.

The products of collisional break-up process have been intensively studied because of their importance in DSD modification. The first results were obtained by Mc Taggart-Cowan and List (1975b) setting up an aero dynamic drop accelerator to study collisions between five pairs of drops at terminal speed. With a similar setup, Low and List (1982a, 1982b) and List et al. (2009) increased the spectrum of drop sizes in colliding pairs in order to cover a wider range of events. They found that break-up fragments usually have a bimodal distribution with one big peak at very small size and another one, less marked, at dimension just smaller than the largest colliding drop. Since this aspect will be a significant matter of this Thesis, it will be described with more details in the next section.

1.2 The collisional break-up

Coalescence and break-up are the main mechanisms in the rain formation as consequence of drops collision. The effects of coalescence on the DSD are easy to recognize and re just mentioned in the previous section.

The chance to have collisional break-up (hereafter referred as "break-up") is directly related to the CKE of the two colliding drops as defined by Low and List (1982a):

$$CKE = \frac{\pi\rho}{12}\frac{D_S^3 \cdot D_L^3}{D_S^3 + D_L^3}(v_L - v_S)^2 \tag{1.2}$$

where ρ is the density of water, D is the drops diameter and v is the drops terminal velocity, while the subscripts L and S indicate large and small colliding drop, respec-

tively. All the quantities in 1.2 are expressed in the International System of Units (SI[1]) to obtain the CKE in Joule. The CKE is a balance between the dimension of colliding drops and their relative fall speed. Figure 1.5 shows the CKE as function of diameter of two colliding drops: both two small and two large colliding drops produce low CKE values because of their similar terminal velocity, while the collision of two drops of different size produces high CKE values.

Low and List (1982a) analyzed the effects of drops collision by studying the process

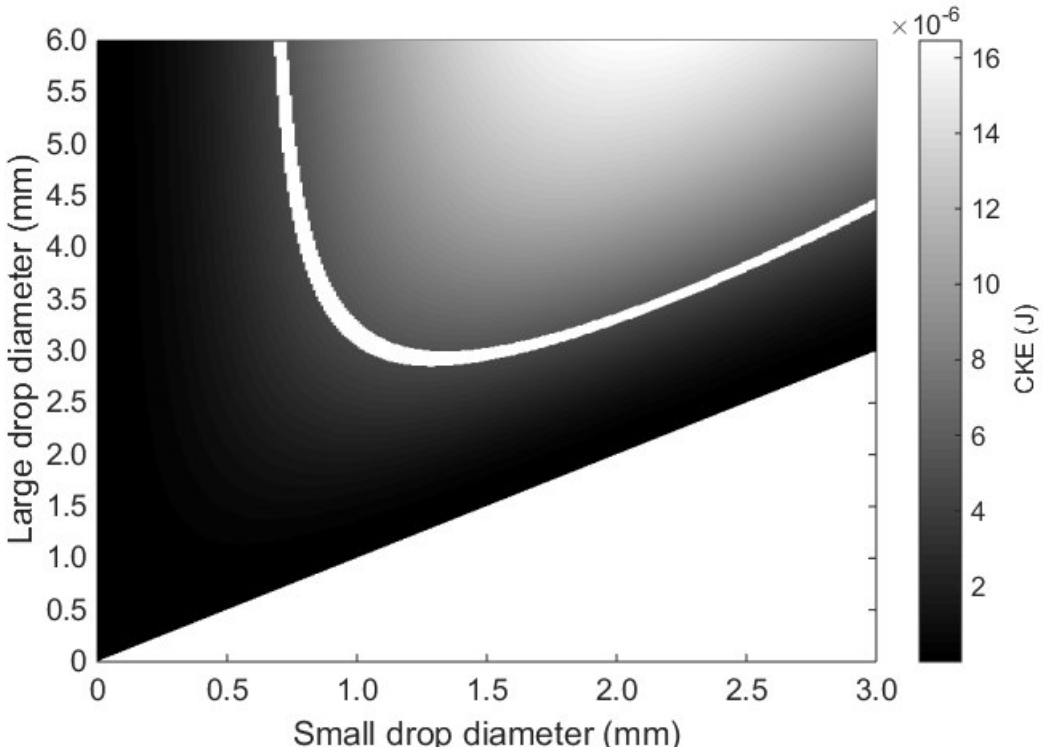

Figure 1.5: CKE values, expressed in Joule, as function of diameter of two colliding drops.

in laboratory. For the experiment, they used an improvement of the aero dynamical drop accelerator used by McTaggart-Cowan and List (1975a). The original system de-

[1]In this Thesis the SI is used. However, some quantities are reported according to the unity of measurement generally used in meteorology.

veloped by McTaggart-Cowan and List (1975a) was made up of two parts, one for the production of small drops (with diameter between 1.0 and 2.5 mm) and the other one for the production of large drops (with diameter between 3.0 and 5.0 mm). Each part was composed by a dropper pump, a free fall zone, an accelerator (with a number of propulsion unit higher for large drops production) and a camera in the collision region. The system was equipped with an electrostatic device to control the rate production of drops, especially for the smaller ones. Low and List (1982a) improved on the original system in order to reveal drops smaller than 1 mm diameter and with a better photographic equipment. They did collide ten drop pairs with different diameters ranging from 0.04 to 4.4 mm diameter basing their choice on the probability to have collision in natural rain for the selected sizes. They calculated the efficiency of coalescence as follows:

$$E_{coal} = a\left(1 + \frac{D_S}{D_L}\right)^{-2} \exp -\frac{\sigma b E_T^2}{S_C} \tag{1.3}$$

where σ is the surface tension of water, a and b are two constants, E_T is the total energy of coalescence and S_C is the surface energy of the spherical equivalent drop. The 1.3 is valid for $E_T < 5\mu J$ since they found that no coalescence is observed for $E_T > 5\mu J$, and this is considered the threshold that marks the transition from coalescence to break-up for two colliding drops.

The products of break-up are fragments of different shape and size. Low and List (1982b) studied, in the same experiment, the distribution of fragments from collisional break-up. They found three different fragments shape: filament, sheet and disk in accordance with what found McTaggart-Cowan and List (1975b). Considering the overall break-up results, the fragments have a bi-modal distribution. The first and more marked peak is at very small diameter (generally around 0.5 mm), while the second is at dimension slightly smaller than the largest colliding drop. This reflects

what previously said, that is the effect of break-up on the DSD is an increase of small drops. Considering separately each fragment shape, they found that the distribution of the sheet and disk fragments is a Gaussian distribution for large drop fragments, while is a log-normal distribution for small drop fragments. Instead, for all filament break-ups they found that both distributions for small and large drop fragments are Gaussian function, while the remaining part of fragments follows a log-normal distribution. The distribution of fragments as parameterize by Low and List (1982a) has been used by different authors which studied the collisional processes (McFarquhar, 2004; Prat and Barros, 2007). The figure 1.6 reports the fragments distributions for five colliding

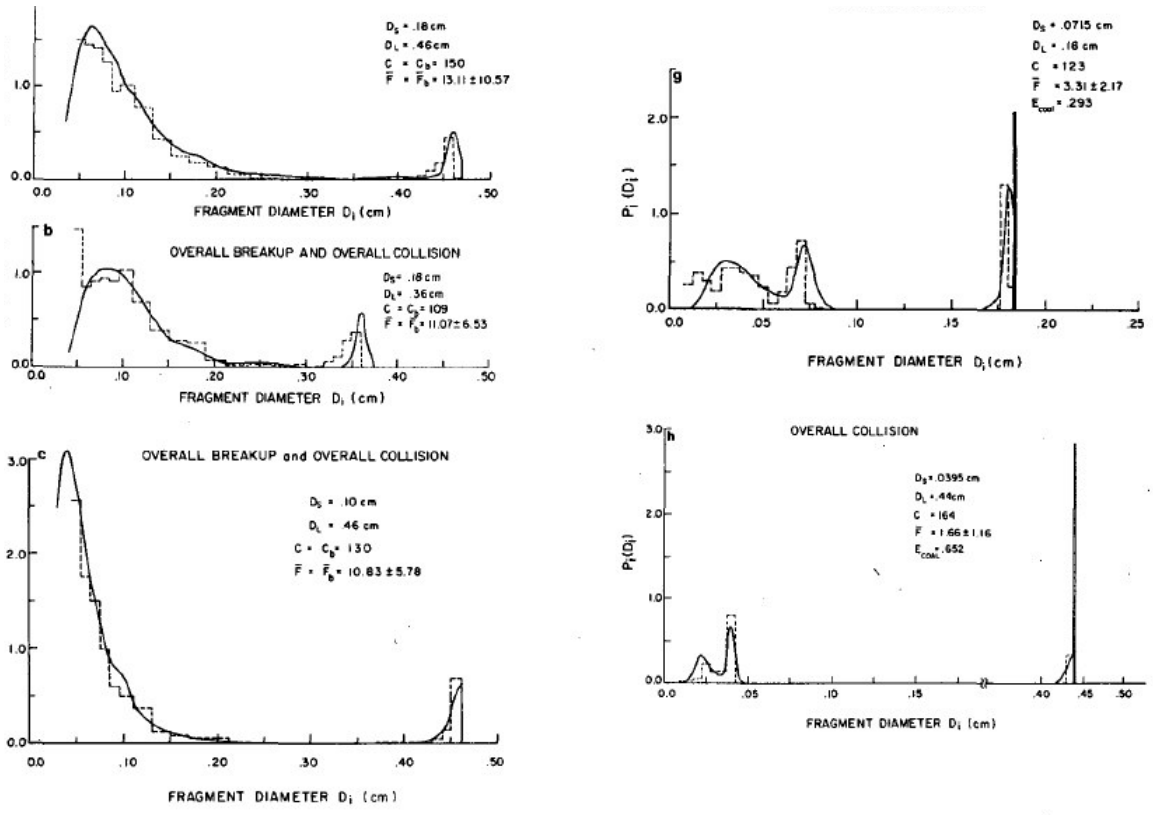

Figure 1.6: Fragments distribution for overall collision for five different colliding drops couples. (Low and List, 1982a)

drops pairs by Low and List (1982b) laboratory studies. It shows the two peaks at low and large diameters.

A further parameter that affects the outcome of a collision is the eccentricity, ϵ, defined as the ratio between the distance of the two colliding drop centers δ and the arithmetic mean of the diameters of volume equivalent spheres D. It plays a crucial role for the appearance of a specific break-up mode (disk, sheet, and filament) and for the number of fragment drops created. The mathematical expression for eccentricity ϵ is:

$$\epsilon = \frac{2\delta}{D_L + D_S} \tag{1.4}$$

Schlottke et al. (2010) simulated the Low and List (1982a,b) experiment implementing a numerical collisional model and increasing the number of drop pairs and taking into account also the eccentricity. They found that the highest values of CKE result in a relatively large number of fragments.

They show that drop pairs with $CKE > 5\mu J$ always present the break-up products (1.7), regardless the value of ϵ, while for CKE close to $5\mu J$ the break-up can occur for high eccentricity value (1.8). Compared to the parameterizations derived by Low and List (1982b), the fragment distributions obtained in this study exhibit similarities but also discrepancies, especially with respect to the peak at small size. Namely, for some colliding couple the peak of small fragments is found at size slightly larger than 0.5 mm and closer to 1.0 mm.

The figure 1.8 reports the snapshots of collisions between 4.6 and 1.8 mm diameter drops for different ϵ values. The CKE value corresponding to the collision is equal to 12.53 μJ, therefore over the 5 μJ threshold, and break-up occurs also for $\epsilon = 1$, although the results of collision are only fragments of very small size. On the other hand, figure 1.8 refers to two colliding drops of 2.7 and 1.5 mm diameter with CKE

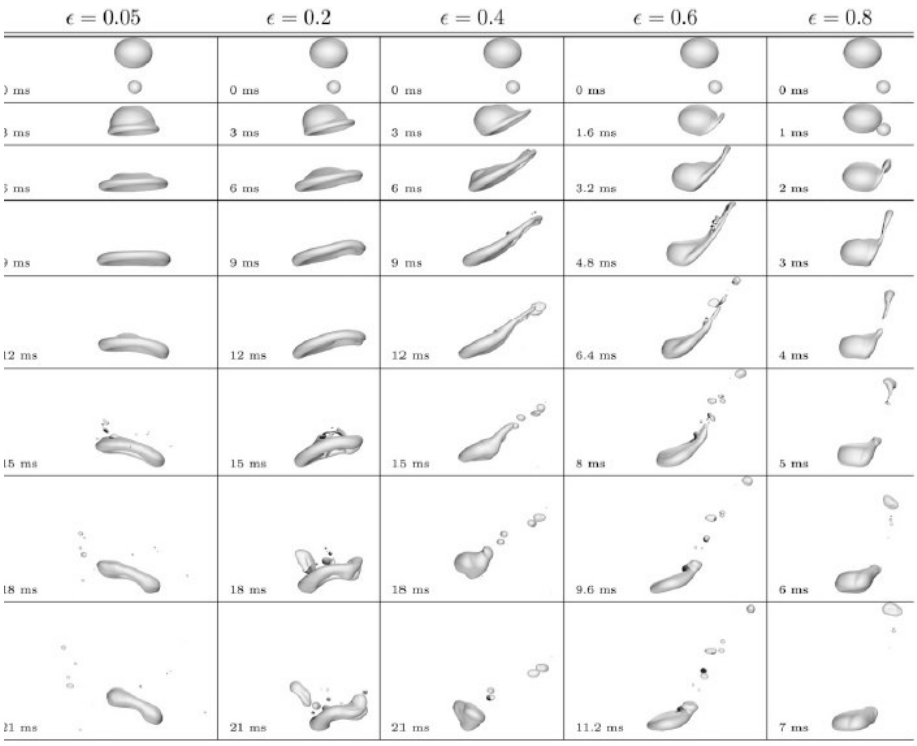

Figure 1.7: Snapshots of drop collisions for various eccentricities and at different times for colliding drops of 4.6 and 1.8 mm diameter respectively. (Schlottke et al., 2010)

value of 3.93 μJ. In this case, although the CKE is slightly below the $5\mu J$ threshold, the break-up takes place for moderate/high eccentricity values.

1.3 The equilibrium drop size distribution (ED)

The parameterization of collision-coalescence and collision-break-up process has been used to study the modification on an exponential DSD. List et al. (1987) used the Low and List (1982b) parameterization to analytically examine the evolution of rain-drop distribution in 1-dimensional box model. They started from a Marshall-Palmer distribution and performed a numerical integration at different rainfall rate. The result

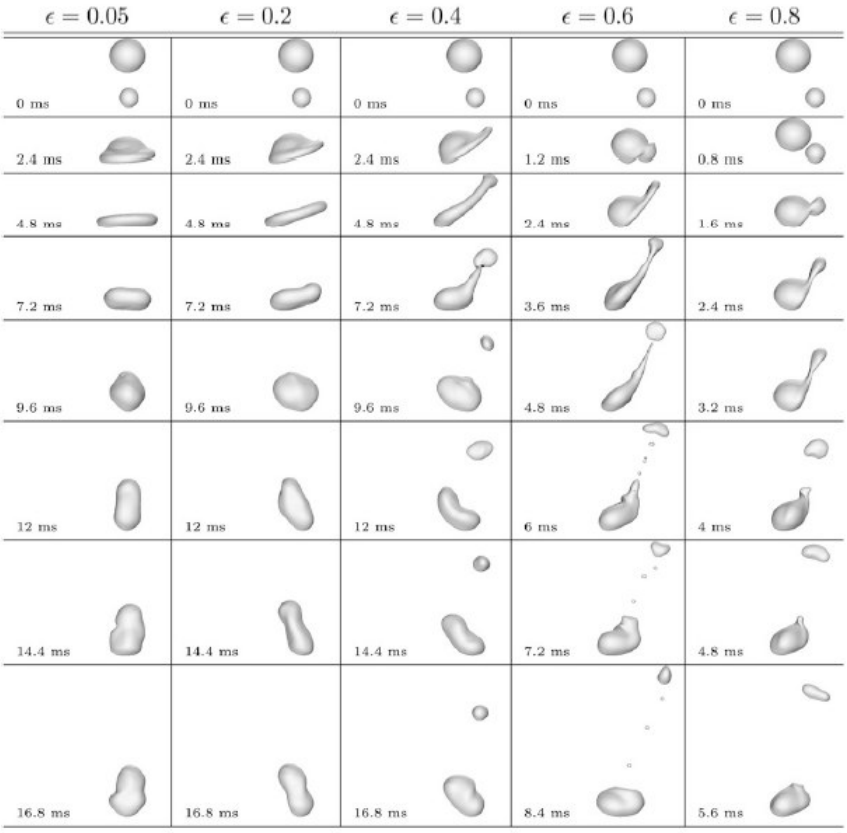

Figure 1.8: Snapshots of drop collisions for various eccentricities and at different times for colliding drops of 2.7 and 1.5 mm diameter respectively. (Schlottke et al., 2010)

was a trimodal ED with the more marked peak at about 0.26 mm while the other two peaks at 0.8 and 1.8 mm diameter respectively. Furthermore, they found that the ED is reached for heavy rainfall intensity.

More recently McFarquhar (2004), based on Low and List (1982a), introduced a new parameterization to derive the ED. The new model takes into account that the distributions of collisional break-up products are combinations of lognormal, Gaussian, and modified delta distributions, and ensures the conservation of number of small drops associated to filament and large drops associated to sheet and disk, and the total mass

conservation. This results in a bimodal ED, with the first peak at 0.26 mm (as in List et al., 1987) and the second peak at 2.3 mm diameter. Although the resulting ED is really different with respect to that obtained by List et al. (1987) (bimodal instead than trimodal), the difference for rainfall rate (RR) and some other DSD integral parameters, is very low. The DSD integral parameters used in this Thesis will be defined later within the text (Chapters 4 and 5).

Prat and Barros (2007) investigated the general governing equation for the evolution of the DSD in the presence of coalescence and break-up. In particular, they focused on the impact of varying the shape of the initial DSD on the equilibrium solution of the equation for a wide range of rain rates and break-up kernels. They used different break-up paremeterization (Low and List parameterization (LL82 from Low and List, 1982b); McFarquhar parameterization (MF04 from McFarquhar, 2004), aero dynamical break-up parameterization (SR71 from Svrivastava, 1971), exponential distribution of break-up fragments (FTL88 from Feingold et al., 1988), etc.) and found results in agreement with previous studies. A bimodal ED using McFarquhar kernel, a trimodal ED using Low and List kernel but with the third peak at just a bit larger diameter. Furthermore, their results show that, although there is no dependence of the ED on initial conditions for the same rain rate and break-up kernel, there is large variation in the time that it takes to reach the equilibrium state.

The figure 1.9 reports the EDs obtained by Prat and Barros (2007) using an initial Marshall-Palmer DSD and different break-up kernels. While Low and List (1982a,b) and McFarquhar (2004) break-up parameterization lead to similar ED around the peak at 0.18 mm and 2.6 mm, but with the strong difference about the presence of third peak, both SR71 and FTL88 parameterization lead to different ED shape. FTL88 gives a resulting ED with only one peak around 1.0 mm diameter and a general trend very different from the others; the aero dynamical kernel (SR71) identifies the peak at 2.6

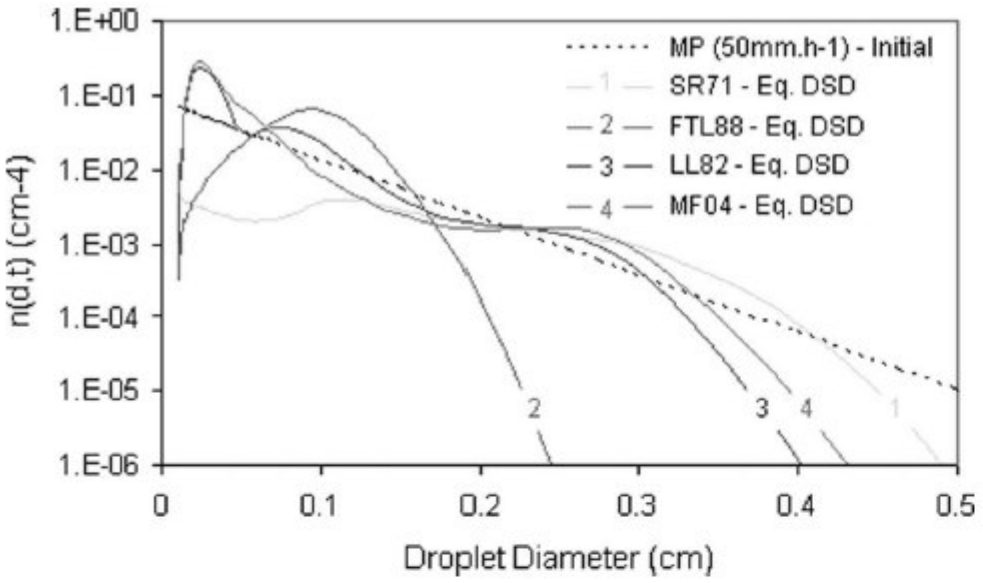

Figure 1.9: EDs for different break-up kernels for initial Marshall-Palmer DSD. SR71 is aero dynamical break-up kernel, FTL88 is collisional breakup using an exponential fragment distribution function, LL82 is collisional break-up using Low and List (1982a,b) parameterization, MQ04 is the McFarquhar (2004) parameterization. (Prat and Barros, 2007).

mm but shows a lower end ED shape different from the others, especially in the number of drops [2]. Straub et al. (2010) derived new parameterizations of the coalescence efficiency and the fragment size distribution and investigated how the new break-up parameterizations influence the shape of a size distribution until the ED is reached. Comparing their results with Low and List (1982a) and McFarquhar (2004) results, they found some differences. First of all, accordingly with the most recent analysis (McFarquhar, 2004; Prat and Barros, 2007), they found a bimodal ED but while the peak at small diameters is slightly shift toward about 0.35 mm, the second peak is found at smaller diameter with respect to McFarquhar found, 1.6 mm instead than 2.3

[2]The unit of measurement used by Prat and Barros (2007) for N(D) is not the usual $m^{-3}mm^{-1}$ but cm^{-4} that presents four order of magnitude of difference in number of drops

mm.

Evidence of break-up influence on experimental DSD shape, up to reach the ED, was also observed by Zawadzki and De Agostinho Antonio (1988) and Willis and Tattelman (1989), showing bimodal or trimodal trend in heavy rainfall DSD, at rain rates higher than 100 and 200 mmh^{-1} respectively. In particular, Zawadzki and De Agostinho Antonio (1988) recorded their data in Brazil and found very good agreement with the theoretical solutions of stochastic equation. In most of the cases, they observe a trimodal ED with the three maxima between 0.6-0.7, 1.0-1.2 and 1.8-2.1 mm diameter as shown in figure 1.10.

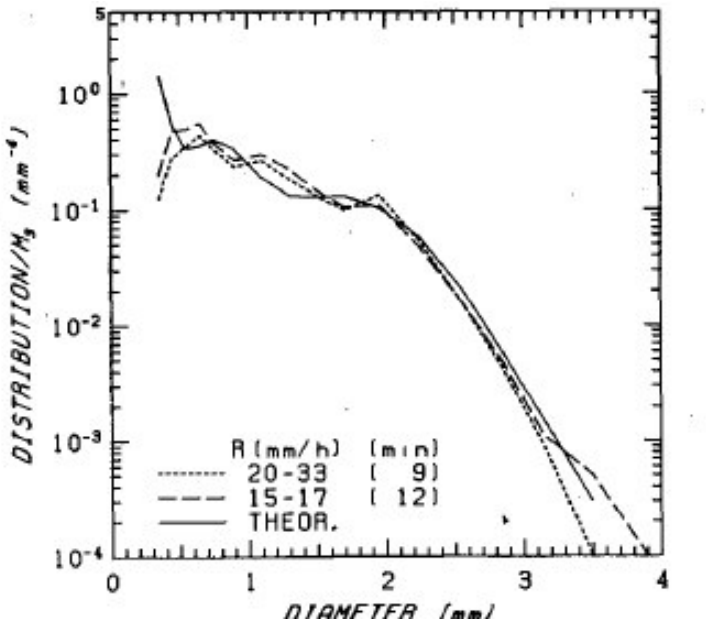

Figure 1.10: DSDs measured by Zawadzki and De Agostinho Antonio (1988) at different rainfall rate values compared with numerical solution for the stochastic equation. (Zawadzki and De Agostinho Antonio, 1988)

More recently, Porcú et al. (2013, 2014) measured DSDs at different altitude and observed the effects of the break-up on the DSD resulting in a bimodal shape. They found

that peak diameters were different than those reported by McFarquhar (2004) and had altitude dependency. They also analyzed the CKE trend with altitude showing that although the diameters interested in break-up process are different each other due to the difference in altitude, the CKE produced is the same.

1.4 The DSD parameterization

In this section will be presented the mathematical functions that are generally used to parameterize the DSD.

The parameterization of DSD finds applications in various field of atmospheric science: in the estimation of rainfall rate from radar measurement, in numerical models both (cloud microphysical models or mesoscale models for weather forecasting application), etc.

The first that tried to measure the DSD in natural rain was Wiesner (1895), exposing to the precipitation a filter-paper dusted with a water soluble dye. The measurement was done in a systematic and methodical manner by Marshall and Palmer (1948) always recording the raindrops on a dyed filter paper. They approximated the DSD with an exponential distribution of this form:

$$N(D) = N_0 e^{-\Lambda D} \tag{1.5}$$

where D (mm) is the equivolume spherical diameter, N(D) is the number of drops in the diameter interval between D and $D + \delta D$, N_0 is the intercept parameter, that is the number of drops when D=0 and generally has a constant value $N_0 = 8 \cdot 10^3 m^{-3} mm^{-1}$ and $\Lambda(mm^{-1})$ is related to the rainfall intensity (RR) by the empirical relationship:

$$\Lambda = 4.1RR^{-0.21}(mm^{-1}) \tag{1.6}$$

The equation (1.5) describes an inverse exponential distribution with the peak in number of drops at D=0. There are many other experimental results that show that equation 1.5 is a good approximation for DSD.

The improvement in disdrometers technology allowed to collect more data that showed a number of small drops, generally at diameters smaller than 1 mm, lower than that predicted by Marshall and Palmer distribution. Waldvogel (1974) has shown that large and sudden changes in N_0 can occur as a function of precipitation type. In these situations is necessary to take into account the variation of N_0 that is assumed constant in equation 1.5. Ulbrich (1983) introduced a new parameterization for the DSD using a gamma distribution expressed as:

$$N(D) = N_0 D^{\mu} e^{-\Lambda D} \tag{1.7}$$

where μ is the shape parameter and can assume both positive and negative values determining the downward or upward concavity respectively, and Λ is the slope of distribution and can assume only positive values. Higher values of Λ indicate narrow distribution in the absence of large drops while the wide distribution results in lower Λ values.

The figure (1.11) shows four different gamma distribution as function of μ and Λ values for a given N_0. Positive μ values give a downward concavity and negative values upward concavity, while high Λ values give more flat distributions and low Λ values steeper distributions. The three parameters of gamma distribution (N_0, μ and Λ) are generally derived using the method of moments. The nth-moment of the DSD, for a

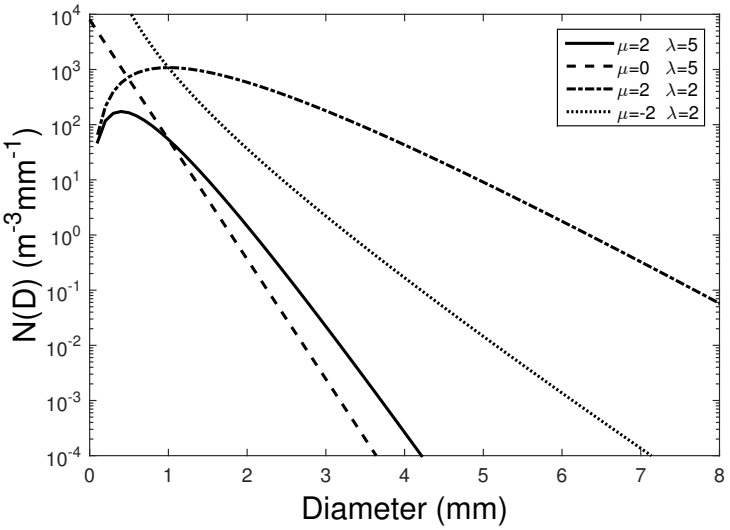

Figure 1.11: Examples of gamma distribution for different μ and Λ values.

gamma DSD model, has the form:

$$M_n = \int_0^\infty D^n N(D) dD = N_0 \Lambda^{-(\mu+n+1)} \Gamma(\mu + n + 1) \tag{1.8}$$

where $\Gamma(x) = \int_0^\infty e^{-t} t^{x-1} dt$ represents the complete gamma function of a generic variable x.

Almost all the integral DSD parameters (i.e. radar reflectivity, rainfall rate, etc.) can be approximated by a moment of gamma distribution expressed as (1.8). The three parameters of gamma distribution are generally determined by a combination of three moments, i.e. moments 2-3-4 (M234) or moments 3-4-6 (M346) and so on, and assume different expressions. Depending on the integral parameter studied, different methods of moments are used to parameterize the DSD and the closest moments to the interested parameter give the smallest bias and fractional error. Cao and Zhang (2009) showed that middle-moment estimators of gamma DSD parameters produce fewer errors than

the lower- and higher-moment estimators. If the DSD follows the gamma distribution, as for the most part of the cases, M234 has the best overall performance in estimating the considered variables. However, if there is an appreciable error between the DSD and the gamma distribution, i.e. as for the equilibrium DSD, the performance of M234 will degrade. In this case, the selection of a moment estimator depends on the considered integral parameters.

In general, the three parameters N_0, μ and Λ can be derived from any three moments, such as the second, third and fourth. Using a ratio defined as:

$$\eta = \frac{M_2 M_4}{M_3^2} \tag{1.9}$$

μ and Λ can be easily derived:

$$\mu = \frac{4 - 3\eta}{\eta - 1} \qquad\qquad \Lambda = \frac{M_2}{M_3(\eta - 1)} \tag{1.10}$$

while N_0 can be obtained by substituting the expressions of μ and Λ in the (1.8).

It should be noted that the integration in (1.8) is performed from 0 to infinity, that is, an untruncated size distribution and this means that drops can assume an infinite size range. This statement is incorrect because in natural rain only a finite number of raindrops were observed within a finite size range (D_{min}, D_{max}) because of practical and sampling limitation in measuring small and large drops. Furthermore, from a physical point of view, the drops can reach a limited dimension during their fall due to both collisional and aero dynamical break-up. If the assumption $D_{min} = 0$ produce a very negligible error, the same can not be said if the assumption $D_{max} = \infty$ is taken into

account. Considering D_{min} and D_{max} as limits of integration, the (1.8) becomes:

$$M_n = \int_{D_{min}}^{D_{max}} D^n N(D) dD = \\ = N_0 \Lambda^{-(\mu+n+1)} [\gamma(\mu+n+1, \Lambda D_{max}) - \gamma(\mu+n+1, \Lambda D_{min})] \quad (1.11)$$

where $\gamma(x,y) = \frac{1}{\Gamma(x)} \int_0^y e^{-t} t^{x-1} dt$ represents the incomplete gamma function of generic variables x, y.

The use of truncated moments calculated according to the (1.11), to fit a DSD may cause a larger error than the use of untruncated moments in estimating the DSD parameters μ, Λ and N_0. The narrower the distribution (that is, D_{min} increases or D_{max} decreases, corresponding to small values for μ and Λ), the larger the error (Vivekanandan et al., 2004). Being the (1.11) a non-linear equation, it can be solved applying an iterative method which solutions are the unknowns μ and Λ. The effect of truncation is strongly dependent by the choice of D_{min} and D_{max}.

1.5 DSD and radar parameters

The knowledge of the DSD is essential for many applications in various disciplines of earth sciences. While rain gauges directly measure rain intensity and accumulation at a point, regional to continental mapping of rainfall relies heavily on measurements that include ground-based radar and satellite remote sensing. These remote sensing measurements necessarily employ empirical relations and underlying assumptions that are directly related to and affected by characteristics of the DSD. The accuracy of the rainfall estimates using single polarization radar measurements traditionally relies on

the appropriateness of derived radar rainfall relations including radar reflectivity to rain rate, Z-R, relationship[3]. The reflectivity Z and the rain rate RR are defined, as follows:

$$Z = \int_{D_{min}}^{D_{max}} D^6 N(D) dD \tag{1.12}$$

$$RR = \frac{\pi}{6} 3.6 \cdot 10^6 \int_{D_{min}}^{D_{max}} v(D) D^3 N(D) dD \tag{1.13}$$

where $v(D)$ is the terminal fall speed of drops, D is the drop diameter and $N(D)$ is the DSD. In the 1.13 the constant value $3.6 \cdot 10^6$ is necessary to express the RR in mmh^{-1}, its typical unit in meteorology. The Z-R relationship has the following form:

$$Z = AR^b \tag{1.14}$$

where the parameters A and b depend on the characteristics of the site (geographical location, local climatology, altitude, etc..) and the event (season, time of the day, type of precipitation, etc.). Due to the large diffusion rain gauges, it is common practice to evaluate radar-rainfall estimates with respect to rain gauge measurements, which are considered a good ground reference. However, rain gauges provide point values when compared to radar data, which are areal estimates. These sampling uncertainties, henceforth referred to as spatial sampling error, have been the object of numerous studies and need of gauge network to be limited. Since the rainfall is a derived product and the reflectivity is a direct radar measurement, disdrometers provide the most relevant data source to study spatial variability of rainfall and reflectivity. On the other side, a disdrometer network is more expansive and need a major maintenance with respect to a gauge network. Futhermore, radar measurements and rainfall are integral

[3]The rain rate is indicated as RR within this Thesis. However, in the radar reflectivity to rain rate relationship it is indicated with R and, just in this case RR is substituted by R

products of the DSD and a disdrometer is often employed to derive Z-R relations for a climate region, a particular weather system, or even a season. The highly variable nature of the DSD, for example from one weather system to another or between convective and stratiform parts of the same storm, results in substantial differences in derived ZR relations. Battan (1973) summarized 69 different Z-R relationships, calculated by different authors and derived for different climatic settings in various parts of the world. The A coefficient assumes a very wide range of values, with a difference of one magnitude order too, while the b coefficient moves from values close to 1 to values close to 2. With the development of dual-polarized radars the use of Z-R relationship lost importance because of the availability of more radar parameters. For the dual-polarization radars, disdrometer observations are often employed in deriving relationships between polarimetric radar observables such as reflectivity at horizontal polarization (Z_h), differential reflectivity (Z_{dr}), and specific differential phase (K_{dp}) and rain rate (i.e. Gorgucci et al., 1995, Tokay et al. 2002 and many others). The mathematical expression for the horizontal/vertical reflectivity is:

$$Z_{H,V} = \int_{D_{min}}^{D_{max}} \sigma_{H,V}(D) N(D) dD \tag{1.15}$$

where $\sigma_{H,V}$ is the backscattering cross section at horizontal and vertical polarization respectively. The differential reflectivity Z_{dr} is defined as the ratio between horizontal and vertical reflectivity, namely:

$$Z_{dr} = 10 log \frac{Z_H}{Z_V} \tag{1.16}$$

Usually both $Z_{H,V}$ and Z_{dr} are expressed in dBZ, while K_{dp}, that is the difference between the horizontal and vertical phase shift, is expressed in km^{-1} and its formulation

is:

$$K_{dp} = \frac{180}{\lambda} 10^3 \int_{D_{min}}^{D_{max}} \Re \left[f_{hh}(D) - fvv(D) \right] N(D) dD \tag{1.17}$$

where λ is the wavelength of radar, $f_{hh,vv}$ is the forward complex scattering amplitudes at horizontal polarization and vertical polarization, respectively, and $\Re$ indicates the real part operator. Following the 1.14 the relationship between polarimetric radar variables and rainfall rate[4] have the form:

$$R = AK_{dp}^b \tag{1.18}$$

$$R = AZ_h^b Z_{dr}^c \tag{1.19}$$

$$R = AK_{dp}^b Z_{dr}^c \tag{1.20}$$

1.6 DSD Variability

The highly variable nature of rainfall is well known: it is not uncommon that one experiences rainfall while another one not, or that one experiences heavier rainfall than the other. The lifting mechanism that origin the cloud and the environmental conditions, as well many other factors, play a crucial role in determining type and intensity of the precipitation. The lifting based on solar heating or forced by orography results in shorter-lived precipitation if compared to that originated by frontal lifting mechanism. This reflects in an higher variability of precipitation structure in the former case with respect to the latter. Moreover, embedded convection is not uncommon within stratiform rainfall, especially at mid-latitude over complex orography.

Space-borne and ground-based remote sensors provide data to estimate rainfall rate. These estimates allow to evaluate the variability of precipitation intensity at large scale,

[4] Also for the relationship between rain rate and polarimetric radar variables RR is substituted by R

but ar not able to resolve the structure below the footprint size, which is, in many cases, comparable to the variability scale of precipitation field. The rain gauge and disdrometer point-like measurements may provide a direct measurement but they suffer from poor spatial coverage. Dense networks of these instruments are able to shed a light on the horizontal spatial variability of rainfall, even if they provide point values that can be compared with difficulty to remotely sensed areal estimates. This sampling discrepancy needs to be characterized and accounted for to achieve meaningful comparisons between these two measurement. The most part of studies in the literature focus more on the assessment of the impact of the spatial sampling error in radar and disdrometers comparisons than on the formulation of a methodology able to account for it (Zawadzki, 1973; Rodríguez-Iturbe and Mejía, 1974; Morrissey et al., 1995). The description of the statistical properties of spatial sampling uncertainties is a key element in formulating such a methodology. Villarini and Krajewski (2008), for instance, attempted to describe the distribution of the spatial sampling errors in space and time. They found that the standard deviation of the spatial sampling uncertainties tends to decrease with increasing rainfall intensities and accumulation time, while it results larger increasing pixel size.

The natural variability of precipitation needs to be studied in order to better evaluate the spatial sampling error and to have a complete analysis of precipitation pattern. Usually the integral parameters of DSD are analyzed in terms of spatial variability. The easiest parameter to study is the rainfall rate, also because it needs a rain gauge to be measured. If disdrometers network is available, the variability of many other paramaters (i.e. reflectivity, liquid water content, mean mass diameter, etc.) can be directly investigated. Extreme spatial variability of rainfall is a source of fundamental difficulties in the evaluation of radar rainfall estimates. Furthermore, spatial variability, especially at small scale, have important implications in hydrological applications

because they require analyses across different spatial scales. It has also implication if partial beam filling is present, that is, when the radar cell or satellite footprint is not completely covered by rain. In this contest, it is fundamental to understand how much the precipitation is correlated within a radar pixel or satellite footprint. A good way to do this is to use a three-parameter exponential function (Habib and Krajewski, 2002):

$$R(d) = R_0 e^{\left(-\frac{d}{d_0}\right)^{s_0}} \tag{1.21}$$

where d_0 and s_0 are the unknowns of the function and represent the correlation distance and the shape parameter, respectively. A more complete description of all function parameters will be given in the dedicated section 5.1.

Habib and Krajewski (2002) used this function to estimate the spatial variability of rainfall analyzing ground radar measurement by using a rain gauge network. Within the size of the radar pixel of 2 km, the rainfall field observed by the rain gauges decorrelates to about 0.6 for a 5-min accumulation time, while higher values of 0.7 and 0.8 are found for 15-min and 60-min accumulations time, respectively. Ciach and Krajewski (2006) analyzed a 3 x 3 km area covered by 25 gauges and used the model represented by equation 1.21 for different averaging time-scale and found that both d_0 and s_0 parameter increase increasing the averaging time-scale (the complete description of the function and its parameters will be given to the Chapter 5); simultaneously the root mean square error (RMSE) of fit between real data and model data decrase increasing the averaging time-scale. If the analysis is made for some particular events that present different rain intensity, the three-parameter exponential function results in different behavior, with high correlation distance and shape parameter and low correlation distance and shape parameter for convective and stratiform precipitation respectively.

Tokay and Öztürk (2012) analyzed a dataset with 6 rain gauges spaced from 0.4 to 5 km and found correlation distances, as function of time integration, really higher than what Ciach and Krajewski (2006) found. They found also results in agreement with Ciach and Krajewski (2006) with very different correlation trend if uniform, moderately and highly variable precipitation cases are considered. Tokay et al. (2014a) analyzed spatial variability of rainfall over a 11 rain gauges network with separation distance from 1 to 150 km. They found correlation distance values higher for fall-winter season with respect to spring-summer and an increase increasing the integration time.

Although all these works are based on rain gauges network, a disdrometer network is the best way to investigate the DSD variability, even if the maintenance of a such structure,from different points of view, is complicated. This is the main reason that the literature is lacking of work regarding the study of DSD variability from disdrometer observations. Miriovsky et al. (2004) limited their study to the spatial variability of radar reflectivity using four different disdrometer types. In particular, they compared the joint density functions of 1- and 15-min reflectivity and rainfall rate data. They found that the 1-min reflectivity data indicate higher spatial variability than 15-min data; the coefficient of variation (CV, defined as the ratio between the standard deviation and the mean value of a variable) indicates that the reflectivity is more variable of rainfall rate. However, their work was strongly limited by using different disdrometer types resulting in difficulty to distinguish between the natural variability of the DSD and instrumental effects so that they were unable to make any quantitative statements about small-scale spatial variability of reflectivity because of the overwhelming instrumental effects.

Later, Lee et al. (2009) used four POSS (Precipitation Occurrence Sensor Systems), a disdrometer very similar to Pludix, to study the DSD spatial variability. The distance between each disdrometer couple ranged from 1.3 to 31 km. They analyzed the

moments of DSD and as well as the rainfall rate and the radar reflectivity. Analyzing the mean DSDs, the authors found significant difference highlighting significant spatial variability of DSD and its parameters. They showed also that the lower moments of DSD have correlation greater than high moments and this underlines that the big drops play an important role in DSD variability. They found also an appreciable variation of number density N_0. However the campaign had not be sketched for the DSD spatial variability study and this limited the analysis.

Also Tokay and Bashor (2010) used a disdrometric dataset, composed by three JW disdrometers operating at a distance of 0.65, 1.05, and 1.70 km in a nearly straight line, to examine the variability of DSDs and its integral parameters of liquid water content, rainfall, and reflectivity. The studied the DSD spatial variability for different integration times analyzing both the trend of the standard deviation of the difference (SD) and Pearson product-moment correlation coefficient between the pairs of disdrometer measurements. Generally, SD decreases increasing the integration time while increase with the distance. Similarly, the correlation coefficient decreases with the distance and increases for longer integration period. Considering the 6-min the integration time as reference, the parameter that has the greatest variation with the distance is the mean mass diameter, while the reflectivity has the lowest variation among the integral parameters. The study focused on the partial filling of a radar pixel and showed that in 10% of the cases a single disdrometer reported more rainy minutes than the rainy minutes when all three disdrometers report rainfall. Similarly two out of three disdrometers reported 5%more rainyminutes thanwhen all three were reporting rainfall considering 1-min data.

More recently Jaffrain et al. (2011) set up a very dense disdrometer network, collocating 16 Parsivel (old version) in 1 km^2. The spatial variability is quantified by the coefficient of variation of the total concentration of drops, the mass-weighted diameter,

and the rain rate between the 16 stations of the network. They found a trend of CV for total concentration of drops and rain rate with the high values of CV for the low values of both D_m and RR, while low values of CV result for $N_T > 400$ m^{-3} and RR> 15 mmh^{-1}, respectively. The CV of mass-weighted diameter does not show any trend and ranges between 3% and 60%.

In this Thesis the DSD spatial variability is studied using data from disdrometer networks of two field campaigns. This allows to analyze the rainfall rate and other DSD parameters (i.e. maximum drop diameter, radar reflectivity, etc.). The disdrometer networks used here have specific peculiarities with respect other field campaigns both for number and spatial arrangement of disdrometers (i.e. the Wallops network has dimensions comparable to a radar pixel or satellite footprint).

Chapter 2

Instrumentation and field campaigns

The word disdrometer, as instrument ables to measure sizes and velocities of drops, was used for the first time by Clardy and Tolbert (1961). The disdrometer is designed to measure the DSD, while other instruments are able to derive the DSD from their measurements. The disdrometers can be based on different measurement principles. This assures a such of variety in measurements, since each disdrometer type brings out a particular characteristic of the precipitation. It is not too easy to collect disdrometric data because of the difficulties in maintenance of disdrometers network due to the costs and logistic problems as well. Not secondary, is the necessity to have high qualified person to check the correct functioning of the instruments. Much easier is to collect rainfall rate (and rain amount) measurements, that is an integral parameters of DSD, but that does not give information about the precipitation properties.

Within this chapter, after an overview, from historical point of view, of the developments of the disdrometers, the properties of disdrometers which data are used for this Thesis

as well the characteristics of field campaigns will be described.

2.1 Instruments overview

The first attempts to measure raindrop sizes date from 1895, when Wiesner (1895) published the description of a method consisting of using a sheet of absorbent paper covered with a water-soluble dye, which was exposed to rainfall for a few seconds. The drops left permanent marks on paper and the raindrop size was considered as function of the diameter of the marks only. However other factors have to be taken into account as the thickness of the paper, the drops terminal velocity and also the humidity of the paper. About half century later, Marshall and Palmer (1948) used a very similar equipment to measure the size of falling drops. They found an exponential distribution in agreement with what, five years before, Laws and Parsons (1943) found. The Marshall and Palmer work is taken as reference for all the people that approach the study of the DSD.

Another traditional way of measuring raindrop size is the flour method, that was originally presented by Bentley (1904) and subsequently modified by Laws and Parsons (1943). Similarly to the paper procedure, a thick flour layer few millimeter deep is exposed to rainfall for a time interval depending on the rain intensity (generally ranging from 3 to 5 seconds), such that enough raindrops would have been trapped; the formed capsules are marked and oven dried. The drop diameter for each capsule is then calculated by converting the weight of the flour capsule into appropriate raindrop diameter using an suitable relationship between these two quantities. Nowadays, the technology improvements led to the disuse of these methods, except for few rare exception (Mahadi et al., 2014).

Jones (1959) developed another method known as the raindrop camera, which consists

of two cameras placed close together that are synchronized to take two photos simultaneously of the raindrop from two perpendicular angles. This method makes it possible to obtain a three-dimensional reconstruction of the shape of the raindrops, and from there to calculate their size. However this first version of this instrument type suffered of technical limits as the low time resolution (it captured the raindrops every 10 seconds). Clardy and Tolbert (1961) were the first to use the word disdrometer and their instrument consisted by a phototube able to capture the raindrops passing through the sampling region. The instrument used a sheet of light as the sensing element and recorded the number of drops, within certain size ranges, as they fall through the light slit.

All these methods had a poor time and size resolution, due also to the technology limitations of the mid '900. An improvement was possible only when the advances in technology resulted in development the more refined disdrometers, instruments based on different functioning principles and able to measured the number of drops falling within a rain event, that allowed a systematic approach to the DSD measurement.

One of the most widely known and used instruments, since it became commercially available during early 1970s, is the Joss-Waldvogel disdrometer (Joss and Waldvolgel, 1969). It is based on the conversion of the vertical momentum of the impacting raindrop into electrical impulses, that is related to the raindrop size because of both drop mass and velocity depend on the drop size. From its development most of literature refer to the data collected by one or more Joss-Waldvogel disdrometer.

During the 1980s and 1990s several different disdrometers, based on the interaction between the electromagnetic waves and the falling raindrops, were developed. They are know as optical disdrometers and infer the dimension of raindrops passing through their laser beam measuring the attenuation of the laser beam; although the functioning principle is the same they do not work at the same wavelength. Many models have

been developed like, for example, the Vaisala FD12P (FD12P Interface Control Document, 2007, available on the web), the Laser Precipitation Monitor (Thies Clima), which emits a laser beam at 785 nm. Among the laser disdrometers, the Particle Size Velocity disdrometer (Parsivel), that was originally developed by PM Tech Inc., Germany (Loffler-Mang and Joss, 2000), improving the instrument potentiality measuring also the terminal velocity of raindrops. Recently, the OTT redesigned Parsivel developing an upgraded version ($Parsivel^2$), with better measurement accuracy (Tokay et al., 2014b). Since its commercial availability, the $Parsivel^2$ has become one of the most diffused disdrometers.

The need to have raindrops samples in a large volume has been resolved by using radar measurements of the velocity spectra generated by the falling raindrops. Between 1990 and 2000 two very similar instruments, even if developed independently, had been constructed. Sheppard (1990) developed the Precipitation Occurrence Sensor System (POSS) while Prodi et al. (2000) developed the Pludix ("PLUviometro DIsdrometro in band X"). Both the instruments are bistatic low power continuous wave (CW) X-band radar and are based on the Doppler effect principle. The two main differences are that while Pludix is a vertical pointing radar, the beam axes of POSS are oriented 20°from the vertical and that they work at very close frequency (9.5 GHZ for Pludix and 10.525 GHz for POSS).

In the first 2000s, the Two-Dimensional Video Disdrometer (2DVD) (Kruger and Krajewski, 2002; Schnhuber et al., 2007) has been developed. As for the first raindrop camera method (Jones, 1959), the 2DVD has two perpendicular camera that capture the falling drops in its cross-section measuring dimension, fall velocity and shape. The better knowledge of the problems related to the DSD measurement together with the increased technology availability leads having measurements that are obviously not comparable with the first models of this instrument type and make 2DVD one of the

best available instruments.

Recently, another contribution to measuring raindrops is the Micro Rain Radar (MRR), an instrument that is halfway between a disdrometer and radar system. It combines the reflectivity measurement at different heights with the descent velocity of the raindrops by the Doppler effect. The MRR is a continuous wave frequency modulated (FM) radar and this makes possible to perform profile measurements with selectable range resolution.

2.2 Instruments description

In this section the characteristics of the instruments which data are used for this Thesis will be described.

2.2.1 Pludix

The Pludix (PLUviometro-DIsdrometro in X-band), manufactured by Nubila sas, is a bistatic low power continuous wave (CW) X-band radar for monitoring and characterizing atmospheric precipitation at the ground. Its functions are:

- to identify precipitation type (rain, snow, hail, drizzle);
- to provide raindrop size distribution;
- to measure the instantaneous rainfall rate;
- to give the total rainfall in a given time interval.

The Pludix is composed by an external device, in which are housed in all the components to generate the electromagnetic waves and the transmitter and receiver antenna,

and the acquisition data system, that has to be connected to a pc, that contains the data acquisition boards with the Pludix software. Both the external device and the acquisition data system are made with weather resistant materials. The figure 2.1 shows the dome shape external device.

Figure 2.1: The external dome-shaped device of Pludix in which are housed the active sensors of the instrument.

The sensor is an X-band continuous wave, low power (10 mW) Doppler radar (9.5 GHz frequency of operation). The microwave beam emitted by an upward oriented antenna is backscattered by the falling hydrometeors.

The transmitting and receiving antennas are very close to each other and the volume of measurement is immediately above them. The figure 2.2 describes in a schematic manner the geometry of system and the equi-phases surfaces, that are surfaces characterized by the same transmitting power.
Near the ground each hydrometeor reaches an aerodynamic equilibrium and falls at a constant terminal velocity only as a function of its size, in the absence of vertical wind. Since Pludix is a low power radar, its reflecting volume is few meters above the ground

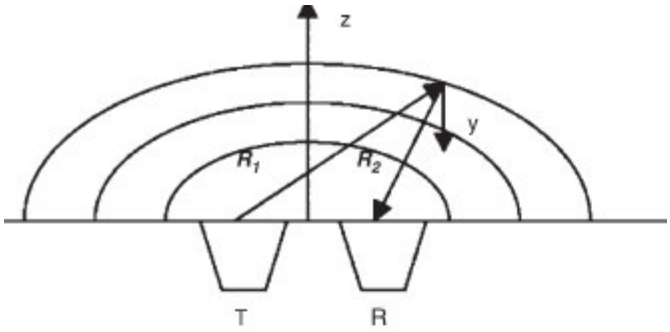

Figure 2.2: Schematic representation of the transmitting and receiving Pludix antenna with the equi-phases surfaces

where the instrument is located, and where vertical wind is zero by definition; so when a hydrometeor enters the measurement volume, it produces a signal whose frequency is a function of its velocity. The amplitude of such components is a function of the reflectivity of the hydrometeors, and their concentrations and location in the volume seen by the sensor. About the latter point, a statistical hypoThesis is made that droplets have an equal probability of falling on a horizontal surface above the instrument. The physical characteristics of hydrometeors affecting the output signal are the backscattering cross section σ_b and the fall velocity v. Both are related to the size, phase (liquid, solid, mixed) and composition (water, air) of hydrometeors.

The theory regarding the computation of backscattering cross section σ_b of a spherical drop by a plane wave, was developed by Mie (1908) which showed that

$$\sigma_b = \frac{\pi r^2}{\alpha^2} \left| \sum_{n=1}^{\infty} (-1)^n (2n+1)(a_n + b_n) \right|^2 \tag{2.1}$$

with $\alpha = \dfrac{2\pi r}{\lambda}$ and λ is the wavelength of the instrument and r the radius of spherical particle. The terms a_n and b_n refer respectively to the scattering arising from induced magnetic and electric dipoles, quadrupole, etc. while n indicates the expansion degree

of a_n and b_n. The terms a_n and b_n can be expressed also as function of the complex refractive index $M = n - ik$ where n is the ordinary refractive index while k is the absorption coefficient of material (in our case, water or ice if raindrops or ice crystals are considered). The 2.1 is always valid but if $\alpha \ll 1$, that is, the drop radius is much smaller than the instrument wavelength, the 2.1 can be written as the Rayleigh scattering formula:

$$\begin{aligned} \sigma_{bi} &= \frac{\lambda^2}{\pi}\alpha^6 \left|\frac{m^2-1}{m^2+2}\right|^2 \\ &= \frac{\pi^5}{\lambda^4}\left|K^2\right| D_i^6 \end{aligned} \tag{2.2}$$

with $K = \dfrac{m^2-1}{m^2+2}$ and D_i the particle diameter.
The basic output of Pludix is the Doppler spectrum of the signal which is obtained from the mixer of the radar as a function of the Doppler frequency shift, collected every minute and sampled from 0 to 1024 Hz in 1024 bins one Hz wide. Generally, a rainy precipitation is able to produce, at the frequency work of Pludix, Doppler frequency shift between 0 and 600 Hz at sea level, a snow event produce frequency shift generally lower than 200 Hz while hail produce very high frequency shift values (if very large hailstones are present the frequency shift can exceed the 1000 Hz). As known, drops fall with a terminal constant velocity that depends on the drop dimensions through the empirical Gunn and Kinzer (1949) relationship:

$$v = 9.65 - 10.3 \cdot e^{-0.6D} \tag{2.3}$$

in which v is the terminal velocity (ms^{-1}) and D the diameter (mm). This formula is effective under standard atmospheric temperature and pressure and for $0.2 < D < 7.0mm$. The figure 2.3 shows the fall velocity, referred at sea level, as function of drop diameter as described by the 2.3 (Gunn and Kinzer, 1949) and of the corresponding Doppler shift frequency obtained by 2.4 as well.

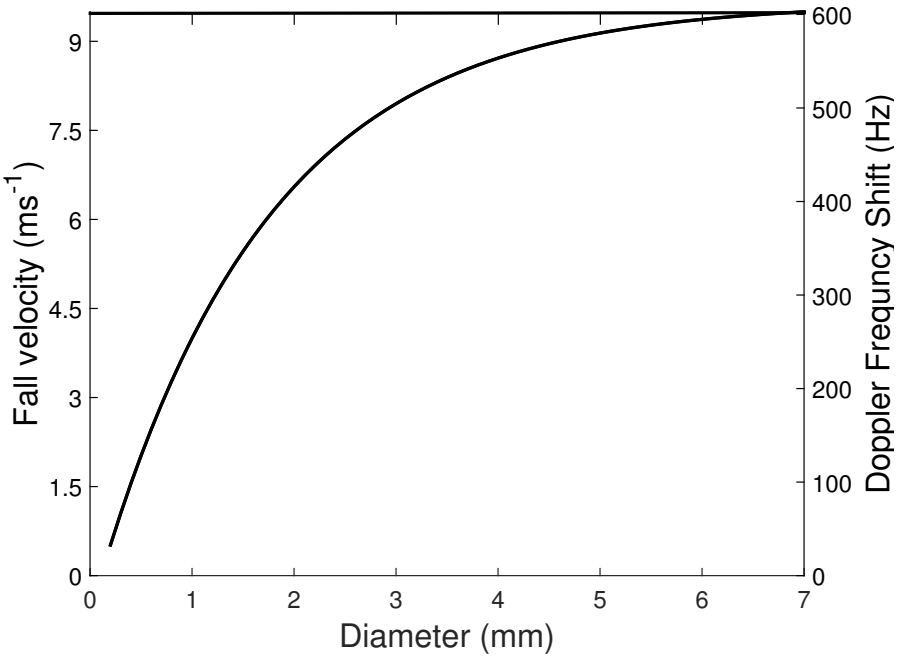

Figure 2.3: Trend of the fall velocity, referred at sea level, as function of drop diameter following Gunn and Kinzer (1949) and of the Doppler shift frequency.

The falling drops when enter in the measurement volume, which varies with drop size from a few cubic meters to cubic decimeters for larger and smaller drops, respectively, produce a Doppler echo whose frequency shift f is proportional to the terminal velocity v:

$$f = \frac{2v}{\lambda} \tag{2.4}$$

where λ is the radar wavelength (for Pludix $\lambda = 0.0315m$). The inversion procedure is based on the conversion of the power spectrum in DSD via the frequency-terminal velocity and the terminal velocity-drop diameter relationships (eq. 2.4 and 2.3).
To estimate correctly the instrument response to natural precipitation and determine the drop size distribution, measurements on monodisperse droplets are performed in controlled conditions and a calibration procedure is constructed (Prodi et al., 2000a,b). Drops are considered spherical up to 1 mm of diameter. The scattering diagram is calculated for a relatively large number of drop size classes using a T-Matrix code (Prodi et al., 1999). If natural rain, as a superposition of monodisperse rains is considered, its spectral intensity S_{real} is:

$$S_{real} = \int_{D_{min}}^{D_{max}} N(D) S_{mono}(D) dD \tag{2.5}$$

where S_{mono} is the spectral intensity generated by a monodisperse rain of diameter D, divided by the number of drops which has caused it, and N(D) is the distribution function, i.e. the relative contribution of that size to the real spectral intensity S_{real}. If the above equation is discretized in frequency and diameter, it gives:

$$S_{f_i} = C_{(f_i, D_j)} N_{D_j} \tag{2.6}$$

where N_D is a column vector whose elements are the number of drops per unit volume in diameter interval D_j, C is the matrix of the contributions to power of monodisperse drops of diameters D_j (column index) at frequencies f_i (row index), divided by the average number of monodisperse drops. For the inversion problem solution, if the C matrix is constructed in such a way that the number of size and frequency intervals are chosen to be the same, it is possible to deduce the drop size distribution N(D) by

the real spectrum S by inverting only the square matrix C. In fact, from 2.6 the N(D) is the unknown quantity to calculate while S is the power spectrum measured by the instrument. The inversion problem is therefore reduced to inverting the square matrix C (21x21). The drops are classified in 21 constant size (0.3 mm wide) intervals, between 0.8 and 7.1 mm, and the actual rainfall rate RR (mmh^{-1}) is computed from the DSD with a time resolution of one minute.

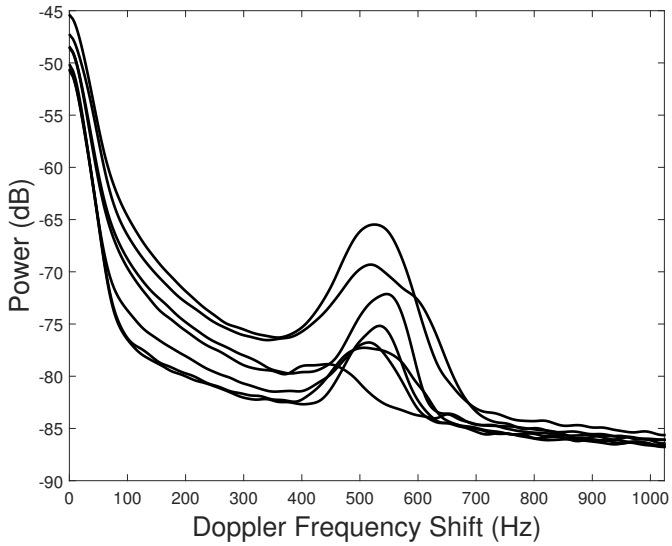

Figure 2.4: Example of some Pludix power spectrum.

The figure 2.4 shows some Pludix power spectrum, as example. The power and the Doppler frequencies interested depend on the rain intensity. The figure 2.5 shows the Pludix power spectrum during a snow event where two main differences result if a comparison with Pludix answer during a rain event is made. One is that the backscattered power during a snow event is lower than a rain event, due to the lower backscattering cross section of ice with respect to the water for small α values at the working frequency of Pludix, and one is that the Doppler frequencies generated are lower because of the lower terminal velocity of snow flakes. The velocity-dimension relationship is gener-

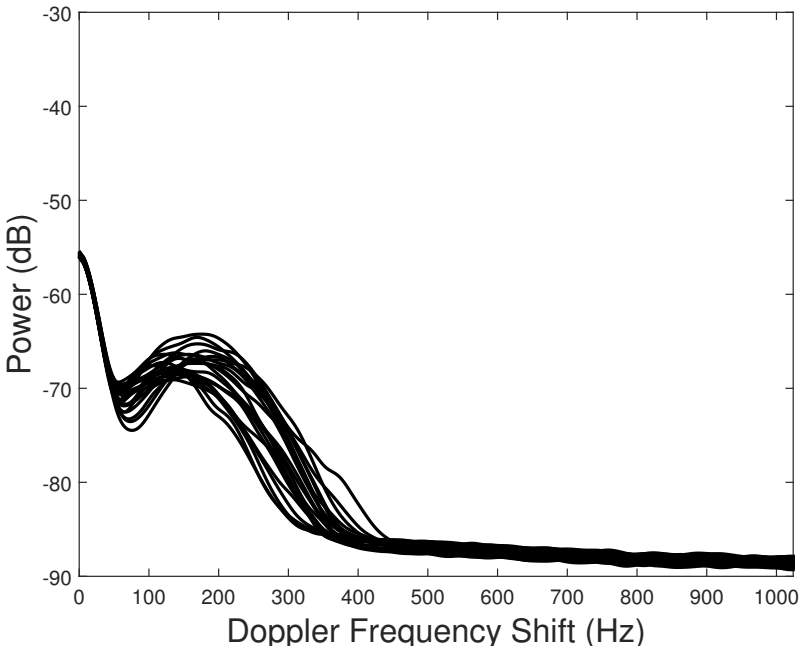

Figure 2.5: An example of Pludix power spectra during a snow event.

ally replaced by velocity-mass relationship if ice particles are analyzed. Pruppacher e Klett (1978) report different velocity-mass relationship (see their tables 10.3b-10.5) as function of crystals (or aggregates) shape. Despite the not easy solution for the determination of unique relationship to estimate the ice particle fall speed, the maximum values measured do no exceed the 3 ms^{-1}. A fall speed of 3 ms^{-1} produces a Doppler frequency shift of 190 Hz, so that the interval 0-200 Hz can be considered the snow band. All these considerations are valid considering dry snow. If wet snow is present, the Doppler frequencies interested increase, due to the higher terminal velocity of particles, and can reach values also exceeding 300 Hz.

Terminal fall velocity of hail has been determined from different direct observations: Lozowski and Beattle (1979), made their measurements in Canada and found the relation $v = 12.43D^{0.5}$, while Knight and Heymesfield (1983) made their measurement

in Colorado (USA) and found the relation $v = 8.445D^{0.553}$ where $D(cm)$ is the hail diameter and $v(ms^{-1})$ is the fall speed. Other relationships are $v = 4.51D^{0.5}$ (Cheng and English 1983) or $v = 4.41D^{0.5}$ (Ulbrich and Atlas1982) where D is in mm. As for the snow, the hail terminal velocity is dependent from the ice density and this is reflected in the different relationships found.

The fall speeds of hail are able to generate Doppler frequencies shift higher than 600 Hz. Typical Pludix power spectra in presence of hail are that show in figure 2.6. If

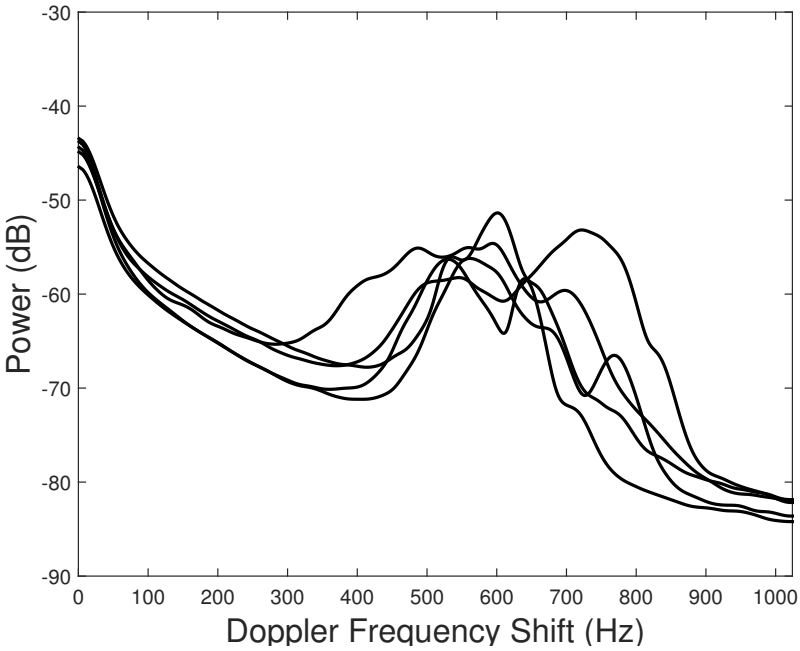

Figure 2.6: An example of hail Pludix power spectra.

hailstones are present in a rainy precipitation the Pludix power spectrum presents secondary maximum at very high frequencies (if the hail size is very large the Doppler shift can also exceed 1000 Hz). The spectrum shape becomes multi-modal with asymmetric peaks because of the inhomogeneous distribution of hail size.

Here, the description of Pludix power spectrum characteristics is limited to the more

frequent precipitative events (rain, snow, hail), but all the other conditions (i.e. mixed precipitation) can be detected by Pludix generating a variety of Doppler spectra that can be considered as an overlapping of those above described.

2.2.2 2DVD

The 2DVD - Two Dimensional Video Disdrometer (Kruger and Krajewski, 2002; Schnhuber et al., 2007) measures size, fall velocity and shape of each hydrometeor that falls in its sampling volume. The 2DVD measurement principle is based on two high speed line scan cameras, that are placed orthogonally to each other, creating the approximately 10×10 cm^2 virtual measurement area. The actual version of 2DVD consists of three main units, the Sensor Unit (SU), the Outdoor Electronics Unit (OEU) and the Indoor User Terminal (IUT). The first 2DVD version was taller than the actual and Nespor et al. (2000) indicated that wind induced measurement errors, caused by the shape of the instruments, were present. Consequently, the shape was modified until to the actual more compact version. The figure 2.7 shows the SU (truncate pyramid shape) and the OEU (rectangular shape) of 2DVD, where the former has vertical dimension very smaller with respect the first 2DVD version to avoid error measurements due to the wind effects.

A light source generates a light sheet that is projected onto a line-scan camera that has a single line of 512 photodetectors that are read out at a rate of 34.1 kHz, creating slices of the image projection. The light sheets are intense and particles falling through them cast shadows on the photodetectors. The photodetector signals are compared against a threshold to determine if a pixel is lit or obscured and in this regard, the 2DVD is calibrated by dropping calibration spheres ranging from 0.5 to 10mm in diameter. The combination of bright light and video thresholding renders the raindrops opaque, and

Figure 2.7: The Sensor Unit and the Outdoor Electronics Unit of the 2DVD. Schonuber (2007).

makes the 2DVD insensitive to ambient light. The two orthogonal projections provide, in principle, three-dimensional raindrop shape information. The light sheet width is 10 cm, so that each photodetector corresponds to 0.1953 mm. The photodetector output is compared to a threshold level and if a pixel value exceeds the threshold, the 2DVD treats the pixel as obscured. The number of obscured pixels determines the size of an hydrometeor.

Shape informations allow computation of the drop volume and equivalent drop diameter D, as well as the oblateness and the effective measuring area of drop and these quantities are necessary to derive the DSD and RR. The 2DVD is also able to calculate the terminal fall velocity of hydrometeors by measuring the time the particle takes for proceeding from camera A (upper system) to camera B (lower system). The distance of the two optical planes is set to around 6.2 mm and then precisely measured by use of calibration spheres. To minimize quantization effects, the mean of time needed to the hydrometeor to pass through the two optical planes both incoming and exiting each of

two planes, is considered. Once that the terminal fall speed is calculated, the particles are filtered out if the measured fall speed is faster or slower than ±50% of the Gunn and Kinzer (1949) observations.

Since the 2DVD measures the drops one by one, is possible to classify them into classes of requested width. Generally, the DSD is calculated over 50 classes 0.2 mm width, using the following relationship:

$$N(D_i) = \frac{1}{A_i \cdot v_i \cdot t \cdot \Delta d_i} \tag{2.7}$$

where $N(D_i)$ indicates the number of drops per cubic meter per millimeter of i-th diameter class, A_i is the effective measuring area of drop, v_i is the terminal fall speed (measured by the instrument or calculated by 2.3) and t is the integration time (one minute typically). The contribution of each drop to the RR is calculated as follow, and then the contributions of all drops falling in the integration time are summed up:

$$RR_i = 3600 \frac{V_i}{A_i \cdot t} \tag{2.8}$$

where RR_i is the rainfall rate due to the i-th drop, V_i is the drop volume in mm^3 and A_i and t are always the effective measuring area of drop and the time integration, respectively.

The 2DVD provides the most detailed information about the individual hydrometeors, despite recent comparative studies revealed that the 2DVD often underestimates the drop concentration for the sizes less than 0.5 mm in diameter (Tokay et al., 2013). The 2DVD data viewer menu presents the image of the hydrometeors in two measuring planes as shown in the figure 2.8.

Figure 2.8 represents a screen dump of the data viewer main menu, showing in the

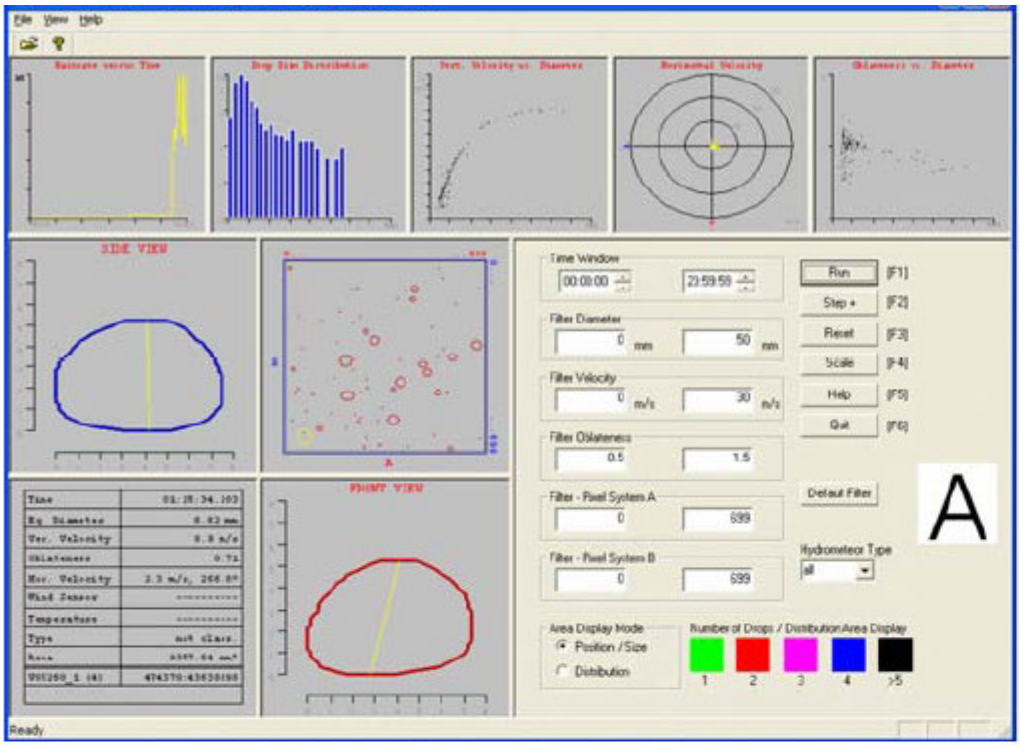

Figure 2.8: A screen shot of 2DVD. Schonuber (2007).

bottom panel the particle front contour, in the middle panel the particle side contour and a virtual top view of the measuring area, and in the top panel the five sub-menus with representations for rain rate, drop size distribution, fall velocity, an estimate for horizontal velocity of raindrops, and particles height/width ratio.

2.2.3 Particle Size Velocity disdrometer (Parsivel)

The Particle Size Velocity disdrometer - Parsivel is a laser-optical disdrometer manufactured formerly by PMTech and recently it has been resigned by OTT (Parisvel^2), and it is intended for hydrometeor size and fall speed measurements. Parsivel^2 is an upgraded version of the Parsivel where measurement accuracy at both small and large

drop end is noticeably better in new model (Tokay et al., 2014b). The disdrometer consists of an optical sensor, where a transmitter emits a laser sheet that is received by a photodiode, within a housing and some appropriate electronics. Parsivel can measure sizes up to about 25 mm and uses 32 size classes of different widths, spread over 0-26 mm. The lowest two size classes are not used at all because of their low signal-to-noise ratio. Registration starts only at the lower size bound of class 3 (0.25 mm). As for the particle size, the velocity is subdivided into 32 uneven classes, starting from 0 and reaching up to 22.4 ms^{-1} (upper margin of class 32), thus, Parsivel stores particles in 32x32 matrices. The temporal resolution is generally set to one minute but the new OTT version, Parisvel^2, is capable to increase the resolution time up to 10 s). The figure 2.9 shows a picture of installed Parsivel. The optical sensor of the instrument

Figure 2.9: A picture of Parsivel.

is a commercially available 780-nm laser diode with a power of 3 mW, producing a horizontal sheet of light (30 mm wide and 1 mm high). The emitter and receiver are 160 mm apart. In the receiver the light sheet is focused onto a single photodiode. The transmitter and receiver are mounted in a housing for protection (see section 2c). In

the absence of drops the receiver produces a 5-V signal at the output of the sensor. Particles passing through the light sheet cause a decrease of this signal by extinction and therefore a short reduction of the voltage which amplitude is a measure of particle size, while the duration of the signal allows an estimate of particle velocity. To eliminate the effect of background light (e.g., sun), the laser is periodically pulsed, and the output signal is discretely sampled in time as the difference between two consecutive on and off state of the laser system (the sampling rate is 10 KHz for the older Parsivel version, while is 25 KHz for Parsivel^2). An appropriate algorithm to detect the start and the end of a signal is implemented in the software.

The particle diameter is calculated from the maximum shadowed area that is related to the maximum output voltage attenuation, assuming the shape of the particle is known. Because drops larger than 1 mm are not spherical, the calculation of the equivolume diameter is based on different axis ratio,x, (vertical over horizontal axis) relationships:

$$x = \begin{cases} 1 & D_{eq} \leq 1mm \\ 1.075 - 0.075 D_{eq} & 1mm < D_{eq} < 5mm \\ 0.7 & D_{eq} \geq 5mm \end{cases} \tag{2.9}$$

where D_{eq} is the equivolume sphere diameter. The 2.9 are valid for raindrops only because of their sphere-like shape, while if it is applied to other shapes (i.e. snowflakes) will produce errors in estimation of size and fall velocity. The Parsivel signal, which is the reduction of the output voltage, is directly related to the shadowed area that can

be calculated as follows:

$$S_{max} = \begin{cases} \pi ab & b \leq \dfrac{h}{2} \\ 2ab\left[\arcsin\left(\dfrac{h}{2b}\right) + \dfrac{h}{2b}\sqrt{1-\left(\dfrac{h}{2b}\right)^2}\right] & b > \dfrac{h}{2} \end{cases} \tag{2.10}$$

where a and b are the major and minor semiaxis of the spheroids, respectively and h is the height of laser sheet. Anyway, if $b \gg \dfrac{h}{2}$ the shadowed area S_{max} becomes $2a \times h$. The inversion of 2.10 is used to compute D_{eq} assuming
that $D_{eq} = 2ax^{\frac{1}{3}} = 2bx^{-\frac{2}{3}}$. However, the only dependable variable measured by Parsivel is the shadowed area, from which the instruments derived the equivolume diameter following the plot in figure 2.10.

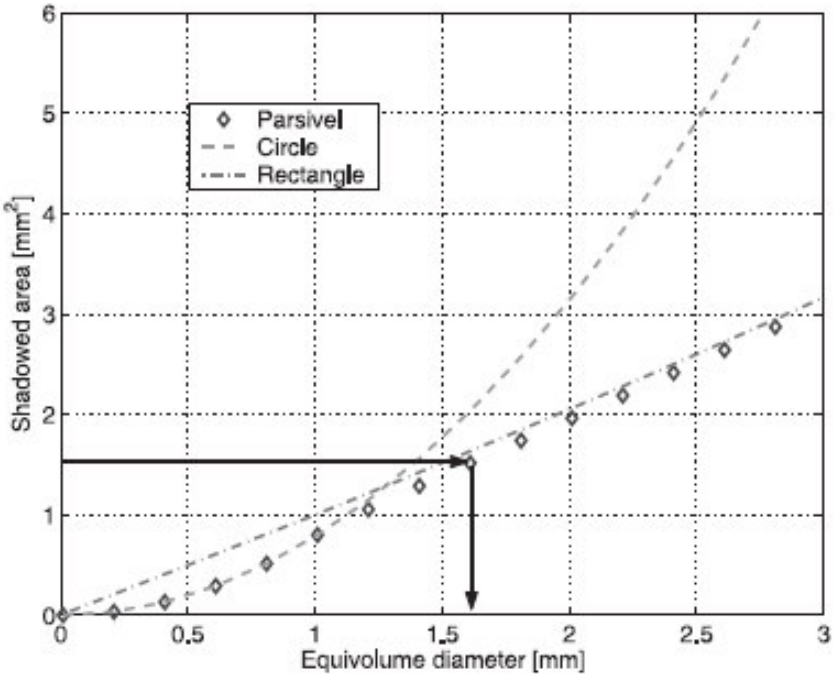

Figure 2.10: Equivolume diameter D_{eq} vs shadowed area S_{max} as estimated by the Parsivel software. Battaglia et al. (2010).

Again, the relationship shown by figure 2.10 is valid for raindrops only. Once that D_{eq} has been computed, all drops falling into a given class are assigned the values corresponding to the center of the size and velocity classes.

2.2.4 Micro Rain Radar (MRR)

The Micro Rain Radar (MRR) is a Continue Wave (CW) Frequency Modulate (FM) vertical pointing radar based on Doppler effect, that measures the signal backscattered by hydrometeors (METEK, GmbH, 2004). It is able to determine the vertical profile of DSD, which is obtained by analyzing the Doppler spectrum recorded, and, as derivative quantities, rainfall rate, reflectivity, liquid water content, fall velocity and other parameters. All the quantities are calculated at each gate. The vertical resolution is variable (it can be set between 10 and 1000 m) and depends on the maximum height to investigate, with the gates number fixed to 31. The power spectrum is calculated every ten seconds and the other quantities can be averaged over different time intervals ranging from 10 to 3600 seconds.

The core component of the radar is a frequency modulated gunn-diode-oscillator with integrated mixing diode and nominal transmit power of 50 mW. The instrument is a monostatic linear polarized radar and is composite of the antenna (parabolic dish of 60 cm of diameter) that is connected the transceiver unit; a commercial pc is necessary to put the instrument in operation. The antenna design allows rainwater to drain without building ponds. In order to avoid disturbances from snow on the antenna dish, optional antenna heating is offered.

The MRR operates with electromagnetic radiation at a frequency of 24 GHz with a modulation depending to the height resolution (e.g. with 300 m 10 m resolution, the modulation ranges from 0.5 MHz to 15 MHz). The spectral analysis of the received

Figure 2.11: A picture of MRR.

signal yields a power spectrum (25 per second averaged every 10 s) which is spread over a range of frequencies lines corresponding to the Doppler frequencies of the signal. Using known relations between fall velocity, rain drop size and scattering cross section the drop spectrum (or drop size distribution) is derived. The integration over the entire drop size distribution results in different parameters, like rain rate, liquid water content, etc.

The calculation of the DSD from the raw spectral power received by the MRR requires some easy mathematical steps. The raw spectral power is calculated as follow:

$$f(n,i) = \frac{10^{20} TF(i)}{C} \frac{1}{i^2 \Delta h} \eta(n,i) \tag{2.11}$$

where $TF(i)$ and C are the transfer function and calibration radar constant, respectively, Δh is the range resolution, i is the number of range gate, n is the line number of Doppler spectrum related to the modulation and $\eta(n,i)$ is the spectral reflectivity. To obtain the DSD is necessary to introduce the spectral reflectivity density calculated

with respect the drop diameter $\eta(D,i)$) that is related to the spectral reflectivity $\eta(n,i)$ as follows:

$$\eta(D,i) = \eta(v,i)\frac{\partial v}{\partial D} = \frac{\eta(n,i)}{\Delta v}\frac{\partial v}{\partial D} \tag{2.12}$$

where $\eta(v,i)$ is the spectral reflectivity density with respect the fall velocity and Δv is the fall velocity resolution. Since the MRR is a vertically pointing radar, the fall velocity of drops will be function of air density, and consequently of the altitude, according what to Foote and du Toit (1969) found, that is, $v \propto \rho^4$ where ρ is the air density (Beard, 1977, found a more complex relationship between fall velocity and air density and viscosity that leads a different results with respect to Foote and du Toit (1969), but this will be analyzed in more detail in the next chapter). The MRR software uses a second order approximation to calculate the fall velocity as function of altitude:

$$v(D,h) = v(0)\delta h = v(0)(1 + 3.68 \cdot 10^{-5}h + 1.71 \cdot 10^{-9}h^2) \tag{2.13}$$

where v(0) is the terminal fall speed at sea level calculated according the 2.3. At this point the DSD for each gate can be estimated:

$$N(D,i) = \frac{\eta(D,i)}{\sigma_b(D)} \tag{2.14}$$

where $\sigma_b(D)$ is the backscattering cross section of drop with diameter D. The DSD is divided in 64 classes, corresponding to the number of Doppler spectrum deriving from the modulation, of variable width also as function of gate number.

2.2.5 Joss-Waldvogel (JW)

The Joss-Waldvogel (JW) is an impact disdrometer was originally developed by Joss and Waldvogel (1967) and is manufactured by Distromet of Basel, Switzerland. The JW is able to transform the vertical momentum of an impacting raindrop into an electric pulse whose amplitude is a function of the drop diameter. It consists of a sensor and signal processing electronics. The sensor has a sampling cross section area of 50 cm^2 covered by styrofoam cone. The standard output of the JW is the number n_i of drops of diameter D_i that are sorted into 20 size intervals ranging from 0.3 to5.6 mm diameter. The boundaries of the 20 channels are not uniform and increase with drop size from 0.1 mm to about 0.5 mm. The temporal resolution is 30 s or 1 min. To compute the drop size distribution, the quantity $N(D_i)$, the number density of drops with diameters corresponding to size class i per unit volume, must first be calculated from the data for every drop size class, according to the following formula:

$$N(D_i) = \frac{n_i}{A_i \cdot v(D_i) \cdot t \cdot \Delta d_i} \tag{2.15}$$

where where n_i is the number of drops measured in drop size class i; D_i is the central diameter of the drops in size class i (mm); A is the size of the sampling area (50 cm^2); t is the time interval for one measurement (usually set to 60 s); $v(D_i)$ (ms^{-1}) is the fall velocity of a drop with the diameter D_i; ΔD_i is the diameter interval of drop size class i (mm). For the terminal velocity, the well-known Gunn and Kinzer (1949) formula is used.

The JW was originally designed for the purpose of calculating radar reflectivity factor. The JW is a reliable instrument that can be operated continuously and unattended. However, it does have three shortcomings: first, it underestimates the number of small drops in heavy rain. Second, it cannot resolve drop sizes larger than 5.6 mm diameter.

Third, its calibration assumes that the raindrops are falling at terminal velocity in still air. Another sources of error is due to the ringing of the styrofoam cone when it is hit by large drops (known as the disdrometer dead time). This effect cannot be reduced by any preventive measure, but it can be corrected by mathematical methods.

Figure 2.12: A picture of JW.

2.3 Field campaigns

Data collected in different field campaigns have been used for this Thesis. Not only DSD data have been analyzed, but also Doppler power spectra, specifically Pludix and MRR data, rainfall rate, reflectivity and other integral DSD parameters. Sometimes, depending on the specific purpose, the data have been screened out imposing a threshold (generally on the rainfall rate values). Since the aim of this Thesis is the study of the collisional break-up and the spatial variability of DSD, the datasets and data types used for each analysis are different.

About the collisional break-up, the analysis can be divided in two parts: in the first part only the Pludix power spectra have been analyzed, while in the second part the

DSD collected by different instruments are used. For both the analysis, from the original datasets only the minutes exceeding a RR threshold have been considered, but while for the part regarding the Pludix power spectra analysis the threshold value was $8mmh^{-1}$, for the second part the threshold value was $5mmh^{-1}$.
Shown below the characteristics of field campaign which data were used with a brief description of peculiarities advantages/problems related to each one.

Instrument	**Location (lat,lon)**	**Altitude (m a.s.l.)**	**Minutes RR > 8mmh^{-1}**	**Duration (MM/YY)**	**Organizer**
Pludix	Linzhi 29.77°N, 94.74°E	3300	412	10/09-09/10	CEOP-AEGIS
Pludix	Lhasa 29.65°N, 91.03°E	3600	6	10/09-09/10	CEOP-AEGIS
Pludix	Wasserkuppe 50.29°N, 9.56°E	910	199	12/00-01/03	DWD
Pludix	Ferrara 44.5°N, 11.37°E	15	169	04/02-06/03	Permanent

Table 2.1: Field campaigns description of Lhasa-Linzhi (Tibet), Wasserkuppe (Germany) and Ferrara (Italy).

The table 2.1 describes the field campaigns characteristics reporting the instrument used, the location, the altitude of location, the number of minutes getting RR over the threshold (8 mm^{-1} for this case), the duration of the campaign and the organizer of the campaign. The three field campaigns described here were carried out at the really different altitude and their duration ranges from 11 months (Linzhi dataset) to about 2 years (Wasserkuppe dataset). In particular the field campaign in Linzhi gave the opportunity to collect, for the first time, DSD data at ground level at very high altitude, since the instrument was installed on the Tibetan Plateau (TP). The disdro-

metric campaign was carried out over the TP from November 2009 to September 2010 in the frame of CEOP-AEGIS (Coordinated Asia-European long-term Observing system of Qinghai-Tibet Plateau hydro-metOeorological processes and the Asian monsoon systEm with Ground satellite Image data and numerical Simulations), a Collaborative EU Project funded under FP7. The CEOP-AEGIS is an international cooperation project between Europe and Asia to improve knowledge on hydrology and meteorology of the Tibetan Plateau and its role in climate, monsoon and extreme meteorological events. Another Pludix was installed in Namco (4700 m a.s.l.; 30.77°N, 90.99 °E) in the central-eastern part of the Plateau (see Figure 1), to study precipitation characteristics over the Plateau. Unfortunately, due to a malfunction and the very rare occurrence of liquid precipitation, the Namco disdrometer was able to operate in very few rain cases, and was not considered in this study. The Pludix installed in Lhasa had some technical problems too and its contribution to the field campaign dataset is limited, so that we refer to Linzhi dataset for simplicity.

The Wasserkuppe campaign was organized by the Deutscher Wetterdienst (DWD) with the aim to test several instruments as Present Weather Sensor (PWS). The PWS is an instruments able to automatically describe the weather conditions according to the World Meteorological Organization (WMO) codes (Prodi et al., 2011). Official reports of Wasserkuppe campaign consists of data from various sources (Bloemink and Lanzinger, 2005). A number of instruments report the precipitation intensity (mm h^{-1}), the 2m air temperature (°C), the 2m relative humidity (%), the 2m wind speed (ms^{-1}) and the dew point temperature (°C), and someone the WMO codes also. Moreover, a human observer reported, with 1-minute time resolution, the weather condition according the WMO codes.

The Ferrara dataset was obtained collecting data by a Pludix permanently installed on the roof of the University. Unfortunately it didn't work continuously during the period

reported in table 2.1 and this did not allow to have a great number of minutes to analyze.

In addition to these, the data collected during HyMeX field campaign have been also analyzed for this first part of the work. HyMeX (HYdrological cycle in the Mediterranean EXperiment) aims at a better understanding and quantification of the hydrological cycle and related processes in the Mediterranean, with emphasis on high-impact weather events, inter-annual to decadal variability of the Mediterranean coupled system, and associated trends in the context of global change. The data collected by both Pludix and 2DVD and MRR also at three measuring sites have been analyzed. One site was in center of Italy, La Sapienza (LS) - Rome (41.90°N, 12.51°E, 45 m a.s.l.), while the other two ,Silandro (46.63°N, 10.78°E, 720 m a.s.l.) and Trafoi (46.60°N, 10.55°E, 1570 m a.s.l.), were in the north of Italy. At LS site were installed one Pludix, one 2DVD and one MRR, while a 2DVD and a MRR were installed at Silandro and Trafoi sites, respectively.

According with the rain rate threshold (8 mmh^{-1}) used to select the data of table 2.1, the dataset of each HyMeX site results in the following minutes: Pludix, LS - 73 minutes, 2DVD, LS - 141 minutes, MRR, LS - 196±37 minutes[1], Trafoi, MRR - 202±98 minutes[2], Silandro, 2DVD - 71 minutes. In addition, also 667 minutes collected with a JW permanently installed on the roof of the University of Ferrara (not included in the HyMeX field campaign) have been analyzed.

The second part of break-up study concerned the only DSD analysis.The data that are used in this analysis were collected by 2DVD and Parsivel[2] in six different field campaigns that are conducted under Global Precipitation Measurement (GPM) mis-

[1]For MMR data the number of minutes has been estimated calculating mean and standard deviation over all radar levels, because each level has different number of minutes exceeding the threshold considered.

[2]

sion, ground validation (GV) program (Hou et al., 2014). The number of instruments, the seasonality, the location, and the duration of the field studies vary from one site to another and are listed in table 2.2. The first column of table 2.2 reports also the city of operational center of each campaign, while the instruments were collocated at various distances ranging from hundred meters to about 110 km. The size of the datasets used in this study ranged from about 140 minutes during Light Precipitation Validation Experiment (LPVEX) to the about 4200 minutes during Iowa Flood Studies (IFLOODS) as noted in table 2.2. The Parsivel^2 data were collected in three of the six field campaigns and the dataset size ranges from about 6500 minutes of Wallops Flight Facility (Wallops) to about 9400 minutes of Integrated Precipitation and Hydrology EXperiment (IPHEX). For the other three sites, Parsivel (previous version of Parsivel^2) is operated. Since data quality of Parsivel^2 is significantly better than old model (Tokay et al., 2014b), we decided to do not use the Parsivel data.

Both for 2DVD and Parsivel^2 the RR threshold used was 5 mmh^{-1} instead of 8 mmh^{-1} used for Pludix analysis. The availability of several instruments allowed to collect, in such cases, very large datasets. Two of these six datasets were used for the DSD spatial variability too, namely Wallops and MC3E, since the distances between the instruments allow to analyze the spatial variability at small scale. About that analysis a threshold was imposed both for RR and reflectivity at K_a and K_u band, but these aspects will be detailed treated in the dedicated chapter.

The IFLOODS is a ground measurement campaign taking place in eastern Iowa. The goals of the campaign are to collect detailed measurements of precipitation at the Earth's surface using ground instruments and advanced weather radars and, simultaneously, collect data from satellites passing overhead. The ground instruments characterized precipitation (the size and shape of raindrops, the physics of ice and liquid particles throughout the cloud and below as it falls, temperature, air moisture, and

distribution of different size droplets) to improve rainfall estimates from the satellites, and in particular the algorithms that interpret raw data for the GPM mission's Core Observatory satellite, launched in February 2014.

The MC3E campaign took place near Lamont, Oklahoma. The experiment was a collaborative effort between the U.S. Department of Energy (DOE) Atmospheric Radiation Measurement (ARM) Climate Research Facility and the NASA's GPM mission GV program. GPM field campaign objectives were to collect a comprehensive set of observations describing precipitation microphysics over continents during the warm season. The observations are used to refine GPM retrieval algorithms over land. At the same time, DOE objectives focused on relating the cloud microphysical observations to accompanying observations of cloud-kinematics and the surrounding environment.

The IPHEX is a ground validation field campaign that took place in the southern Appalachian Mountains in the eastern United States. IPHEx is co-led by NASA's GPM mission, with partners at Duke University and NOAA's Hydrometerological Testbed. The field campaign had two primary goals. The first is to evaluate how well observations from precipitation-monitoring satellites, including the recently launched GPM Core Observatory, match up to the best estimate of the true precipitation measured at ground level and how that precipitation is distributed in clouds. The second is to use the collected precipitation data to evaluate models that describe and predict the hydrology of the region.

The LPVEX campaign took place in the Gulf of Finland and collected microphysical properties, associated remote sensing observations, and coordinated model simulations of high latitude precipitation systems to drive the evaluation and development of precipitation algorithms for current and future satellite platforms. Specifically, LPVEX sought to characterize the ability of CloudSat, the GPM-DPR (Dual-Frequency Precipitation Radar), and existing/planned passive microwave (PMW) sensors such as

the GPM microwave imager (GMI) to detect light rain and evaluate their estimates of rainfall intensity in high latitude, shallow freezing level environments. Through the collection of additional microphysical and environmental parameters, the campaign also sought to better understand the process of light rainfall formation and augment the currently limited database of light rainfall microphysical properties that form the critical assumptions at the root of satellite retrieval algorithms.

NASA's Wallops Flight Facility, located on Virginia's Eastern Shore, was established in 1945 by the National Advisory Committee for Aeronautics as a center for aeronautic research. Today, Wallops is NASA's principal facility for management and implementation of suborbital research programs. In the six Wallops sites where 2DVD and Parsivel were installed, several other instruments are installed too, as rain gauges, radar, etc.

Field campaign	**Location**	**Duration**	**# of 2DVD and one-minute data ($> 5 mmh^{-1}$)**	**# of Parsivel² and one-minute data ($> 5 mmh^{-1}$)**
Iowa Flood Studies **(IFLOODS)** Iowa City and Waterloo, Iowa	42°N, 92°W	May to June 2013	6 - (4222)	14 (7520)
Midlatitude Continental Convective Clouds Experiment **(MC3E)** Ponca City, Oklahoma	36°N, 97 °W	April to June 2011	7 - (968)	/
Wallops Flight Facility **(Wallops)** Wallops Island, Virginia	37°N, 75°W	July 2013 to March 2014	6 (3912)	6 (6446)
Alabama Huntsville, **(Alabama)**	35 °N, 87°W	December 2009 to June 2010	3 (904)	/
Integrated Precipitation and Hydrology EXperiment **(IPHEX)** Ashville, North Carolina	35°N, 83°W	May to June 2014	5 (2114)	12- (9316)
Light Precipitation Validation Experiment **(LPVEX)** Helsinki, Finland	60°N, 24 °E	September to December 2010	3 - (134)	/

Table 2.2: Field campaigns description of IFLOODS, MC3E, Wallops, Alabama, IPHEX and LPVEX.

Chapter 3

Collisional Break-up: detection and analysis

The collisional break-up is one of the most important process in rain formation and affects substantially the microphysical structure of the rain layer. Many laboratory and experimental studies (Low and List, 1982a,b; McFarquhar, 2004; Prat and Barros, 2007) have been conducted to understand this phenomenon. These studies demonstrated that the shape of DSD moves away from log-normal trend when break-up is present, showing a two or three peaks spectrum at well defined diameters. The break-up, together with the other rain processes, have been introduced in Chapter 1, and in this Chapter will be reported the results obtained in the detection of break-up occurrence from ground based disdrometric measurements. The first step to study the break-up in natural rain focused on the analysis of Pludix power spectrum, that presents particular shape in correspondence of break-up occurrence. Then, the unprecedented availability of disdrometric datasets at different altitudes, allowed to study the effect of reduced air density on the break-up mechanism, and to asses the dependance of the break-up

diameter on the altitude, finding a limiting value of CKE. Since the study of break-up analyzing the Doppler power spectrum is possible only using instruments based on the Doppler effect (such as POSS, Pludix and MRR) and since most disdrometers are based on different measuring principle, the study has been focused on the DSD data analysis with the aim to detect the break-up occurrence by investigating the DSD directly. Finally, some case studies will be shown with the aim to individuate the development of break-up up to the reaching of the equilibrium DSD.

3.1 Pludix power spectrum

The Pludix output is the Doppler power spectrum obtained sampling the power backscattered by falling hydrometeors during one minute interval, as function of Doppler shift frequencies. The Doppler frequencies are function of the terminal fall speed of drops according to the equation 2.4. Figure 3.1 reports, as an example, some Pludix power spectra referred to sea level measurements during a rain event showing both rain (solid lines) and no-rain (dashed lines) minutes.

During the rain event the Doppler spectrum presents a bump generally between 200 and 600 Hz (these are the Doppler frequencies generated by falling drops at sea level), with the power peak ranging in this interval. The increse of power at low frequencies is an instrument noise, and it is screened out before the inversion process to estimate the DSD. The power is function of drops concentration and size and it is an indicator of the intensity of precipitation, the higher the RR the greater the backscattered power. The figure 3.1 shows also a sort of symmetry of the bump generated by rain with respect to the power peak, for few frequency intervals, and this feature will be relevant for our break-up detection purposes.

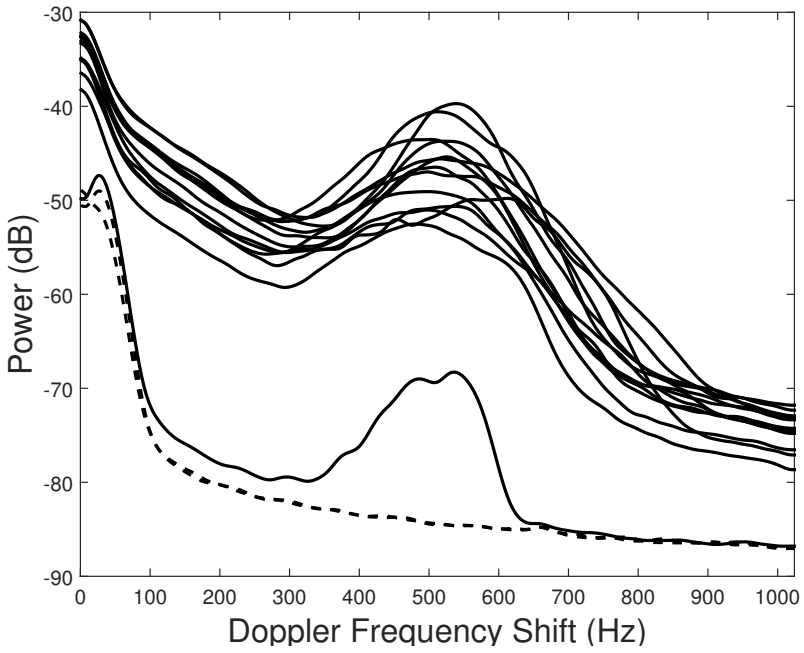

Figure 3.1: An example of Pludix power spectra during a rain event (solid lines). No-rain Doppler spectra are also shown (dashed lines). The x-axis reports the Doppler shift frequency (Hz) of falling drops, while the y-axis the power backscattered by the drops population.

3.2 Break-up detection algorithms

In this section will be reported the structure of the two algorithms developed to detected break-up occurrence in natural rain. The first one is based on the analysis of Pludix power spectrum only and can be applied only to instruments that give a Doppler power spectrum as output. Due to this limitation, it was mandatory to extend the break-up analysis to the instruments that measures DSD directly. This because of the most part of disdrometers are based on different working principles (2DVD, Parsivel, etc.) and their output is the DSD. So the second algorithm described here works on the DSD data.

3.2.1 Power Spectrum (PS) algorithm

In the Section 3.1 the characteristics of Pludix power spectrum have been described, highlighting the symmetry of the power peak obtained during a precipitative event. This property is lost when break-up is the dominant process and the Doppler spectrum shows an abrupt decrease of the power immediately after the power peak (i. e. an order of magnitude of power decrease in about 50 Hz, as estimated by Prodi et al., 2011). This feature is not easy to observe because of the scarcity of these events in natural rain. Figure 3.2 shows the differences between Pludix power spectra where break-up is dominant (dotted line) and where is not (solid line), resulting in a different shape of the maximum and in the slope of the power after it. The Doppler frequencies interested by the break-up phenomenon are usually those in the final part of "rain band", that is, around 600 Hz at sea level.

To automatically recognize the break-up signature in the Pludix power spectrum a simple algorithm (PS algorithm) has been written. Before to apply the algorithm, the Pludix power spectra are smoothed in order to screen out noise that can grow in the computation of the first derivative of the spectrum.

For each minute spectrum with rain rate larger than 8 mm h^{-1}, the normalized backward derivative of the received power with respect to the Doppler frequency is calculated in the interval 300-900 Hz, for the i-th frequency value, as follows:

$$\delta_i = \frac{p_i - p_{i+1}}{p_i} \frac{1}{\Delta f} \tag{3.1}$$

where p_i and p_{i+1} the backscattered power of i-th and (i+1)-th Doppler frequency, respectively and Δf is the frequency interval (1 Hz in this case). The choice to calculate the backward derivative (hereafter referred as "derivative") is to work with positive values in the region of interest. Generally, the derivative will assume a positive value

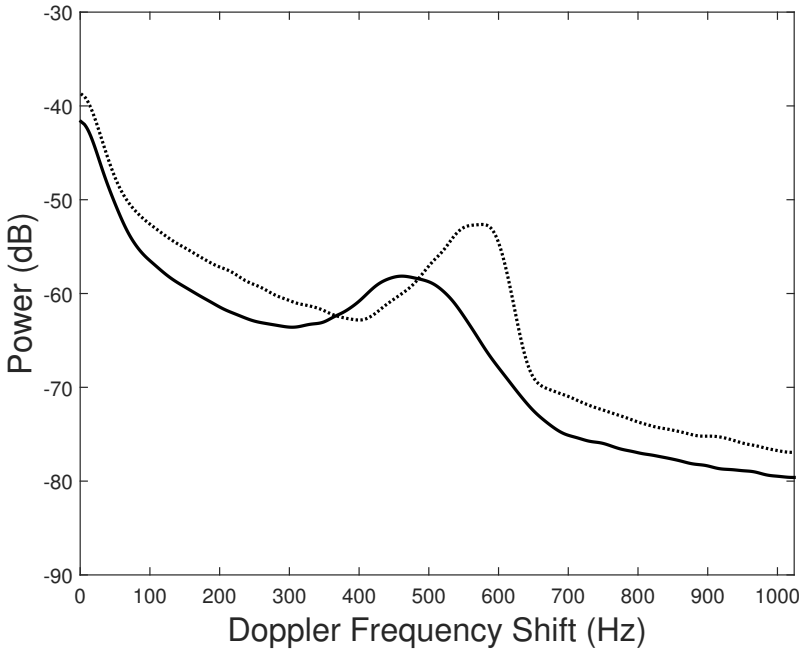

Figure 3.2: An example of Pludix power spectra with dominant break-up (dotted line) and non (solid line).

with higher values in correspondence of minutes dominated by break-up. The lower-end of the interval has been chosen at 300 Hz to check if the break-up phenomenon may occur at small diameters, while the upper-end has been chosen at 900 Hz in order to consider also cases where the dorp fall velocity are higher than the Gunn and Kinzer (1949) values, as it is for higher elevation data, as it will shown in the next Sections. To have more stable and robust values, the derivate value assigned to each frequency is calculated by averaging the eleven derivatives of the interval centered on the considered point, that is:

$$\delta_i = \sum_{n=i-5}^{i+5} \frac{\delta_n}{11} \tag{3.2}$$

The selected minutes are sorted according to the derivative values, from the lowest to the highest. The frequency corresponding to the power peak is selected as the fre-

quency for which the power starts decreasing, assumed as a robust indication of the drop size where break-up becomes significant for the considered minute. The underlying assumption for this choice is that, as the drop size and rain rate increase, both power and frequency of the peak increase, but the increase in frequency is limited by the break-up as the maximum drop size is reached.

3.2.2 DSD Spectrum (DS) algorithm

In the Chapter 1 has been analyzed in detail the signature of break-up on the DSD. As a result of break-up, drops around 1.5 mm are depleted, while there is an increase of small drops (less than 1 mm in diameter) and an increase of drops around 2-3 mm. The peak at small diameters is more marked than the one at larger size. It should be noted that it is impossible to recognize the break-up situations only by this feature because it could be due to other factors that occur within and above the precipitation layer. Not even the second peak, at larger diameter, represents a feature sufficient to recognize the break-up because can also be a product of coalescence (McFarquhar, 2004). The relative minimum and maximum in the range 1.0-2.6 mm can be taken as reference to identify the break-up.

To detect the break-up analyzing the DSD looking for the relative minimum and maximum in the range 1.0-2.6 mm, another simple algorithm (DS algorithm) has been written. The DS algorithm has been written for the DSD characteristics of Pludix (diameter bin width 0.3 mm) but has been applied, with the appropriate modifications, given the different diameter bin width of the other disdrometers, to the DSDs collected by the other instruments (2DVD, JW). The following description of the DS algorithm is referred to the DSD characteristics of Pludix:

- minutes with RR higher than 8 mmh^{-1} are selected;
- the point by point DSD spectrum normalized derivative between 1.55 mm and 2.45 mm diameter is calculated (ascending derivative);
- the point by point DSD spectrum normalized backward derivative for diameters larger than 2.45 mm is calculated (descending derivative);
- the ten minutes with the highest summation of ascending and descending derivative value are considered as break-up minutes;
- the central diameter of diametral class with the maximum descending derivative is considered as break-up diameter;
- finally the mean break-up diameter, with its standard deviation, is estimated for each considered minute.

The figure 3.3 shows the working principle of the DS algorithm.

3.3 Dependence of collisional break-up on altitude

The data analyzed with both PS and DS algorithm were collected at different altitude. While this aspect has not consequence for the application of DS algorithm, some implications about result for the application of PS algorithm. In fact, at altitude higher than sea level, the Doppler frequencies generated by the falling drops are greater due to the different air density. For this reason, the choice of 900 Hz as upper-end of Doppler frequency interval for the PS algorithm application is necessary for the analysis of spectra collected ad higher altitude (namely Wasserkuppe and Linzhi).

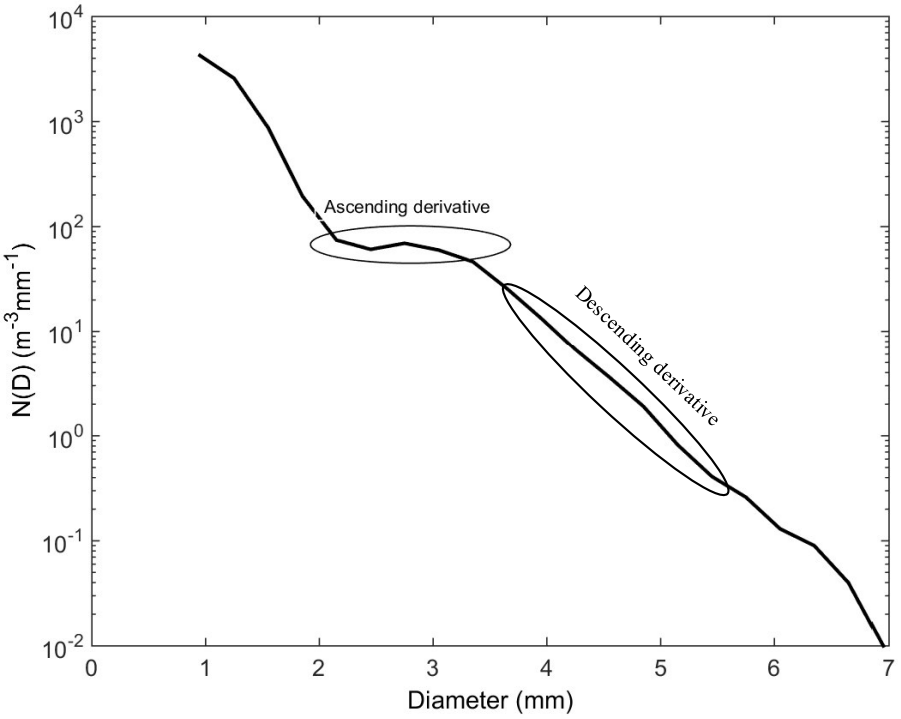

Figure 3.3: The ascending and descending derivative as individuated by DS algorithm.

There are empirical evidences that, for spheroidal shapes, the Drag coefficient (C_D), for high Reynolds numbers, does not change appreciably with the Reynolds number (Spilhaus, 1948; Kessler, 1969). Writing the C_D of a drop with mass M and diameter d as:

$$C_D = \frac{8M(\rho_w - \rho)g}{\rho_w \pi d^2 \rho v^2} \tag{3.3}$$

where g is the gravitational acceleration, ρ and ρ_w are the air and water density, respectively and v is the fall velocity of drop. Considering a change of altitude, the term $8M(\rho_w - \rho)g/\rho_w \pi d^2$ is constant and the assumption that also C_D is constant leads to

the relationship:

$$\rho v^2 = \rho_0 v_0^2 \tag{3.4}$$

where the subscript 0 refers to the sea level. The equation 3.4 shows that decreasing the air density, the terminal fall velocity of drops increases. An empirical relationship between rain drop diameter and terminal velocity at different altitudes was derived by Beard (1977), for drops with $40\mu m \lesssim d \lesssim 6mm$. The equation can be written in the form:

$$V = V_0(\alpha + \beta X) \tag{3.5}$$

with

$$\alpha = 1 + \epsilon_s(T) \tag{3.6}$$

$$\beta = \left[1.058 \cdot \epsilon_c(\rho) - 1.104 \cdot \epsilon_s(T)\right] / 5.01 \tag{3.7}$$

$$X = ln(D) + 5.52 \tag{3.8}$$

where V_0 is a basic state (sea level) velocity in m s^{-1} for saturated air at 1013 hPa and 20°C, T is the air temperature in Kelvin, ρ is the air density in kg m^{-3}, ϵ_s is the velocity deviation from Stokes drag and ϵ_c is the velocity deviation for a constant drag coefficient. At any level aloft, the values of α and β are computed from the simple expressions:

$$\epsilon_s(T) = \frac{\eta}{\eta_0} - 1 \tag{3.9}$$

$$\epsilon_c(\rho) = \left(\frac{\rho}{\rho_0}\right)^{\frac{1}{2}} - 1 \tag{3.10}$$

where

$$\eta \approx 1.832 \cdot 10^{-5} \{1 + 0.00266 [T(K) - 296]\} \tag{3.11}$$

$$\rho \approx 0.348 \cdot \frac{p(hPa)}{T(K)} \tag{3.12}$$

and η is the dynamic viscosity in kg m^{-1} s^{-1}, η_0 is the basic state dynamic viscosity at 1013 hPa and 20°C equal to $1.818 \cdot 10^{-5}$ kg m^{-1} s^{-1}, p is the static air pressure in hPa and ρ_0 is the basic state air density at sea level pressure and 20°C equal to 1.204 kg m^{-3}.

Foote and du Toit (1969) used another, but probably less accurate, form to calculate the terminal fall speed at arbitrary atmospheric conditions. The relation arises from the Davies data, reported by Sutton (1942) and also published by Best (1950) and estimates the terminal fall speed at any level aloft:

$$V(D) = V_0(D) \left(\frac{\rho_0}{\rho} \right)^{0.4} \tag{3.13}$$

where $V_0(D)$ is the terminal fall velocity calculated at sea level according to Gunn and Kinzer (1949), ρ_0 and ρ are the air density at sea level and at considered altitude respectively. Both using the Beard (1977) or Foote and du Toit (1969) approximation, the air pressure at a given altitude can be obtained or by measurements or by applying the equation valid for the standard atmosphere:

$$p = p_0 e^{-\frac{gZ}{RT}} \tag{3.14}$$

where p_0 is the atmospheric pressure at sea level at standard conditions, g is the gravitational acceleration in m s^{-1}, Z is the altitude considered in m, R is the universal

gas constant equal to 8.314 J mol^{-1} and T the temperature in K. Consequently, the air density ρ can be calculated from the relation $p = \rho RT$.

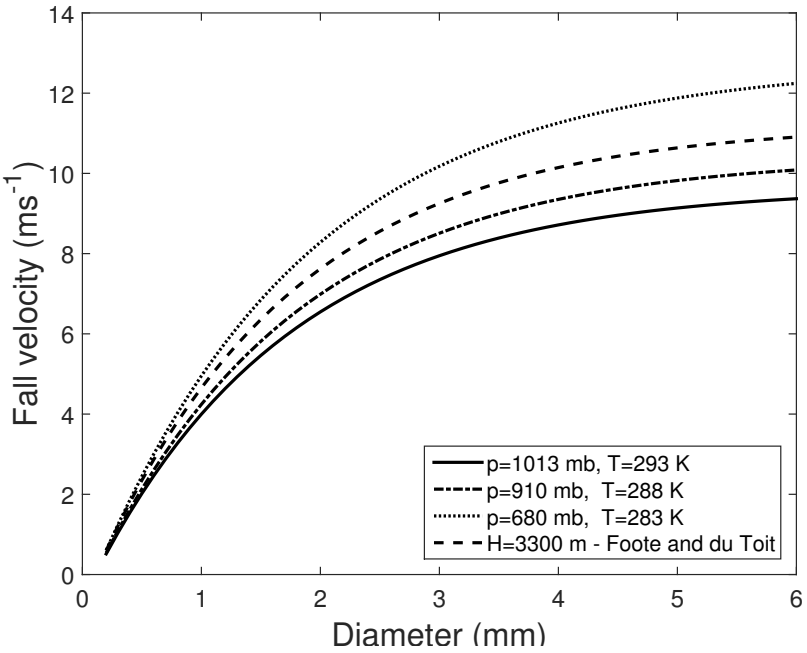

Figure 3.4: The v-D relationship calculated for the three datasets described in 2.1 according to Beard (1977). The v-D relationship for Linzhi altitude is calculated also according to Foote and du Toit (1969).

The figure 3.4 shows the v-D relationship for given p and T at Ferrara (solid line), Wasserkuppe (dash-dot line) and Linzhi (dotted line) according to equation 3.5. The equation 3.5 for given p and T at Ferrara reduces to the 2.3. The air pressure and temperature are obtained averaging the measurements carried out during the precipitative events in each of the three sites. These values are used to calculate the v-D relationship at Linzhi and Wasserkuppe also according to equation 3.13 (dotted and dash-dot line respectively). The terminal fall velocity, for a given drop diameter, increases increasing the altitude (i.e. for large diameter, at 680 mb is expected an increase of about 30% with respect the sea level). The Foote and du Toit (1969) v-D relationship, here cal-

culated for the Linzhi air density (dash line) underestimates the terminal fall velocity with respect to what obtained by Beard (1977) relationship, and we decided to use the latter because of its explicit dependence on the air temperature.

The fall velocity modification with altitude has consequences on the Doppler frequencies interested by falling drops. Consequently the frequency band limits are modified at Wasserkuppe and Linzhi. For this reason the upper-end limit of the PS algorithm has been chosen at 900 Hz. The table 3.1 reports the frequency band limits of Pludix for the corresponding diameter band limits for the three locations. The table 3.1 shows also that the width of the frequency intervals of the classes corresponding to the larger drop diameters, is lower than the width of the frequency intervals of the classes corresponding to the smaller diameters, regardless the location. For diameters larger than 6 mm diameter the corresponding Doppler frequencies are not reported because of the size limitation of Beard relation.

	Frequency (Hz)		
D (mm)	**Ferrara**	**Wasserkuppe**	**Linzhi**
0.8	208	220	256
1.1	274	292	314
1.4	330	351	413
1.7	377	402	474
2.0	416	444	526
2.3	448	479	569
2.6	475	508	606
2.9	498	533	637
3.2	517	554	663
3.5	533	571	685
3.8	549	585	704
4.1	557	598	720
4.4	566	608	733
4.7	574	616	744
5.0	580	624	754
5.3	585	630	762
5.6	590	635	770
5.9	594	639	777
6.2	597		
6.5	599		
6.8	602		
7.1	604		

Table 3.1: Diameter and Doppler frequency limit of the 21 Pludix bands for sea level (Ferrara), 950 m a.s.l. (Wasserkuppe) and 3300m a.s.l. (Linzhi).

3.3.1 PS algorithm: results

The PS algorithm has been applied to the three datasets and the Pludix power spectra ranked according the derivative values. The figure 3.5 reports the ten Pludix power spectra with the highest derivative values according the PS algorithm.

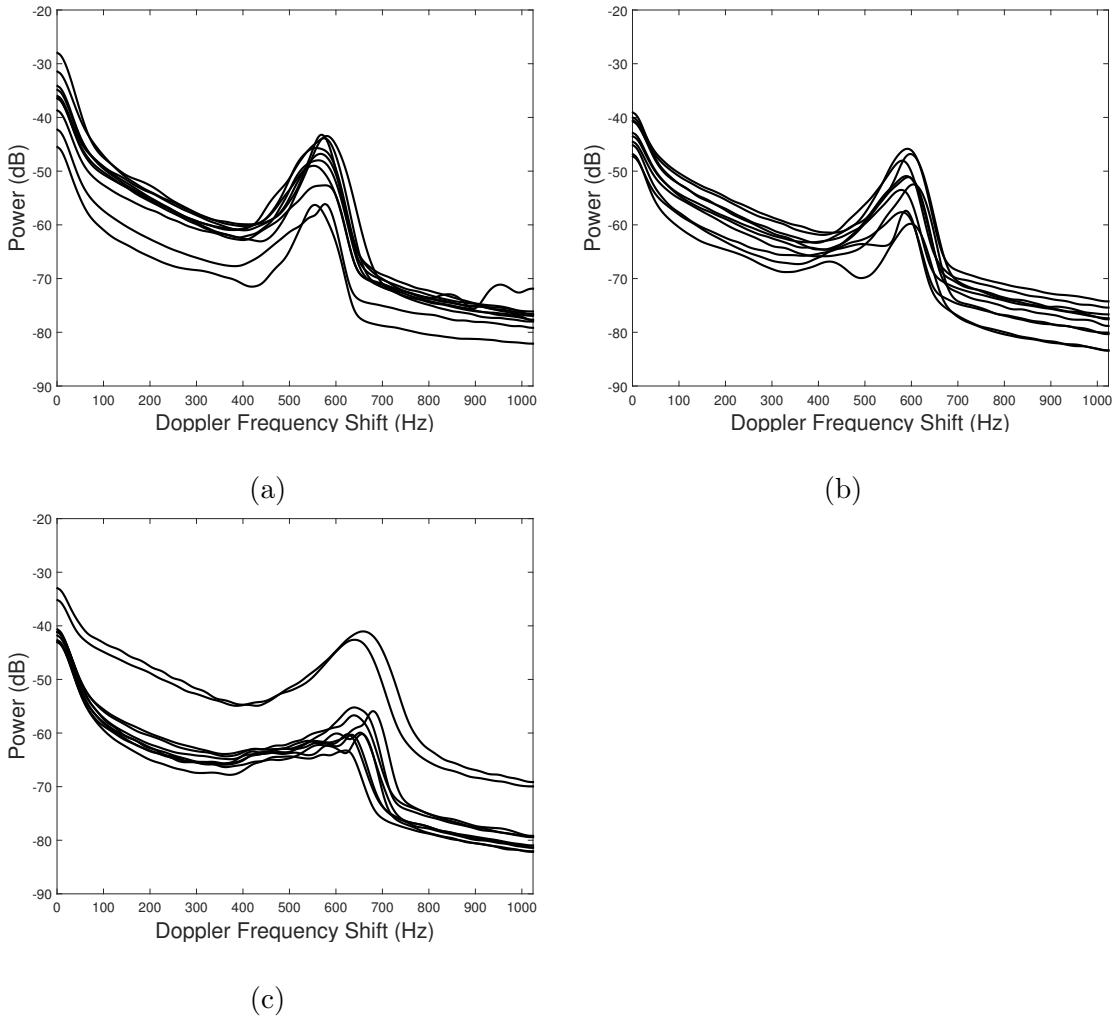

Figure 3.5: Pludix power spectra for 10 selected break-up minutes by PS algorithm in the (a) Ferrara, (b) Wasserkuppe, and (c) LinZhi experimental sites.

The maximum decrease of power spectrum occurs in a rather narrow frequency interval

for the three sites (figure 3.5), showing that these frequency limits might be regarded as a characteristic of the experimental site and, thus, the altitude. It can also be observed that the break-up power spectra are characterized by different power values, indicating that the phenomenon can occur at different rain rates. This is clearly evident for LinZhi data (figure 3.5c) where the power intensity for the two minutes is much higher than the others, but the break-up frequencies are very similar. The power spectra reported in 3.5a and 3.5b show slightly different shapes for the Linzhi site (figure 3.5c), except for the two more-intense minutes: here the drops are comparatively smaller and the backscattering cross sections are closer each other. Therefore, the spectra show a slow decrease (a sort of plateau) for frequencies smaller than the frequency of the power peak. At lower altitudes, drops are larger and the differences among backscattering cross sections are more marked, resulting in a sharper power peak, since the backscattering cross sections in the Mie theory depend on fifth and lower power of the drop radius.

To estimate the break-up diameter (the diameter derived from the frequency of the power peak), the V-D relationship has to be applied. At sea level, Ferrara site, the Gunn and Kinzer (1949) V-D relationship can be used, but for the other two sites is used the V-D relationship suggested by Beard (1977). Before to apply the V-D relationship, the terminal fall velocity of the frequency of the power peak is obtained from the equation 2.4 and an estimate of the break-up diameter at different heights can be obtained, as reported in 3.2.

In Table 3.2 the uncertainties estimated for each parameter are also reported. The standard deviation of the distribution of the power peak frequencies is considered as the uncertainty of the break-up frequency; this error is then propagated to velocity and diameter and reported. These uncertainties are originated by natural fluctuations of cloud microphysics and by the deviations of the environmental conditions from the

values reported in figure 3.4, used for the diameter retrieval.

Site	Alititude (m ASL)	f(Hz)	σ_f (Hz)	v (ms^{-1})	σ_v (ms^{-1})	D (mm)	σ_D (mm)
Ferrara	15	569	9	8.98	0.14	4.55	0.35
Wasserkuppe	950	587	10	9.25	0.16	4.02	0.32
Linzhi	3300	652	24	10.28	0.38	3.16	0.3

Table 3.2: Diameter and Doppler frequency limit of the 21 Pludix bands for sea level (Ferrara), 950 m a.s.l. (Wasserkuppe) and 3300m a.s.l. (Linzhi).

3.3.2 CKE limiting value

The effect of altitude is clearly to reduce the size of the break-up diameter, which decreases as altitude increases. Because the air viscosity and the water surface tension depend slightly on temperature, which is very similar in the three sites, the main factor affecting the break-up mechanism is air density: a reduction in air density results in an increase of the drop terminal velocity and thus in an increase in the kinetic energy of the collision between larger and smaller drops. Following Low and List (1982a), the break-up takes place when the CKE supplied to the system during the collision is not dissipated by the system itself by viscous deformation and oscillations of the merged drop, whose diameter of the equivolumetric sphere is $(D_S^3 + D_L^3)^{\frac{1}{3}}$. A detailed balance of the collision energy budget is hindered by the impossibility to properly define, both experimentally and theoretically, relevant features determining the budget. As an example, the difference between surface energy of the two drops before the collision and the drop after the collision may vary by one order of magnitude, depending on the drop shape, known to be strongly irregular and rapidly changing across and immediately

after the collision process. Furthermore, the drag on the drop surface depends on the drop shape and the section perpendicular to the motion direction. Finally, oscillations and internal circulation dynamics are also unknown for large, unstable drops close to their break-up size.

In this uncertainty frame, a strong constraint is provided, determining a reliable value for the maximum drop velocity, from which the break-up diameter can be straightforwardly derived, relying on well-established v-D relationships. These results can be exploited by estimating CKE (not dependent on the drop shape) for the three sites considered following the equation 1.2.

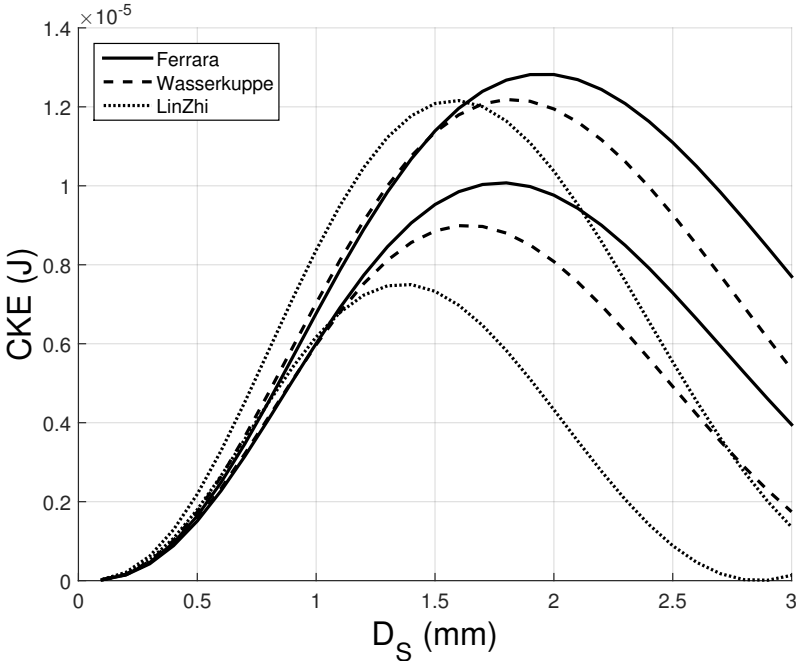

Figure 3.6: CKE (J) as a function of the D_S (mm) in the collision: for each site are plotted the curves for $D_L \pm \sigma_{D_L}$ (mm).

In figure 3.6 the CKE values for the three sites are plotted as function of D_S (mm) for the respective break-up diameters reported in table 3.2: two curves are reported for

each site, one for $D_L - \sigma(D_L)$ and one for $D_L + \sigma(D_L)$ to indicate the range of possible break-up drop sizes, within estimated uncertainties. The maximum CKE is reached when D_S is between 1.5 and 2.0 mm and its maximum value is similar for the three sites (within 5%), if $D_L + \sigma(D_L)$ curves are considered, indicating that a CKE of about $1.22\mu J$ is able to disrupt the drops regardless of the altitude and can be assumed as a limiting value of the kinetic energy that can be absorbed by a drop collision. Of course, the disruption may also occur for lower diameters, owing to the particular alterations of the break-up mechanisms that are likely to take place in real rain.

3.3.3 DS algorithm: results

The figure 3.7 shows the ten DSDs selected by the DS algorithm at Ferrara, Wasserkuppe and Linzhi analyzing the Pludix data. The results show a marked agreement with what the theoretical model find as equilibrium DSD (figure 1.9), with DSD that presents a relative minimum followed by a relative maximum in the diameter range 1.5-3.0 mm. The DSDs shape are very similar regardless the altitude with the relative increase in number of drops slightly marked at Linzhi site (figure 3.7c).

The figure 3.8 summarizes the estimated break-up diameter for all measurement sites using DS, PS or both techniques depending on the instrument type. For the sites where both DS and PS technique is applied, very close values of breakup diameter are found. The general trend of the graph shows a decrease of break-up diameter with altitude due to the reduced air density and viscosity that influences the size reached by drops. Referring to the legend in the figure 3.8, "LS" indicates La Sapienza site while "Plx" stays for Pludix. The 2DVD and JW data are analyzed by applying the DS algorithm while the PS algorithm has been applied to the MRR data. In particular, the MRR break-up diameter has been estimated averaging four consecutive levels so that just

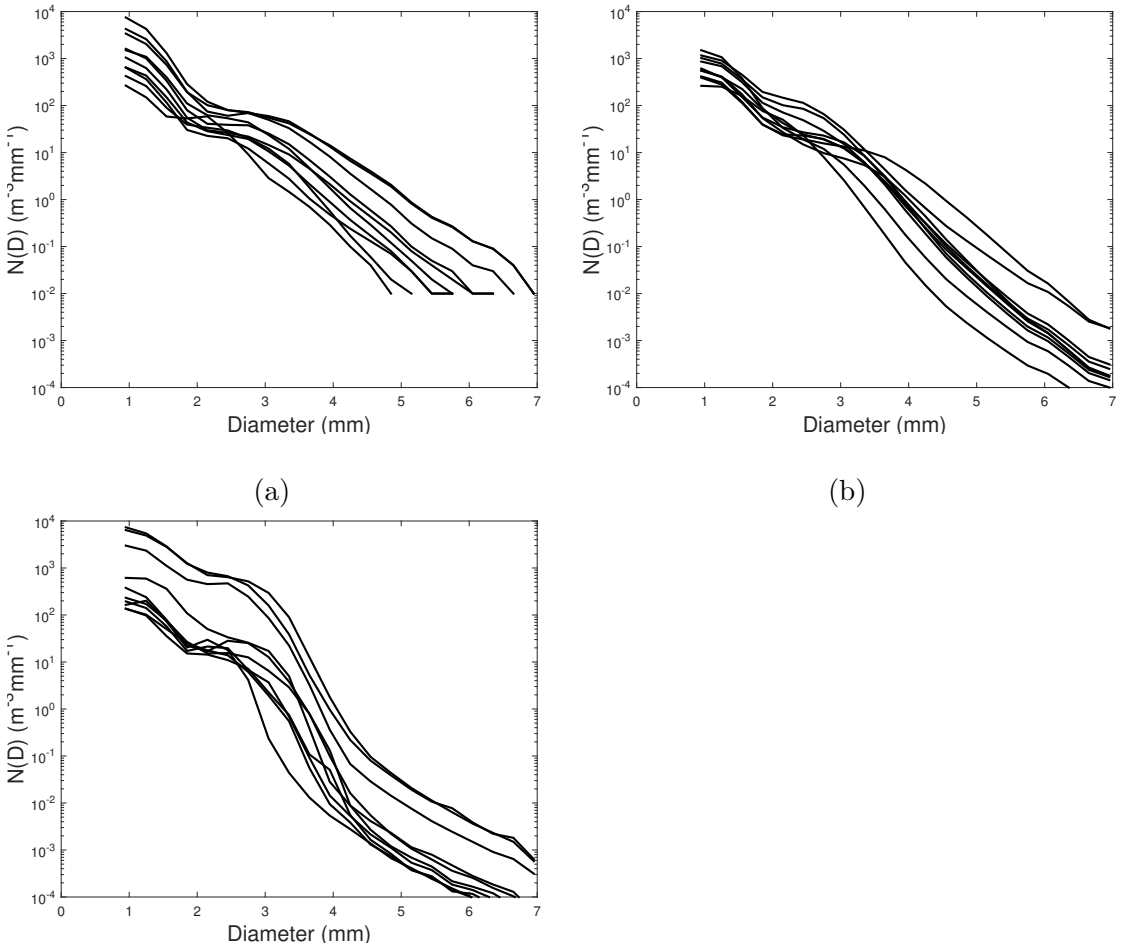

Figure 3.7: Pludix DSDs for 10 selected break-up minutes by DS algorithm in the (a) Ferrara, (b) Wasserkuppe, and (c) Linzhi experimental sites.

eight values of break-up diameter are found for the 1000 m investigated by the instrument. The break-up diameter was not estimated for each level because the vertical resolution of the instrument is 35 m and, substantially, there is not appreciable variation of break-up diameter for two consecutive levels. On the other side, estimating the break-up diameter averaging four consecutive levels, there is not a significant variation

in fall velocity of drops and in Doppler frequency generated, as well.

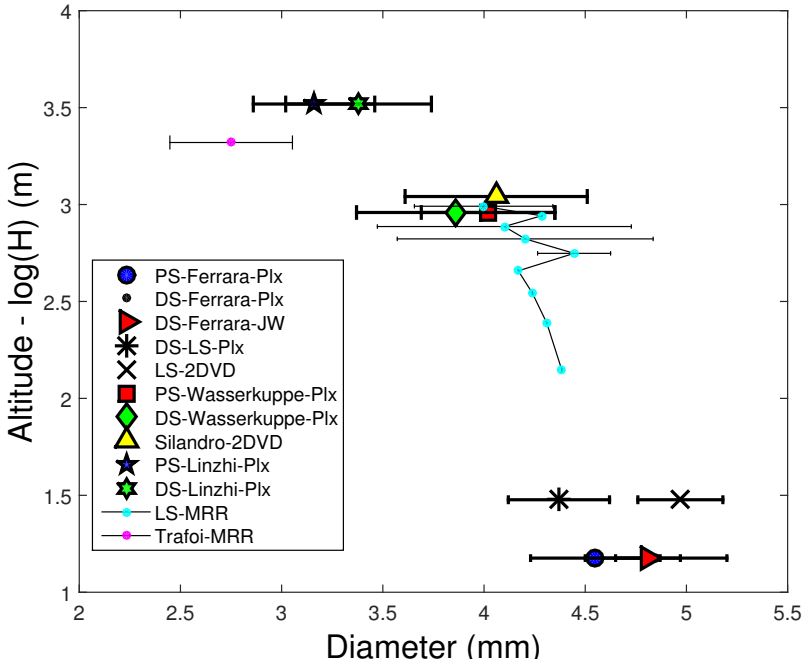

Figure 3.8: Trend of the estimated break-up diameter as function of altitude and algorithm applied.

To completion the analysis, the DSDs corresponding to the ten minutes selected as break-up by PS algorithm are reported for the Ferrara site. The figure 3.9 shows that the DSD shape is in good agreement with the findings of the DS algorithm and the theoretical models too. A very important feature resulting from DSDs selected as break-up by both PS and DS algorithm is their similarity, almost coincidence, with what theoretical models describe as equilibrium DSD (McFarquhar, 2004; Prat and Barros, 2007).

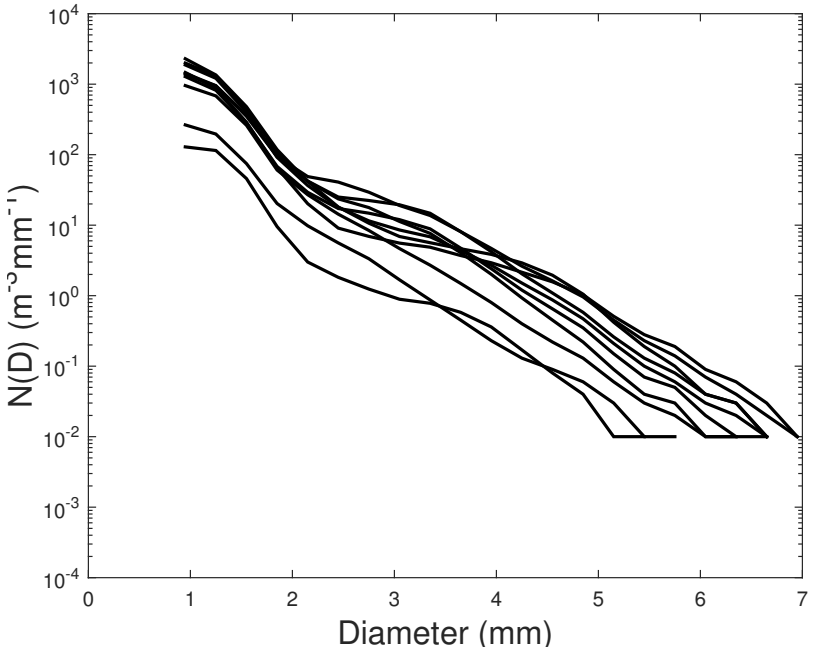

Figure 3.9: DSDs corresponding to the ten break-up minutes as selected by PS algorithm for the Ferrara site.

3.4 Break-up: case studies

In order to describe the evolution of different rain events, with particular emphasis to the development of equilibrium DSD, four case studies were selected from the Linzhi (three cases) and Lhasa (one case) stations as summarized in table 3.3. The choice of case studies over Tibetan Plateau is due to the greater ease in reaching the equilibrium DSD during a rain event.

The 1-minute Pludix data are averaged over 2 minutes for mainly convective, short lived cases (numbers 1 and 2 in table 3.3) and over 5 minutes for long lasting, mixed convective-stratiform cases (numbers 3 and 4). This was done as a trade-off between the need to analyze the fine temporal scale of the precipitation structure and the clar-

#	DD/MM/YY	Site	Type of rain	max RR (mmh^{-1})	RA (mm)
1	23/07/10	Lhasa	weak convective	12.15	1.35
2	9/07/10	Linzhi	deep convective	372.6	38.12
3	31/08/10	Linzhi	mixed	28.46	29.41
4	05/09/10	Linzhi	mixed	22.13	33.74

Table 3.3: Characteristics of the four case studies analyzed. The type of cloud/rain is assessed by looking also at satellite images.

ity of the DSD representation. The study was carried out by analyzing rain rate, DSD spectra, and Pludix power spectra. Here, only two cases are reported, namely the cases 2 and 3 on table 3.3, the former for the exceptional rain intensity recored, the latter for the clear evolution during its long duration.

29 July 2010

A large convective cluster developed in the early morning (local time) over the Linzhi area (Eastern TP). Satellite infrared images (not shown here) report cloud top minimum temperature around 205 K and the rain event lasted several hours. The system hit the Linzhi site at different stages and we concentrate our analysis on a single rain shower occurring between 15:30 and 16:00 UTC. In figure 3.10a the 2-min average rain rate is reported, showing a peak of about 370 mm h^{-1} and values above 10 mm h^{-1} for the rest of the time. The DSD spectra plotted in figure 3.10b show that the highest rain rate intensities (cyan tones) are due to an increase in drop numbers for all diameters, but especially around 1 mm and between 2 and 3 mm highlighting the presence of equilibrium DSD in this case. The DSDs before (blue lines) and after (red lines) the main rain rate shower are rather different in the number of drops larger than 1.5 mm, which is higher before the shower and markedly reduced after, possibly due to

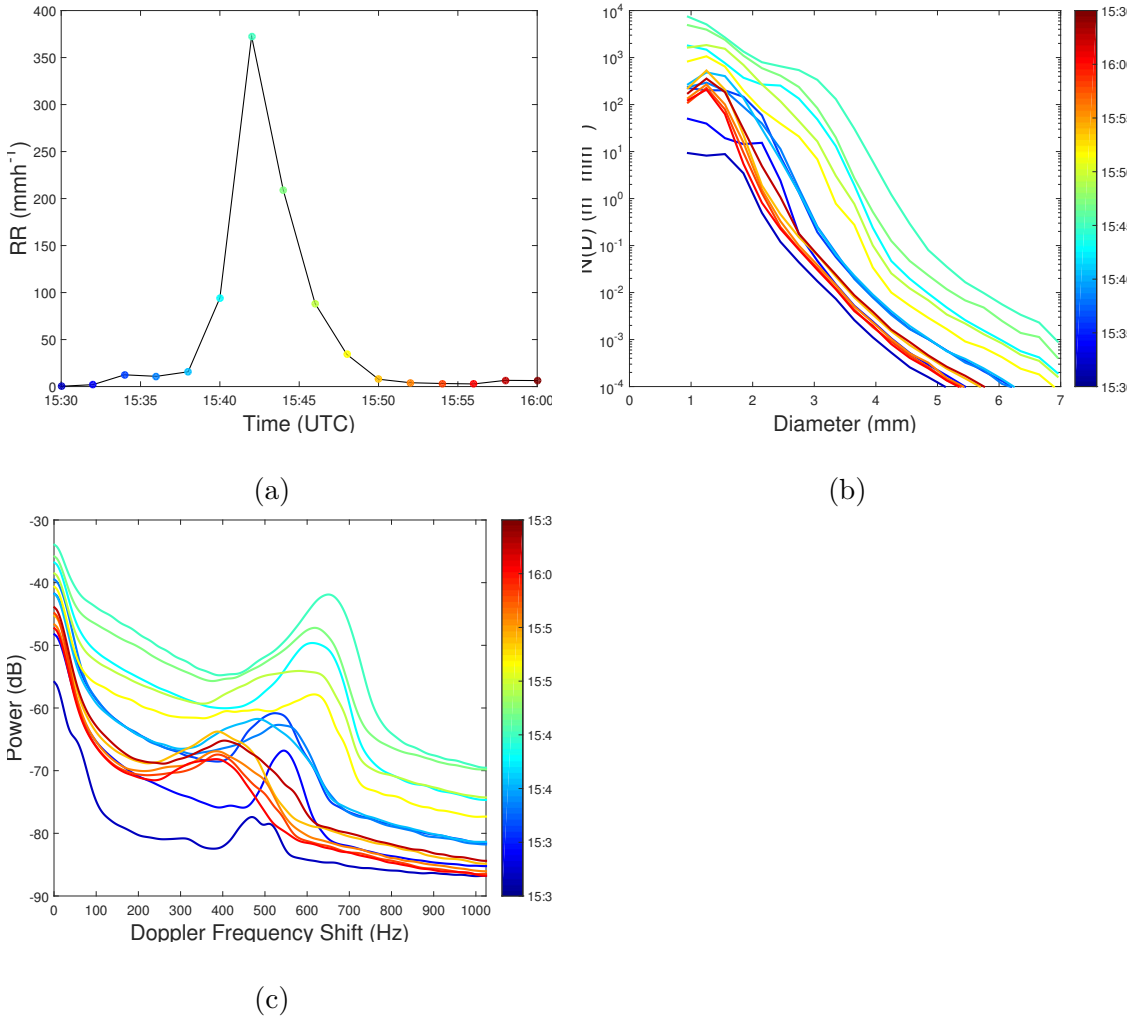

Figure 3.10: Pludix DSDs for 10 selected break-up minutes by DS algorithm in the (a) Ferrara, (b) Wasserkuppe, and (c) Linzhi experimental sites.

the presence of an updraft current in the early stage of the event and the depletion of larger drop numbers after the main shower, as is usually found in convective events. The power spectrum curves reported in 3.10c show peaks between 400 and 650 Hz, indicating great variability of the DSD throughout the event. For this extreme episode, there is a sharp decrease in the power after the peak and the frequencies affected by

the marked decrease are similar to each other at different rain rates. This indicates that the maximum break-up size has similar values, even if the number of drops and the rain rate greatly differ.

A significant number of large drops (around 5 mm, exceeding the limit estimated by Porcú et al., 2013) is found for the highest rainrate minutes, as also reported by Niu et al. (2010) for DSD measurements carried on at 1753 m a.s.l. A plausible explanation for such behavior can be attempted along the following lines. First, break-up occurs during the high rain rate minutes, but given the high drop concentration, the products of the break-up may re-combine to form large, highly unstable drops that can break-up again very easily. A second possible explanation could be the presence in the large drops of an ice core that makes the drop more stable and able to reach larger sizes. The presence of super-terminal drops (Montero-Martinez et al., 2009) could also affect the results. Additionally, during such intense rain showers, many complex interactions may take place among drops and other hydrometeors that cannot be resolved with the present study, given also the rarity of such extreme events.

31 August 2010

The event was characterized by long lasting stratified precipitation with moderate embedded convection, and rain rate ranging from 1 to 16 mm h^{-1}, as shown in figure 3.11a. The single peak of the DSD is around 1.1 mm and the DSDs corresponding to low rain rate minutes have very similar shapes according to the exponential trend. For the more intense rain rate, about 16 mm h^{-1} (dark yellow symbols in figure 3.11a around 17:30 UTC), the DSD changes concavity because of the increase in drops of all sizes, but especially around 3 mm, as reported in figure 3.11b. Looking at the Pludix power spectra (figure 3.11c), the rapid decrease of the power of the yellow lines around 700 Hz indicates the likely occurrence of break-up. The transition between moderate and

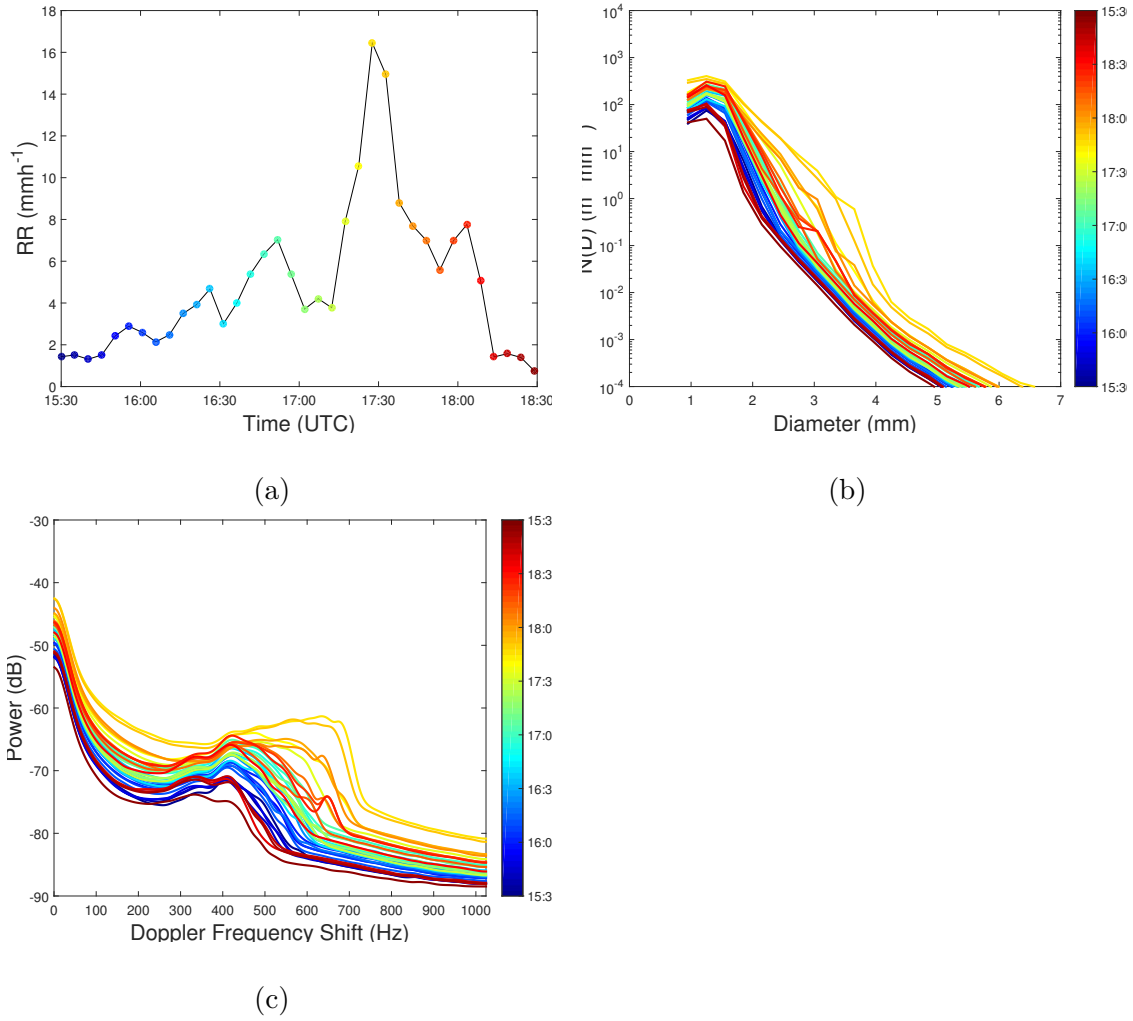

(a) (b) (c)

Figure 3.11: Pludix DSDs for 10 selected break-up minutes by DS algorithm in the (a) Ferrara, (b) Wasserkuppe, and (c) Linzhi experimental sites.

intense rain rates is marked by changes in the power spectra shapes. In the present case, however, the break-up DSD does not show the relative depletion of drops around 2 mm diameter, as reported in figures 3.10a and 3.11a: this indicates that break-up is occurring but is not yet able to increase significantly the number of very small drops. A further explanation is that this convective episode is part of a long lasting, mainly

stratified event, while the previous case is related to convective cell.

Chapter 4

Collisional Break-up and Equilibrium DSD

The extensive experimental activity related to the NASA GV-GPM program has made available an exceptional dataset, characterized by the use of more advanced instruments (2DVD and Parsivel2), the meticulous quality control, the high number of instruments used and the total number of recorded rain minute (more than 12,000 minutes), as summarized in Chapter 2. Such a large dataset made it possible a detailed study of the break-up occurrence in natural rain, and of the evolution of the DSD towards the equilibrium DSD. To this purpose, the DS algorithm has been reshaped and improved in a new automatic break-up detection algorithm (called SLOPE algorithm) set up for the 2DVD characteristics. It has to be specified that, also according to the results obtained by Pludix power spectrum and DSD analysis (3), the break-up is a fundamental mechanism to reach the equilibrium DSD. So, here we refer to break-up and equilibrium DSD in an equivalent manner.

In this chapter the SLOPE algorithm will be described and its application on the GV-

GPM analyzed, evaluating the relative occurrence of equilibrium DSD in natural rain. Moreover, the ability of the gamma distribution to fit the equilibrium DSD is discussed and the properties of rain and DSD parameters as function of break-up illustrated.

4.1 SLOPE algorithm

The SLOPE algorithm is designed to recognize the break-up features in the DSD. It is developed primarily for 2DVD DSD, which is sampled at uniform size bin, but is also applied to Parsivel DSD, where the raw output contains drop counts at uneven size bins. The algorithm consists of five steps as follows:

- The linear best fit of the considered DSD is calculated over a five diameter bins from smaller (starting point) to larger diameters.
- Four different starting points are considered between 1.0 and 1.6 mm with steps of 0.2 mm. This results in four linear relationships.
- The highest slope (HS) of the four linear best fits is considered as reference to label the DSD.
- The individual DSDs are sorted from the lowest (negative) to the highest (possibly positive) HS value. HS ranges from -4.56 to 1.97 m^{-3} mm^{-2}.
- A total of six classes are introduced based on HS. Most of the DSDs have slope between 0 and -2 m^{-3} mm^{-2}, and this interval is divided into four classes with 0.5 m^{-3} mm^{-2} increment (classes 2 to 5), and the remaining two classes are defined with $HS > 0$ m^{-3} mm^{-2} (class 1) and with $HS < -2$ m^{-3} mm^{-2} (class 6).

The algorithm analyzes the DSD between 1.0 and 2.6 mm diameter computing the slope of the linear best fit and ranks the DSDs accordingly. The figure 4.1 shows

three different examples of DSD with different values of HS as identified by the SLOPE algorithm. The dotted lines represent the liner fit; due to the figure deformation, the dotted lines emphasize the real value of HS reported in the legend figure. The linear fit is reliable and robust in identifying the changes in slope of DSD and avoids recognizing as break-up situations isolated spikes (as could happen applying the DS algorithm), due to the natural DSD variability at such short time scales.

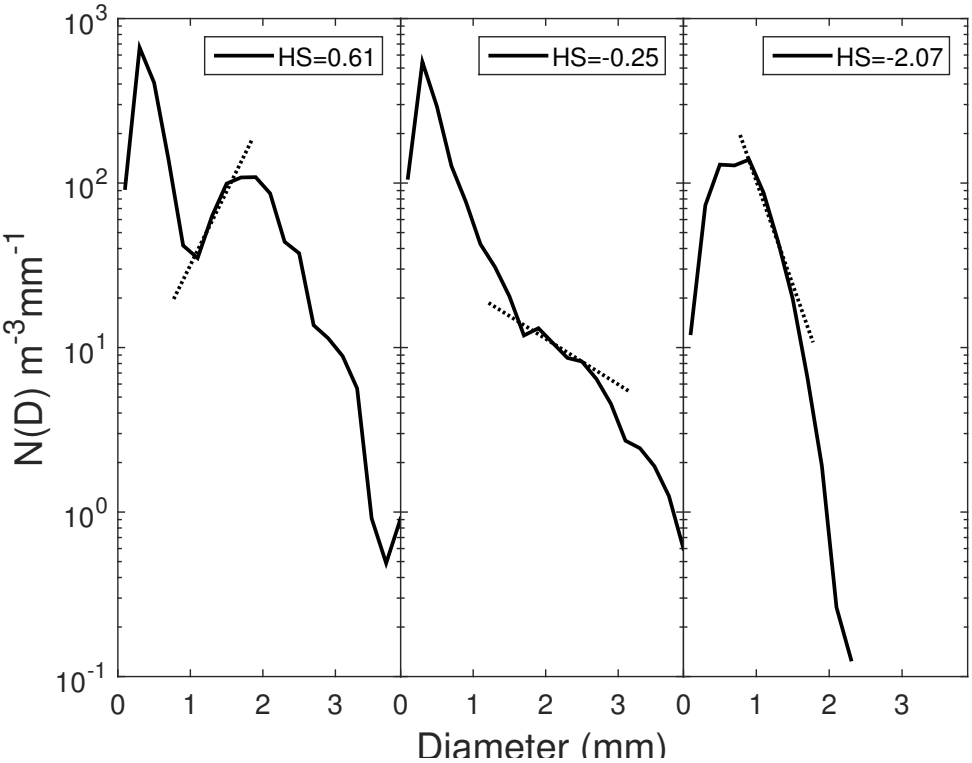

Figure 4.1: Three examples of DSD with different HS values. The dotted lines do not represent the real HS values because of the figure deformation.

The one-minute disdrometer observations are averaged over two, three and five minutes to have a more stable sampling. A sensitivity study has been conducted to evaluate the difference in using different temporal sampling and no significant discrepancy is

found in the results. For this reason, has been choose to use the two-minute average. Moreover, a minimum rainfall threshold of 5 mmh^{-1} is adopted to eliminate light rain since break-up takes place mainly in convective rain (Li et al., 2009). The 8 mmh^{-1} threshold used for both PS and DS algorithm, has been replaced by 5 mmh^{-1} threshold because, for these datasets, a sensitivity study to different rainfall threshold of 5, 6, 7 and 8 mmh^{-1} has been made. The results don't reveal particular differences by using the different RR thresholds. Consequently, the 5 mmh^{-1} threshold has been choose to have the highest number of samples.

4.1.1 SLOPE algorithm: 2DVD results

The SLOPE algorithm has been applied to the DSD data of the GV-GPM program (table 2.2). In this section will discuss the results referred to 2DVD data only. The 2DVD derived DSDs averaged on the six HS classes defined according the SLOPE algorithm for the six field campaigns are shown. The number of two-minutes averages (hereafter referred as samples) for each class is also given.

In figure 4.2 the mean DSD of each HS class for the all six field campaigns are shown. A concave down DSD shape with a single peak is observed in all six sites for classes 5 and 6. The peak occurred at diameter between 0.5 and 1.0 mm and the relatively low concentration of smaller size drops is primarily attributed to the underestimation of small drops by 2DVD (Tokay et al., 2013). For the remaining four classes, a well-defined peak occurred at 0.3 mm. For class 1, the DSD had a sharp decrease in concentration from the peak to around 1.0 mm followed by a plateau where the concentration slightly increases without changing significantly with size, until 2.0 mm. A secondary maximum was observed at around 2 mm at most of the sites followed by exponential decrease with increasing drop sizes.

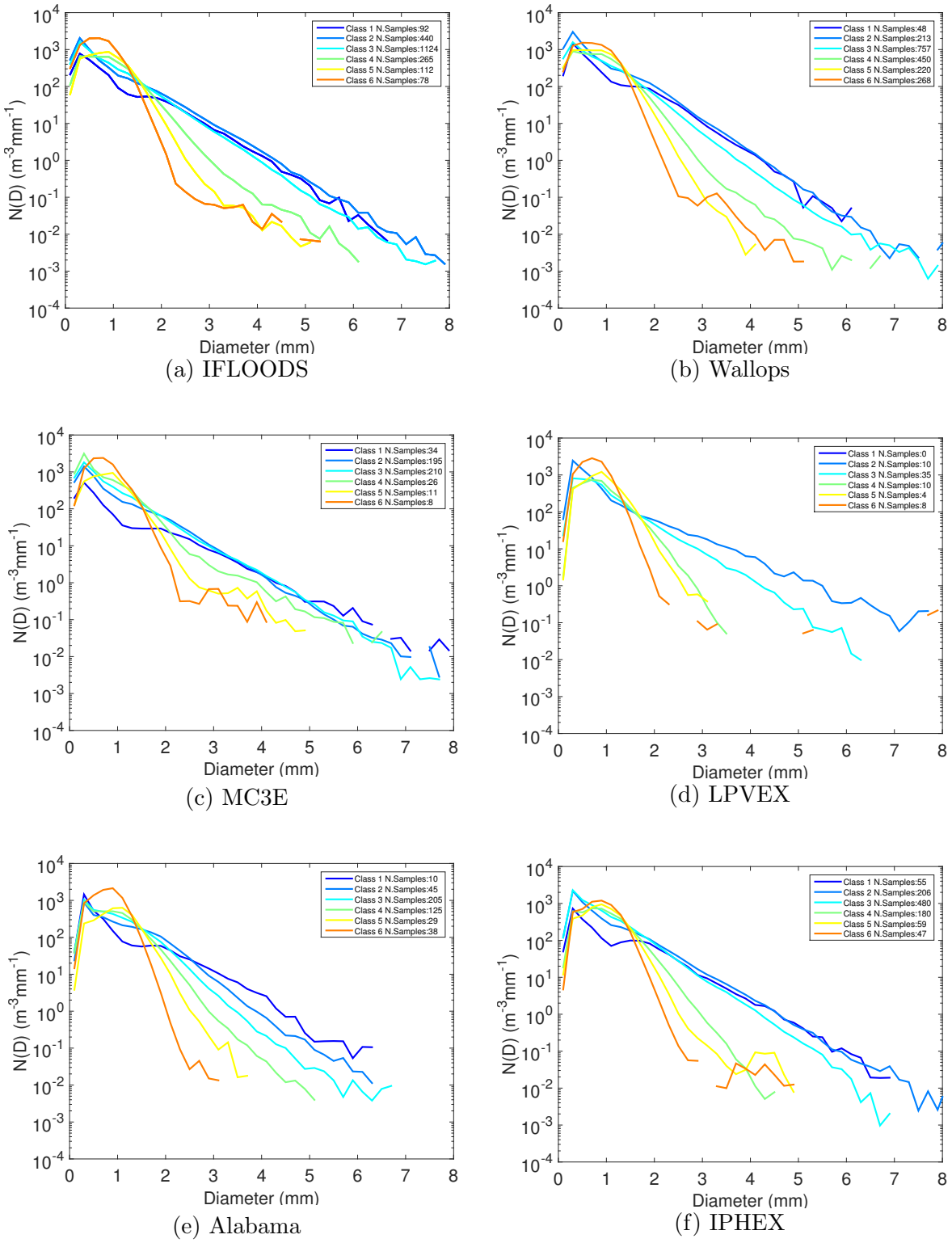

Figure 4.2: Mean DSD for each HS class for each field campaign from 2DVD data.

The DSDs with positive HS (class 1) have good agreement with those obtained by different models and defined as equilibrium DSD (McFarquhar, 2004; Pratt and Barros, 2007; Straub et al., 2010). Thus, class 1 is labeled as equilibrium DSD. However, the diameter at which the second maximum is observed is slightly lower than diameter of the maximum obtained by numerical simulation, around 2.6 mm (McFarquhar, 2004). While class 1 shows a clear signature for equilibrium DSD, class 2 marks a transition between dominant break-up, and equilibrium DSD, and DSD where the break-up is negligible with respect to other processes. Class 2 shows a sharp decrease in drop concentration from the peak to 1.0 mm followed by relatively slower decrease between 1.0 and 2.0 mm and represents situations where break-up is present but it is not able to modify the DSD up to the equilibrium. Classes 3 and 4 have the exponential slope from peak distribution to the largest observables sizes where the slope is sharper in class 4 than in class 3. When the drop concentrations fell below 10^{-1} drops m^{-3} mm^{-1}, the DSD exhibits one or more discontinuities, mostly observed for drop diameters larger than 2 mm.

The figure 4.3 shows the mean plus and minus one standard deviation (STD) for each of the six HS classes, always for IFLOODS dataset. The cloud envelop follows the trend of the mean DSD and it is evident the changing in DSD shape from class 1 (figure 4.3a) to class 6 (figure 4.3f). The width of cloud envelop decreases both from class 1 to class 6 and from lower to larger diameters. When the drop concentration is very low, about 1 $m^{-3}mm^{-1}$, the variance of distribution of number of drops corresponding to those diameter classes is too high and the cloud envelop diverges.

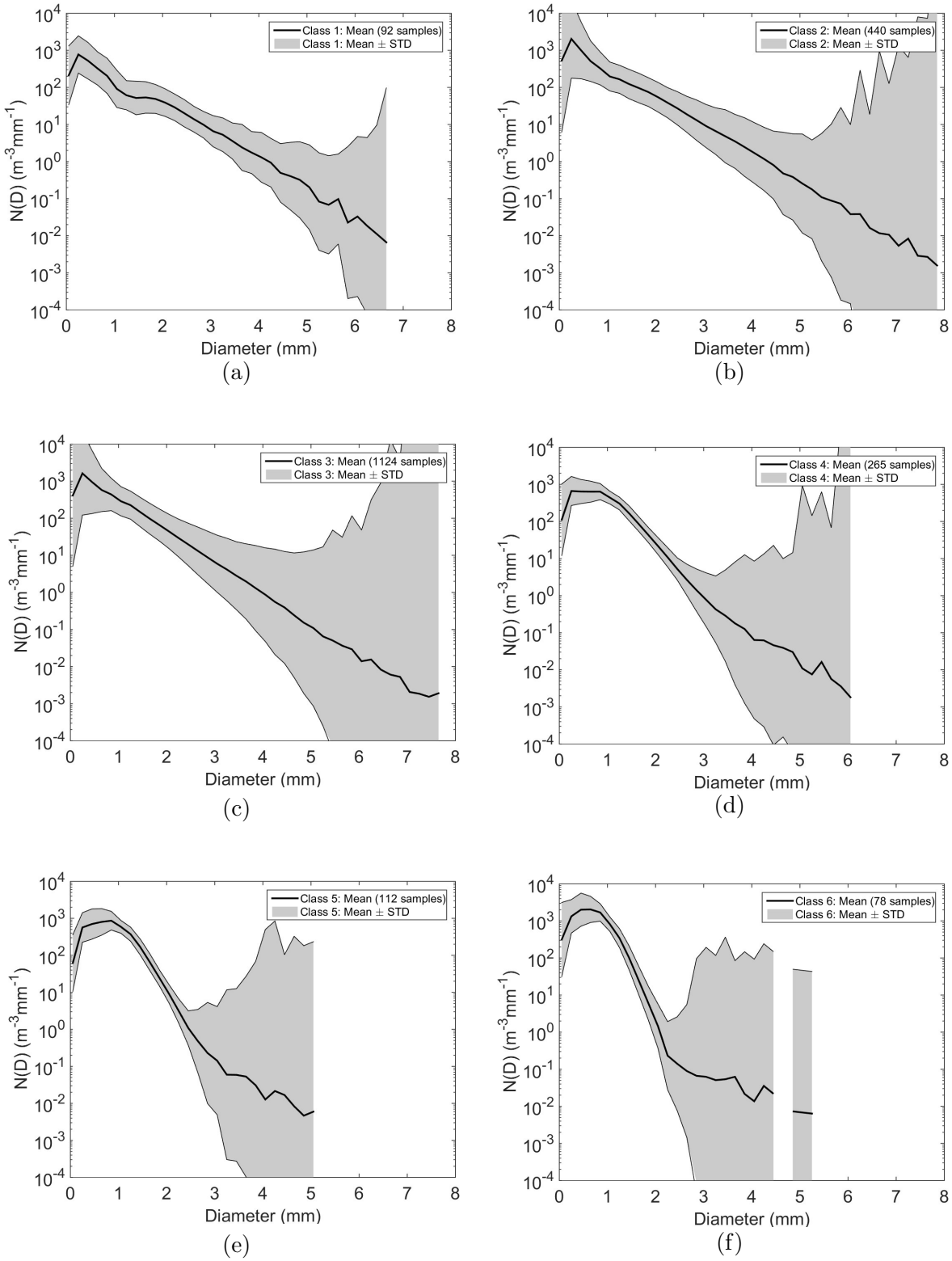

Figure 4.3: Cloud envelop of mean DSD plus and minus one standard deviation (STD) for each HS class for IFLOODS dataset. The number of samples size of each HS class is also reported.

	IFLOODS(%)	MC3E(%)	Wallops(%)	Alabama(%)	LPVEX(%)	IPHEX(%)
	2DVD	2DVD	2DVD	2DVD	2DVD	2DVD
Class 1	4.5	7.0	2.4	2.2	0	5.3
Class 2	20.8	40.3	10.9	10.0	14.9	19.5
Class 3	53.2	43.3	38.7	45.3	52.3	45.4
Class 4	12.5	5.4	23.0	27.7	14.9	17.0
Class 5	5.3	2.3	11.3	6.4	6.0	8.4
Class 6	3.7	1.7	13.7	8.4	11.9	4.4

Table 4.1: Percentage of occurrence for each HS class for each 2DVD dataset.

Table 4.1 reports the percentage of samples in each HS class for each dataset. The DSDs have positive HS values in a low percentage of cases marking the fact that equilibrium DSD is rare in natural rain. The percent values depend on the season of experiment and climatic characteristics of the regions. The maximum occurrence for class 1 was 7%, based on 2DVD observations during MC3E, which was carried on during the Spring of 2011. In contrast, class 1 2DVD observations were 2.4% at Wallops where the experiment period was mainly during Autumn 2013 and Winter 2013-14. The continental showers dominated the precipitation events during MC3E, while widespread stratiform precipitation was mainly observed at Wallops.

Combining the classes 1 and 2, the percentage reaches up to about 47% during MC3E. This remarks that break-up is more frequent during convective episodes, but only in few cases (the 7% in class 1) is able to modify the DSD to reach the equilibrium DSD. High percentage values were also observed both for classes 1 and 2 during IPHEX and IFLOODS where the experiments focused on springtime flooding over orographic and flat areas, respectively.

A further significant result is obtained from LPVEX that had the lowest occurrences for class 1 (0%) and 2 (14.9%). This experiment was designed for observations of light rain

(in fact the minutes with $RR > 5$ mmh^{-1} are very few) that frequently occurs during Autumn at high latitudes and this is an additional proof that break-up takes place and has effect on the DSD shape mostly during convective rain. The total absence of equilibrium DSD confirms that this feature needs particular conditions to happen. In Alabama, the percentages were relatively low for classes 1 and 2. Although the most of the observations was during Spring and early Summer, just few convective rainfall was included. The rain rate and reflectivity recorded were below 10 mmh^{-1} and 36 dBZ in most cases.

4.1.2 SLOPE algorithm: Parsivel results

The SLOPE algorithm described above is designed for disdrometer observations where the bin width is uniform. The performance of the detection algorithm was tested for Parsivel observations where the bin width is not uniform and doubles from 0.129 mm to 0.257 mm at around 1.3 mm. This particular diameter is within the range of size bins used by the algorithm to compute the HS value.

Figure 4.4 reports the mean DSD for each HS class obtained from Parsivel data for IFLOODS, IPHEX and Wallops. As just mentioned in the chapter 2 in the other three site the Parsivel data available were collected with the older version of the instrument and for this reason it was not considered, given the unsatisfactory performance of the old version instrument).

The results are in a good agreement with the findings based on 2DVD: class 1 shows the DSD equilibrium, particularly during IFLOODS and IPHEX, and class 2 can be considered as the transition from break-up to non break-up. The other four classes show an exponential trend of DSD with a different slope as function of class. The similar features of DSD in each class between 2DVD and Parsivel reveals that the SLOPE

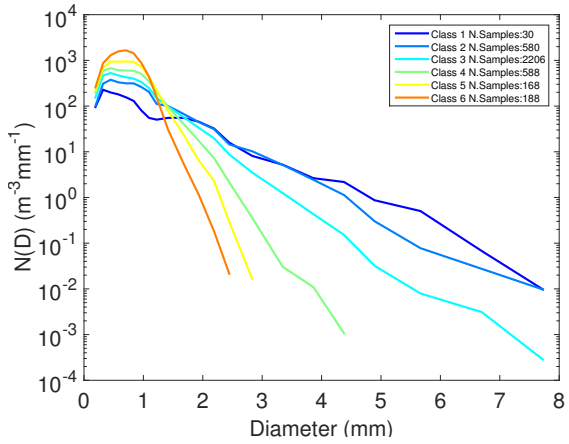

(a) IFLOODS

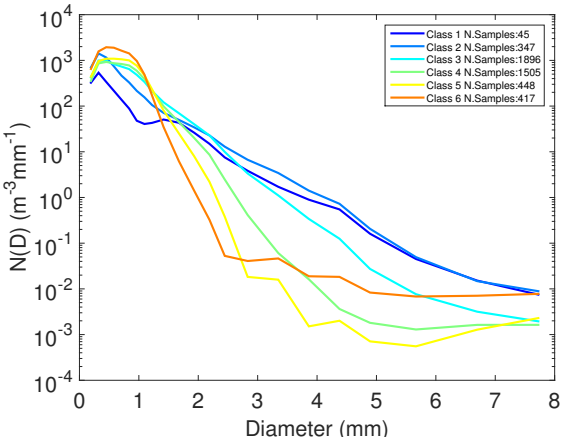

(b) IPHEX

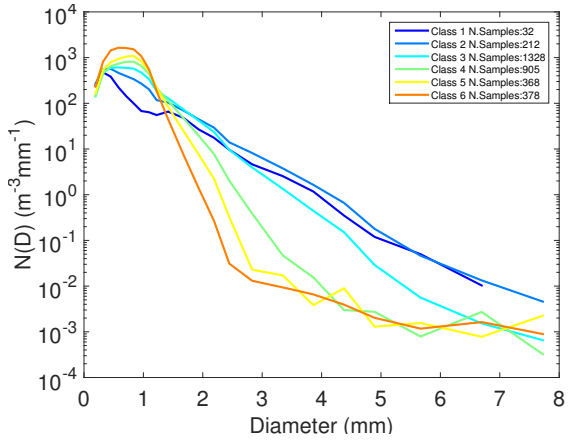

(c) Wallops

Figure 4.4: Mean DSD for each HS class for each field campaign from Parsivel data.

algorithm is not limited to a disdrometer where the size bins is uniform. However, percent occurrence for classes 1 and 2 was much less in Parsivel (table 4.2) than in 2DVD (table 4.1). The table 4.2 reports the percentage of occurrence for each HS class for the three datasets where the Parsivel were installed. The difference is more marked in the class 1 than class 2, while the percentage is more similar for classes from

three to six. This is mainly due to the larger width of DSD bins, and indicates that this instrument characteristic does not allow recognizing a large part of break-up cases.

	IFLOODS(%)	Wallops(%)	IPHEX(%)
	Parsivel	Parsivel	Parsivel
Class 1	0.8	1.0	1.0
Class 2	15.4	6.6	7.5
Class 3	58.7	41.2	40.7
Class 4	15.6	28.1	32.3
Class 5	4.5	11.4	9.6
Class 6	5.0	11.7	8.9

Table 4.2: Percentage of occurrence for each HS class for each Parsivel dataset.

4.2 Evaluation of gamma fit

The three parameters gamma distribution (Ulbrich, 1983) is widely used to parameterize the DSD. The parametric form of gamma distribution is described by the equation 1.7 and the three parameters N_0, μ and Λ can be estimated applying the method of moments (section 1.4).

A visual comparison between figures 4.2 - 4.4 and figure 1.11 reveals that gamma distribution is not the best model for the DSD of class 1 and 2. In this section is evaluated the goodness of gamma distribution in fitting the measured DSDs as function of HS classes. An alternative parameterization for a better fit of the break-up induced DSDs requires more in-depth analysis and will be object of future studies. For this purpose both the method of moments M234 and M346 are used to estimate the gamma parameters and the analysis is made only for the 2DVD data. The estimation

of gamma distribution parameters (μ, λ and N_0) with M234 is showed by equations 1.8 ÷ 1.10. Similarly are obtained the parameters with M346. Since the results applying the method M234 and M346 are very similar to each other, here will be shown only the results obtained with M234 for IFLOODS dataset (the biggest one).

For this purpose, for each DSD selected by the SLOPE algorithm the corresponding gamma distribution is estimated. The Pearson correlation coefficient is calculated between the experimental two-minutes averaged DSD and the gamma distribution to determine the applicability of the gamma fit at six different HS classes. The correlation as well as for the whole DSD spectrum, is also calculated for the size interval 1.0-2.6 mm, where the algorithm analyzes the slope of the DSD to assess the effects of the break-up process on the DSD shape.

The Pearson correlation coefficient is defined as follows:

$$R = \frac{\sigma_{xy}}{\sigma_x \sigma_y} \tag{4.1}$$

where R is the correlation coefficient, σ_{xy} is the covariance while σ_x and σ_y are the standard deviation of variable x and y. For the present analysis, the variables x and y are the measured DSD and the corresponding estimated gamma distribution respectively.

Figure 4.5 shows the correlation coefficient between the experimental DSDs and the estimated gamma distributions for IFLOODS 2DVD dataset. The colors are in according with the colors defined in figures 4.2 - 4.4 for each class. Considering the entire size spectrum, majority of observations have correlations above 0.8 for classes 3-6, while the correlations have a relatively wider range for classes 1-2 (figure 4.5a) showing lower values with higher frequency. For the selected size interval 1.0-2.6 mm, the correlations remained above 0.9 for classes 3-6, while class 1 exhibited evenly distributed correlations between near 0 and 1 (figure 4.5b). This shows that gamma distribution often

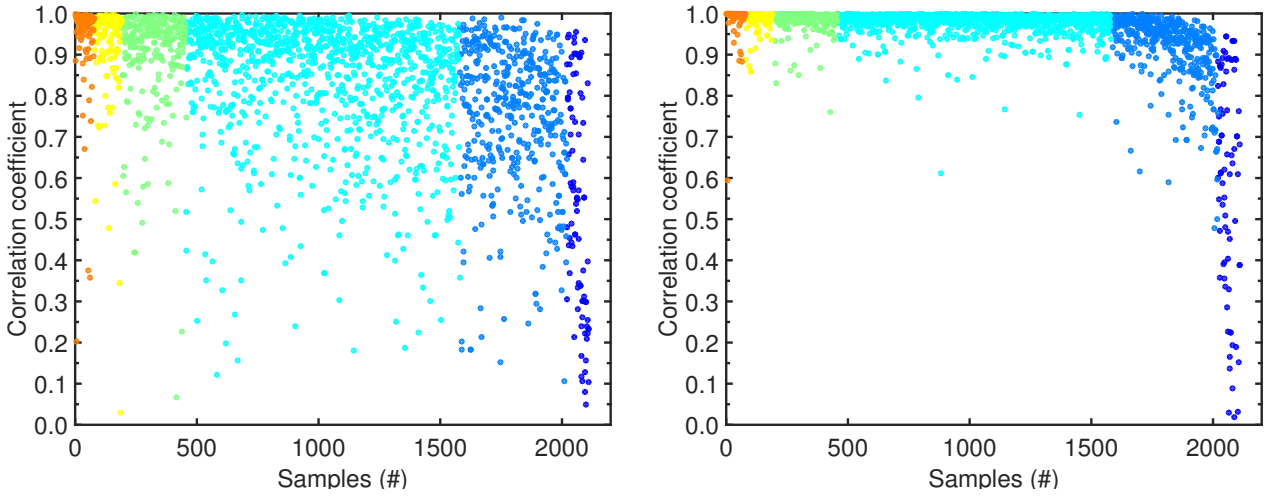

(a) (b)

Figure 4.5: Pearson correlation coefficient between the experimental DSD and the corresponding estimated gamma distribution for a) the whole DSD spectrum and b) for the 1.0-2.6 mm diameter range, for IFLOODS dataset. The samples are ordinated from the lowest to the highest HS value.

fails in approximating equilibrium DSDs. Class 2, which is the transition from equilibrium DSD to situations where the break-up process does not affect the DSD shape, has both high correlations above 0.9 and between 0.6-0.9. This confirm that the gamma distribution is not the best approximation also for the transition minutes, where the break-up is present but the equilibrium DSD is not reached. It should be added that the low correlation could be partially due to the differences between observed and fitted spectra in small and large drop ends. Since M234 is used, the fitting in both ends of the size spectrum may substantially deviate from the observations. Considering the whole spectrum, if the observed spectrum has large number of small drops and/or presence of large drops, the correlations are expected to be relatively low.

Also using the truncated gamma distribution instead untruncated gamma distribution,

the trend of the correlation coefficient does not change.

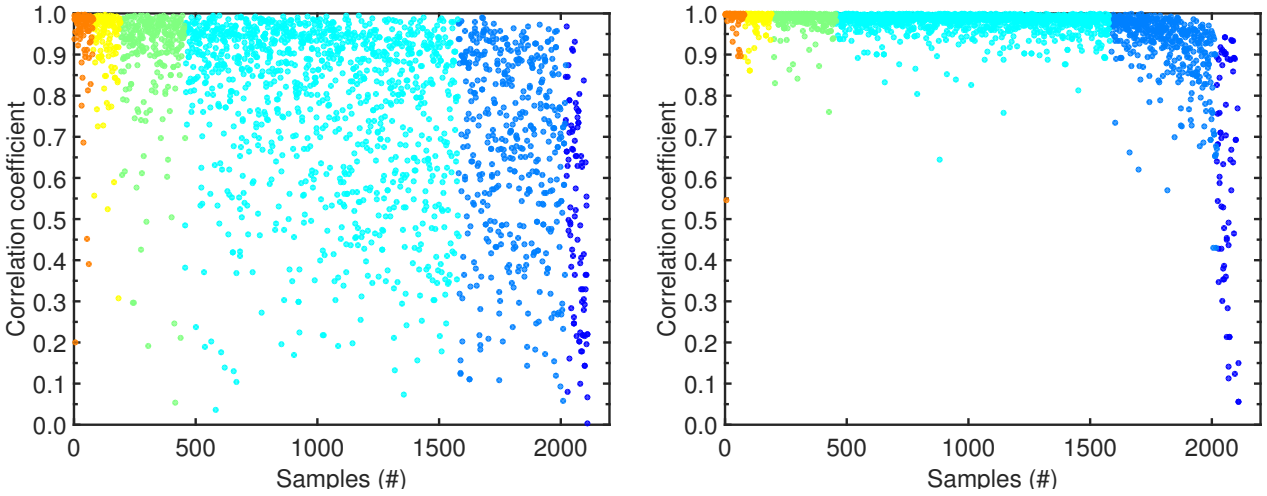

(a) (b)

Figure 4.6: Pearson correlation coefficient between the experimental DSD and the corresponding estimated gamma truncated distribution for a) the whole DSD spectrum and b) for the 1.0-2.6 mm diameter range, for IFLOODS dataset. The samples are ordinated from the lowest to the highest HS value.

The differences between figures 4.5 and 4.6 are negligible and the observations made for the figure 4.5 are valid for the figure 4.6 too.

4.3 Integral rain and DSD parameters

The parametric form of size distribution is often derived from disdrometer observations without visually inspecting the DSD. In that regard, it is important to identify the break-up based DSD parameters if they are different than non break-up DSD parameters. This can be considered an additional indicator to distinguish between cases where the equilibrium DSD can develop and cases where it is not possible. For this purpose, the trend of several rain and size distribution parameters are studied as function of the

HS classes. The table 4.3 reports the parameters used for this analysis.

Parameter	Symbol	Units	Definition
Mean mass diameter	D_{mass}	mm	$D_{\text{mass}} = \frac{M_4}{M_3}$
Maximum diameter	D_{max}	mm	/
X Factor	X	/	$X = \frac{D_{\text{max}}}{D_{\text{mass}}}$
Total concentration of drops	N_T	m^{-3}	$N_T = \sum_{i=1}^{n} N_i(D)$
Normalized intercept parameter with respect to N_T	N_T^*	$m^{-3}mm^{-1}$	$N_T^* = \frac{N_T}{D_{\text{mass}}}$
Normalized intercept parameter with respect to LWC	N_W	$m^{-3}mm^{-1}$	$N_W = \frac{256 \cdot LWC}{\pi \rho_w D_{\text{mass}}}$
Rain Rate	RR	mmh^{-1}	$RR = \frac{\pi}{6} 3.6 \cdot 10^6 \int_{D_{min}}^{D_{max}} v(D) D^3 N(D) dD$
Reflectivity	Z	dB	$Z = \int_{D_{min}}^{D_{max}} D^6 N(D) dD$
Liquid Water Content	LWC	$g\ m^{-3}$	$LWC = \frac{\pi}{6} \rho_w \int_{D_{min}}^{D_{max}} D^3 N(D) dD$
Horizontal Reflectivity	Z_H	dB	$Z_H = \int_{D_{min}}^{D_{max}} S_H D^6 N(D) dD$
Differential Reflectivity	Z_{dr}	dB	$Z_{dr} = 10 log \frac{Z_H}{Z_V}$
Difference between the horizontal and vertical phase shift	K_{dp}	$deg\ km^{-1}$	$K_{dp} = \frac{180}{\lambda} W(1 - \overline{r_m})$

Table 4.3: Integral rain and DSD parameters.

The trend of selected parameters will be shown in the figure 4.7 for 2DVD IFLOODS dataset.

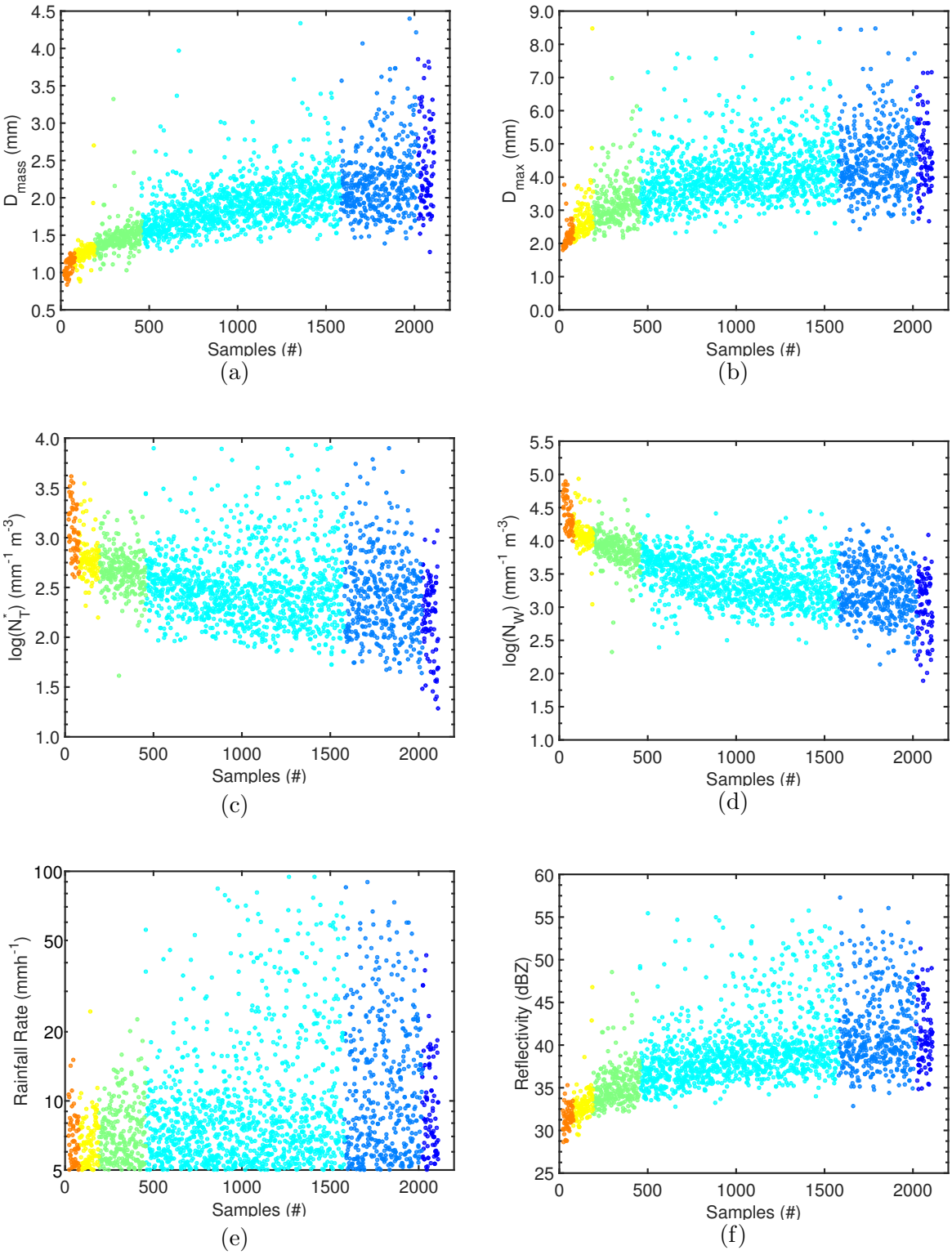

Figure 4.7: Distribution of the selected DSD parameters as function of the samples number, ranked from the lowest to the highest HS value. a) D_{mass}, b) D_{max}, c) $\log(N_T{}^*)$, d) $\log(N_W)$, e) RR and f) Z.

The analysis has been carried out also for the other 2DVD datasets but since the findings are very similar will not be shown. The distribution of D_{mass}, D_{max} and $N_T{}^*$ and N_W has different characteristics at different classes (figures 4.7a- 4.7d). D_{mass} and D_{max} decreased from class 1 to class 6, while the reverse was true for logarithmic values of $N_T{}^*$ and N_W. The low values of D_{max} and D_{mass} indicate narrow DSD, while high values of $N_T{}^*$ and N_W reveal large concentration of small and midsize drops for classes 5 and 6. This is in agreement with the mean DSD in figures 4.2 and 4.4. The increase in D_{max} and D_{mass} is more gradual from class 3 to class 1 coinciding with relatively small changes in the width of the size distribution in figures 4.2 and 4.4. The decrease in $N_T{}^*$ and N_W is also gradual from class 3 to class 1. The trend is confirmed also by the mean and standard deviation of these parameters that both decrease from class 1 to 6 for D_{mass} and D_{max} while increase for $N_T{}^*$ and N_W.

Rain rate, which is the moment 3.67 of the DSD, does not show any trend from class 1 to class 6 (figure 4.7e) unlike the other parameters. Reflectivity, which is the sixth moment of DSD decreased from class 1 to class 6 (figure 4.7f). Classes 2 and 3 have larger sample sizes and show wide variations in both rain rate and reflectivity with the highest values of both mean and standard deviation. Class 1 has relatively smaller sample size and was bounded between 5 and 30 mmh^{-1} for rain rate and between 36 and 51 dBZ for reflectivity. Overall, none of the computed DSD parameters, if considered alone, can be used to identify equilibrium or break-up dominated DSD with respect to DSD where break-up is negligible, but they can be additional indicators to screen out situations where collisional break-up does not affect the DSD shape (i.e. no modification of the DSD when the reflectivity is lower than 36 dBZ). Consequently, even if a threshold could be set for each parameter, this is not a sufficient condition to detect equilibrium (or dominated break-up minutes) but the SLOPE algorithm has to be applied for this aim.

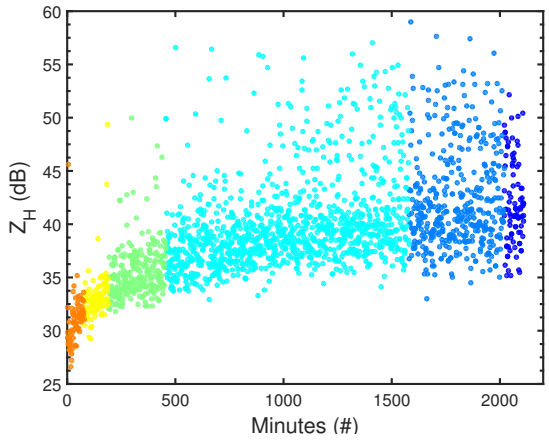

(a)

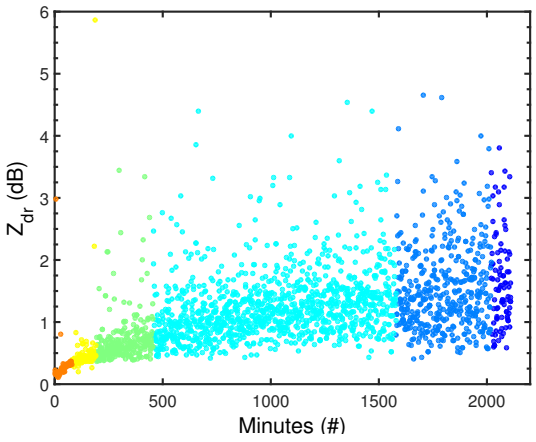

(b)

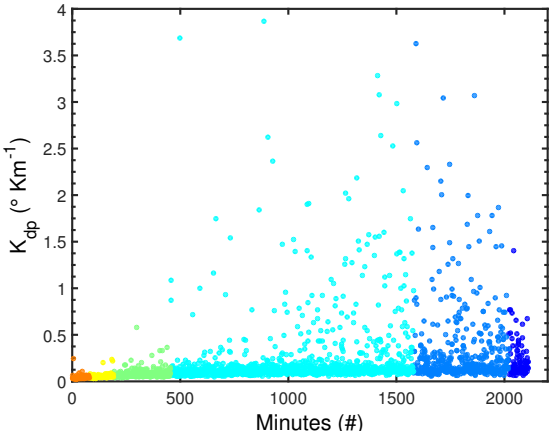

(c)

Figure 4.8: Distribution of the selected DSD parameters for radar application. a) Z_H, b) Z_{dr}, c) K_{dp}.

Very similar findings are obtained by the radar DSD parameters. The trend of Z_H parameter (figure 4.8a) shows no difference with respect to the Z trend (figure 4.7f), while no more informations can be obtained by Z_{dr} and K_{dp} analysis. Z_{dr} (figure 4.8b)

presents very similar values for all classes and also the standard deviation for classes 1-3 are comparable to each other. Lower mean and standard deviation values are obtained for classes 5-6. K_{dp} (figure 4.8c) does not show any particular trend and does not give an additional contribute to the analysis.

Chapter 5

Small scale DSD spatial variability

Insight into the spatial variability of the DSD, and hence rainfall, is of primary importance for various environmental applications like cloud/precipitation microphysical studies, numerical weather modeling, rainfall estimation using remote sensing data, hydrological applications, etc.. Moreover, extreme spatial variability of rainfall is a source of uncertainty in evaluation of remote sensing rainfall estimates across the pixel/footprint. The spatial variability of the DSD can be investigated using multiple synchronized measurements distributed in the same area. Although different works are based on rain gauges network (Ciach and Krajewski, 2006; Villarini et al., 2008; Tokay and Öztürk, 2012 and many others), the difficulties in managing a disdrometer network leads to a lack in the literature about the DSD spatial variability using disdrometer data.

Very few papers are focused on the study of DSD spatial variability, but each one presents some limitation either because the field measurement was not set up primarily for this analysis type (Lee et al., 2009) or because the analysis regarded a limited number of DSD parameters (Miriovsky et al., 2004; Jaffrain et at., 2012) or because

the number of disdrometers available is limited.

In this context, the study carried out in this Thesis is the first result of systematic study of DSD spatial variability using two disdrometer networks (Wallops and MC3E) set up for this aim. The availability of twelve disdrometers (six 2DVD and six Parsivel) at Wallops as well as the seven 2DVD installed at MC3E campaign resulted in two unprecedented disdrometric dataset. In particular, the distance among the instruments is comparable with a radar pixel or satellite footprint and covers different range of small spatial scale.

In this chapter will be shown the method used to analyze the small scale spatial variability of DSD parameters and the results obtained for the two field campaigns analyzed.

5.1 Methodology

To study the small scale DSD spatial variability, the three-parameter exponential model has been selected (eq. 1.21) as presented in section 1.6, $R(d) = R_0 e^{\left(-\frac{d}{d_0}\right)^{s_0}}$ where d is the distance between two instruments , $R(d)$ is the correlation as function of distance, R_0 is called "nugget parameter" and represents the correlation between two collocated instruments (with non zero distance but much lower then scale distance), d_0 is the correlation distance or scale parameter and s_0 is the shape parameter.

The nugget R_0 gives us information about the very small scale variability of the process as well as the measurement errors (Journel and Huijbregts, 1978). It is ideally close to one as two collocated instruments of the same type should agree to one another with almost no variability between them and almost no measurement errors. For short integration periods, the sampling errors play an important role resulting noticeable variability between the collocated gauges. While 5-minute integration is considered the

shortest reliable period for gauge rainfall, disdrometer derived rain parameters are often presented at 1-minute integration. In that regard, the natural variability and sampling differences result in noticeable variability in the derived parameters. Due to the unavailability of two collocated disdrometers of the same type, for this work the nugget parameter was assigned following previous studies based on rain gauge measurements (Villarini et al., 2008; Tokay and Öztürk, 2012). The correlation distance d_0 gives us information about the distance at which the process decorrelates. Finally, for the shape factor s_0, controls the behavior of the correlation function at the small scale (near zero distance). The shape parameter is relatively more dependent to the correlation distance and the root-mean square error between the observed and fitted correlations is the measure of the goodness of the fit. If the shape and nugget parameters are one, then equation 1.21 is the simple exponential model where d_0 is the e-folding distance (Ciach and Krajewski, 2006). Even when the shape parameter is not one, d_0 is still the e-folding distance when d is equal to d_0.

To estimate the correlation distance and the shape parameter from the equation 1.21, the following methodology has been used:

- Following previous studies (Villarini et al., 2008; Tokay and Öztürk, 2012), the nugget parameter R_0 are assigned three different values (0.90, 0.95 and 0.99).

- The correlation coefficient $\mathrm{R(d)_{obs}}$ is calculated between paired measurements. Since six and seven sites were operated at Wallops and MC3E respectively, a table of 15 and 21 correlations ($\mathrm{R(d)_{obs}}$) at corresponding distances was constructed.

- Theoretical $\mathrm{R(d)_{est}}$ is estimated for multiple couple of d_0 and s_0. For an initial guess, a range of s_0 is set from 0 to 2 at 0.01 interval and d_0 is from 0 to 300 km at 0.1 km interval.

- The unknown parameters of d_0 and s_0 are determined minimizing the root-mean square error (RMSE) between the $R(d)_{obs}$ and $R(d)_{est}$.

Fifteen different DSD parameters were analyzed for the small scale spatial variability. The parameters included the twelve described in table 4.3 more the shape parameters $\mu(N_T^*)$ and $\mu(N_W)$ of DSD gamma parameterization corresponding to the normalization done with respect to total concentration (N_T) and with respect to liquid water content (LWC), and also the shape parameter with respect to $\sigma(D_{mass})$. The $\log(N_T{}^*)$ and $\log(N_W)$ are also analyzed.

5.2 Results: Wallops dataset

5.2.1 Dataset description

The data analyzed were collected in the Wallops Flight Facility in the period indicated in table 2.2. The distances among the disdrometers in the measuring field ranges from 0.5 to 2.3 km. This characteristic, together with the fact that in each measuring point a 2DVD and a Parsivel were collocated, makes the dataset unique for the study of DSD spatial variability. In fact, a measuring field (figure 5.1) comparable in size to a satellite footprint or radar pixel,equipped with twelve disdrometers, is not present in literature. It has to be specified that the footprint of TRMM-PR (Tropical Rainfall Measuring Mission - Precipitation Radar) and GPM-DPR is approximately 5 km, a bit larger than the Wallops measuring field.

The dataset size used for this study is different from the one described in table 2.2 because different criterion and threshold were used to select the data. Five different rain/no-rain thresholds are used based on K_u- and K_a-band reflectivity and rain rate. The choice of K_u- and K_a-band reflectivity threshold is related to the applicability of

this study to the PR and DPR retrieval algorithm, on board the TRMM and GPM mission, respectively. The preliminary observation of DPR indicates the minimum detectable signal ranges between 12 dB and 15 dB for K_u-band and 12 dB for K_a-band radars while the TRMM-PR minimum detectable signal at K_u-band is 18 dB.
Basing on these considerations, the dataset size according the different thresholds when all twelve instruments (the six 2DVD and the six Parsivel) exceed the considered threshold, results in:

- RR$>$ 0.1 mmh^{-1} (447 minutes);
- $Z_{K_a}>$ 12 dB (445 minutes);
- $Z_{K_u}>$ 12 dB (434 minutes);
- $Z_{K_u}>$ 15 dB (380 minutes);
- $Z_{K_u}>$ 18 dB (278 minutes);

Throughout the experiment, the maximum RR was 13.1 and 18.4 mmh^{-1} for 2DVD and Parsivel, respectively, while the mean RR was around 1.1 mmh^{-1} (exactly 1.09 and 1.15 mmh^{-1} respectively) for both instruments for rain/no-rain threshold of 0.1 mmh^{-1}. The minimum detectable RR was 0.11 and 0.08 mmh^{-1} for $Z_{K_a}>$12 dB for 2DVD and Parsivel, respectively, while 0.16 and 0.30 mmh^{-1} for $Z_{K_u}>$18 dB. These reflectivity limits corresponds to DPR and PR minimum detectable signals and resulted in missing 0.44% and 38% in rain occurrence and $\sim$0% and 19% in rainfall, respectively if 2DVD data are considered. More restrained is the missing of rain occurrence considering 12- and 15 db-Z_{K_u} threshold with respect to 18 db-Z_{K_u} threshold, resulting in 3% and 15% respectively for 2DVD data.
To verify the consistency of collected data at the different thresholds, the Probability

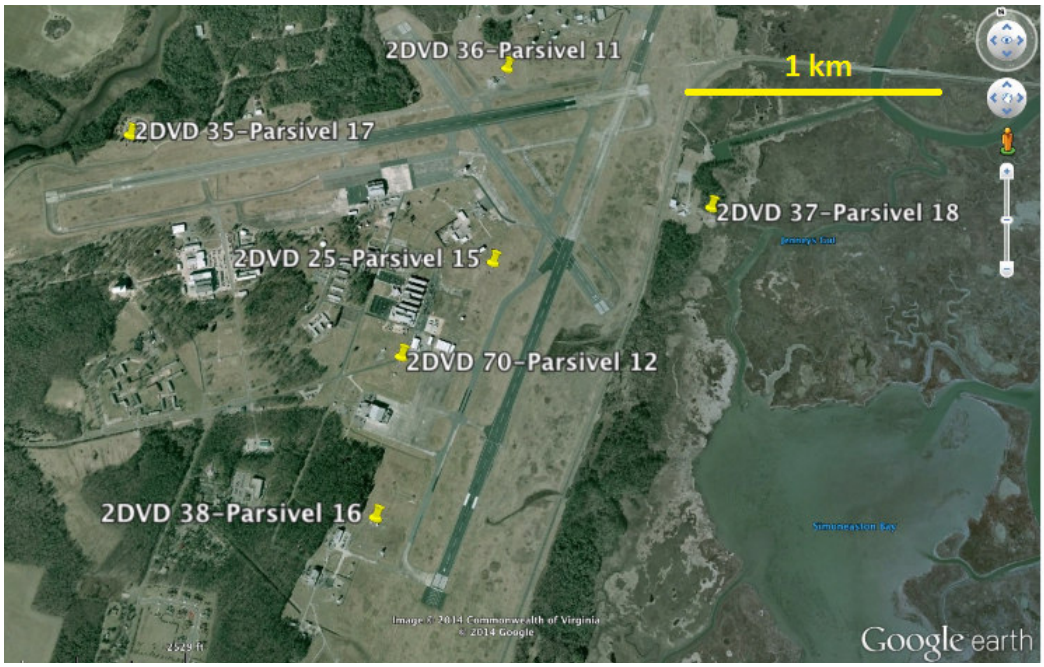

Figure 5.1: Measuring field at NASA Wallops Flight Facility.

Density Function (PDF) and Cumulative Density Function (CDF) are calculated for each parameter both for 2DVD and Parsivel. PDF and CDF of DSD and rain parameters provide an insight on the agreement between the 2DVD and Parsivel disdrometers. Here, will be shown the PDF and CDF for RR, 12 dB-Z_{K_a} and 18 dB-Z_{K_u} threshold. The two instruments show good agreement for the most of analyzed parameters. The figure 5.2 depicts the PDF and CDF of RR, Z_{K_a} and Z_{K_u} for three different rain/no-rain thresholds for 2DVD and Parsivel disdrometers. The probability distribution of these parameters, as well as Z, Z_H, LWC (not shown here) show negligible difference, with a slightly higher percentage of lighter rainfall in 2DVD than in Parsivel (figures 5.2a-5.2b). For the K_a- and K_u-band reflectivities, the distributions have similar trends in the two disdrometers (figure 5.2c- 5.2f). At the same time, the distributions were shifted toward higher reflectivities at K_u-band than at K_a-band reflectivity and rain/no-rain

threshold for the same disdrometer. For all three parameters, the rain rate and K_a-band based threshold resulted in similar distributions while K_u-band threshold showed significantly less sensitivity to the lighter rain regardless of choice of disdrometers.

The probability distributions of the N_W (figure 5.3) has noticeable differences between Parsivel and 2DVD reflecting the differences in sensitivity to the small drops (figures 5.3a- 5.3b). In fact, N_W skews toward higher values in 2DVD than in Parsivel indicating the presence of more small drops in 2DVD than in Parsivel. The sensitivity to the rain/no-rain thresholds is insignificant for both disdrometers as cumulative distributions overlapped for all three thresholds. The same discussion applies to $N_T{}^*$ (not shown here).

D_{mass} (figure 5.3), on the other hand, has similar probability distributions between the disdrometers with a narrow distribution peaking 1.1-1.2 mm (figures 5.3c- 5.3d). A very good agreement in distributions of rain rate and D_{mass} between the disdrometers reflects the good agreement in mid-size section of the size spectra. The probability distribution of D_{max} (figure 5.3) of Parsivel presents a multi peak discontinuous trend, reflecting its bin width effect, in contrast to continuous probability distribution in 2DVD (figures 5.3e- 5.3f). In fact, the bin width of Parsivel is 0.5 mm between 2.6 and 5.3 mm where a large part of the D_{max} is observed and 1 mm for larger D_{max} values. At the same time, cumulative distributions have a good agreement indicating both disdrometers were able to sample D_{max} adequately even though 2DVD has the twice the sampling area of Parsivel.

Analyzing the differences among the thresholds used, the PDF and CDF of RR and 12 dB-Z_{K_a} threshold are very similar to each other, while 18 dB-Z_{K_u} shows a different trend. The difference is more marked for integral DSD parameters (RR, Z_{K_a}, Z_{K_u}, etc.) with a greater contribution from the upper end of distribution both for 2DVD and Parsivel (figure 5.2).

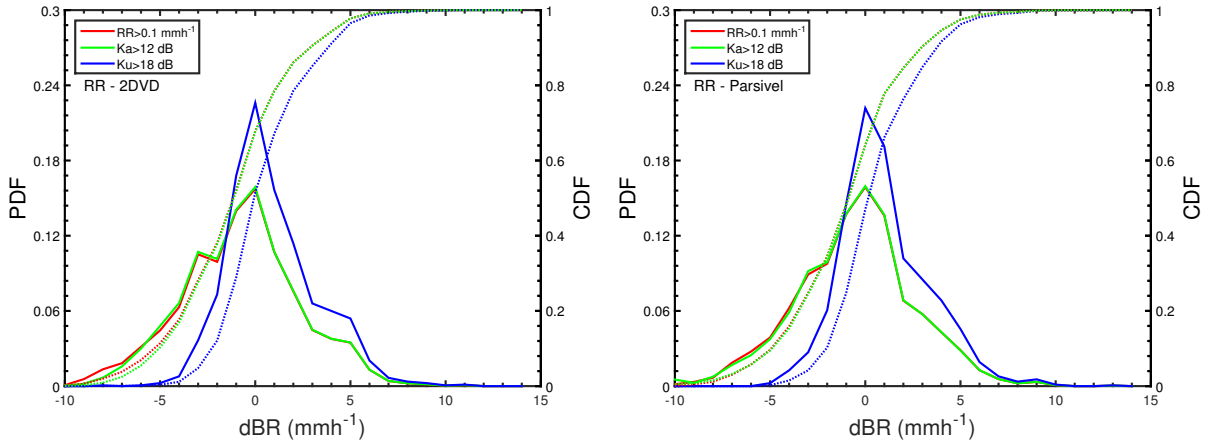

(a)

(b)

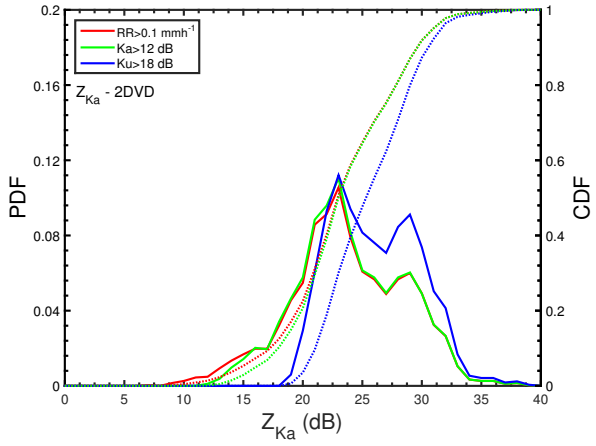

(c)

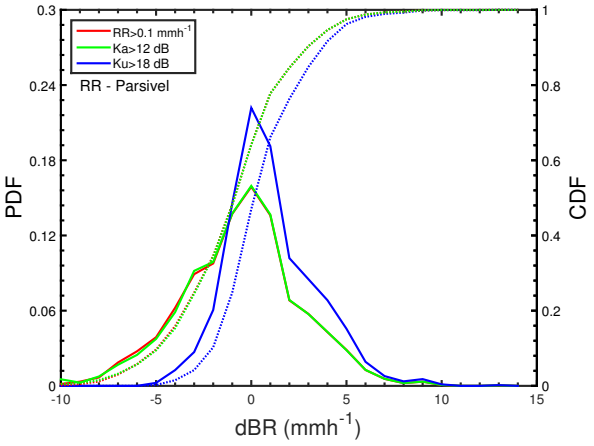

(d)

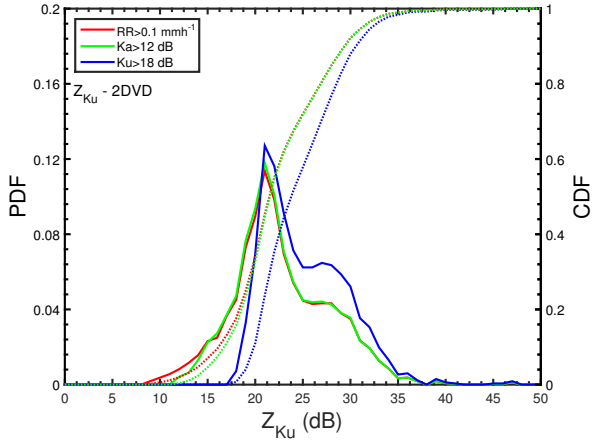

(e)

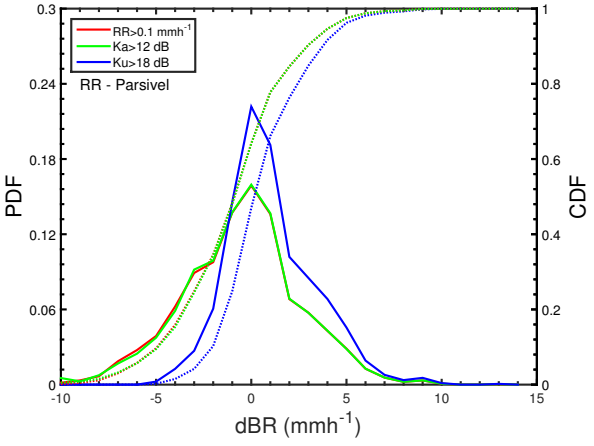

(f)

Figure 5.2: PDF and CDF of DSD integral parameters: (a) and (b) RR, (c) and (d) Z_{K_a}, (e) and (f) Z_{K_u} for 2DVD and Parsivel data, respectively.

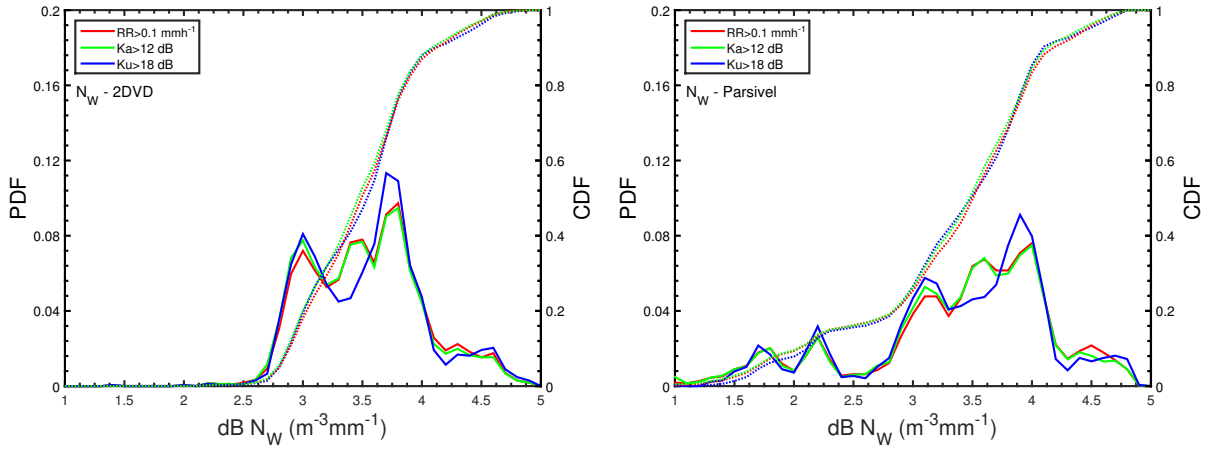

(a)

(b)

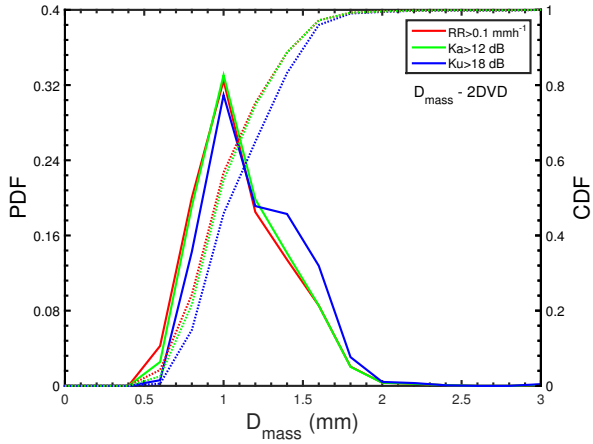

(c)

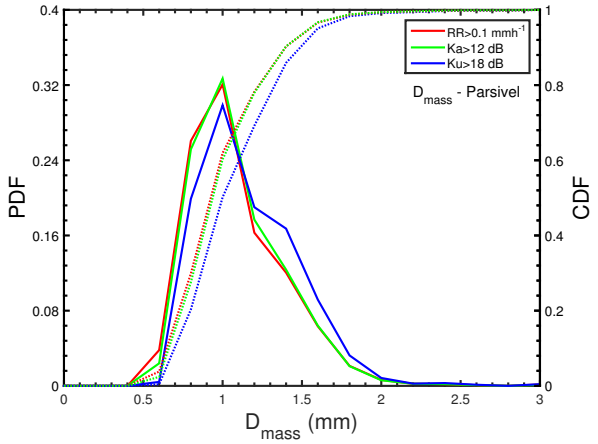

(d)

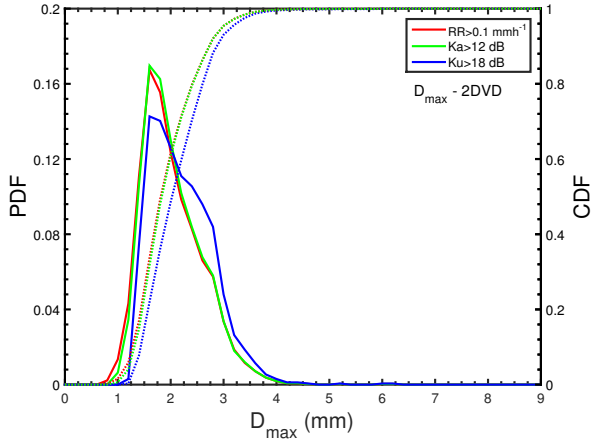

(e)

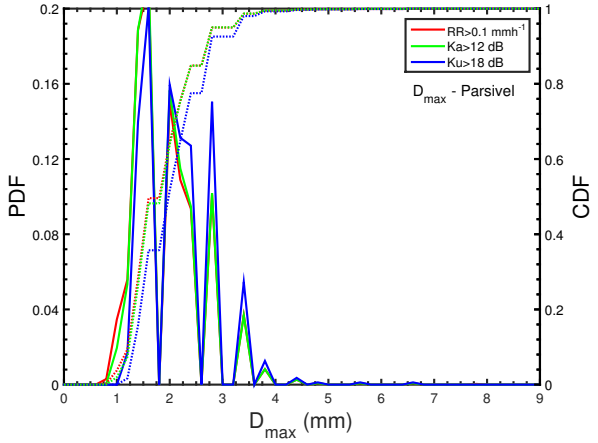

(f)

Figure 5.3: PDF and CDF of DSD parameters: (a) and (b) N_W, (c) and (d) D_{mass}, (e) and (f) D_{max} for 2DVD and Parsivel data, respectively.

The tables 5.1 and 5.2 show the statistical properties of PDF for all eighteen analyzed parameters for 2DVD and Parsivel data, respectively. The numeric values of threshold, as well the measurement units of parameters are not shown for a better visualization. There is very good agreement between the two instruments and also between the different rain/no-rain threshold. The low mean and also 90^{th} values of RR and reflectivity at different bands indicate the dominance of stratiform rain events during the measurement period. The D_{mass} and D_{max} values confirm the great contribution of low- and mid-size drops to the measured DSDs. Both the instruments have appreciable difference in estimation of the two intercept parameters, $N_T{}^*$ and N_W where the former has sensibly lower values than the latter.

5.2.2 Correlation distance analysis

The three-parameter exponential function is then calculated for each of the considered parameters. In the figures 5.4 and 5.5 are shown, both for 2DVD and Parsivel, the experimental correlation for each disdrometers pair (point for 2DVD and star for Parsivel), the three-parameter exponential function (blu line for 2DVD and red line for Parsivel) with d_0, s_0 and RMSE values for $R_0 = 0.99$, since there is no difference in results considering $R_0 = 0.90$ or 0.95. The RMSE value reflects the goodness of the experimental data fit by using the three-parameter exponential function. The results refer to RR threshold.

An excellent agreement is evident in spatial variability of LWC, RR, and N_T between the 2DVD and Parsivel, as well as for $N_T{}^*$ and N_W even if the functions slightly diverge at the larger distances. Correlation distances of RR are 4.2 km and 4.5 km for Parsivel and 2DVD, respectively, when nugget parameter is 0.99 (figure 5.4a) but do not change for nugget parameters of 0.90 and 0.95.

	Mean			STD			Median			10^{th} Percentile			90^{th} Percentile		
	RR	$\mathbf{Z_{K_a}}$	$\mathbf{Z_{K_u}}$	**RR**	$\mathbf{Z_{K_a}}$	$\mathbf{Z_{K_u}}$	**RR**	$\mathbf{Z_{K_a}}$	$\mathbf{Z_{K_u}}$	**RR**	$\mathbf{Z_{K_a}}$	$\mathbf{Z_{K_u}}$	**RR**	$\mathbf{Z_{K_a}}$	$\mathbf{Z_{K_u}}$
RR	1.10	1.10	1.43	0.94	0.94	1.02	0.87	0.87	1.11	0.33	0.35	0.68	2.16	2.16	2.65
LWC	0.07	0.07	0.09	0.05	0.05	0.06	0.06	0.06	0.07	0.02	0.02	0.05	0.14	0.14	0.17
$\mathbf{Z_{K_a}}$	26.3	26.4	27.8	27.6	27.6	28.2	23.4	23.5	25.8	17.8	18.4	21.6	30.1	30.1	31.0
$\mathbf{Z_{K_u}}$	26.8	26.8	28.4	33.1	33.1	34.0	21.9	22.0	24.3	16.7	17.3	20.3	29.9	29.9	31.0
$\mathbf{Z_H}$	26.4	26.5	28.0	32.6	32.6	33.6	22.3	22.4	24.7	17.0	17.6	20.7	29.6	29.6	30.7
$\mathbf{Z_{dr}}$	0.38	0.38	0.44	-11.35	-11.39	-10.83	0.29	0.30	0.35	0.14	0.15	0.17	0.68	0.68	0.76
$\mathbf{K_{dp}}$	0.010	0.010	0.013	0.015	0.015	0.018	0.006	0.006	0.009	0.002	0.002	0.004	0.020	0.020	0.025
$\mathbf{D_{mass}}$	1.11	1.13	1.20	0.30	0.29	0.31	1.05	1.06	1.15	0.79	0.82	0.86	1.52	1.52	1.59
$\mathbf{D_{max}}$	2.03	2.05	2.22	0.58	0.57	0.59	1.92	1.94	2.13	1.40	1.44	1.54	2.83	2.83	2.97
X	1.83	1.83	1.86	0.26	0.25	0.22	1.79	1.79	1.83	1.56	1.56	1.60	2.15	2.14	2.15
$\mathbf{N_T}$	447	442	526	407	410	467	340	331	400	141	130	181	818	814	950
$\mathbf{N_T}^*$	302	290	327	394	390	444	184	176	209	59	55	63	641	607	639
$\mathbf{log(N_T}^*\mathbf{)}$	2.48	2.46	2.51	2.60	2.59	2.65	2.26	2.25	2.32	1.77	1.74	1.80	2.81	2.78	2.81
$\mathbf{N_W}$	6524	6215	6810	9294	9118	10219	3468	3253	3967	873	833	861	14770	13502	14378
$\mathbf{log(N_W)}$	3.81	3.79	3.83	3.97	3.96	4.01	3.54	3.51	3.60	2.94	2.92	2.93	4.17	4.13	4.16
$\mu(\sigma_{\mathbf{DM}})$	5.7	5.8	5.4	3.5	3.5	3.4	5.2	5.2	4.7	1.7	1.7	1.7	10.6	10.6	10.1
$\mu(N_{\mathbf{T}}{}^*)$	4.8	4.9	4.4	2.9	2.9	2.7	4.4	4.4	3.8	1.6	1.6	1.5	8.8	8.8	8.1
$\mu(N_{\mathbf{W}})$	5.2	5.1	4.7	3.4	3.3	3.1	4.5	4.5	4.1	1.5	1.5	1.5	9.9	9.6	9.0

Table 5.1: Mean, standard deviation (STD), median, 10^{th} and 90^{th} percentile of all 18 parameters for 2DVD data as function of the rain/no-rain threshold. RR-0.1 mmh^{-1}, Z_{K_a}-12 dB, Z_{K_u}-18 dB. For the units refers to table 4.3.

	Mean			STD			Median			10^{th} Percentile			90^{th} Percentile		
	RR	$\mathbf{Z_{K_a}}$	$\mathbf{Z_{K_u}}$	**RR**	$\mathbf{Z_{K_a}}$	$\mathbf{Z_{K_u}}$	**RR**	$\mathbf{Z_{K_a}}$	$\mathbf{Z_{K_u}}$	**RR**	$\mathbf{Z_{K_a}}$	$\mathbf{Z_{K_u}}$	**RR**	$\mathbf{Z_{K_a}}$	$\mathbf{Z_{K_u}}$
RR	1.15	1.15	1.49	1.00	1.00	1.10	0.91	0.92	1.15	0.36	0.37	0.70	2.22	2.22	2.68
LWC	0.08	0.08	0.10	0.06	0.06	0.06	0.07	0.07	0.08	0.03	0.03	0.05	0.14	0.14	0.18
$\mathbf{Z_{K_a}}$	26.2	26.2	27.6	27.8	27.8	28.4	23.2	23.2	25.5	17.3	17.9	21.1	29.9	29.9	30.9
$\mathbf{Z_{K_u}}$	27.7	27.7	29.3	34.8	34.7	35.7	21.7	21.7	24.0	16.4	16.9	20.0	30.2	30.2	31.6
$\mathbf{Z_H}$	27.7	27.4	29.0	36.6	35.6	36.6	22.1	22.1	24.4	16.7	17.2	20.4	29.7	29.7	31.0
$\mathbf{Z_{dr}}$	0.39	0.40	0.47	-9.67	-10.39	-9.77	0.27	0.28	0.35	0.13	0.14	0.16	0.76	0.76	0.83
$\mathbf{K_{dp}}$	0.011	0.011	0.015	0.022	0.021	0.026	0.006	0.006	0.010	0.002	0.002	0.005	0.022	0.022	0.028
$\mathbf{D_{mass}}$	1.09	1.10	1.17	0.32	0.31	0.33	1.01	1.02	1.10	0.77	0.79	0.84	1.50	1.50	1.58
$\mathbf{D_{max}}$	1.96	1.98	2.15	0.63	0.61	0.64	1.93	1.93	1.93	1.42	1.42	1.42	2.83	2.83	2.83
X	1.80	1.80	1.85	0.27	0.27	0.25	1.77	1.77	1.82	1.51	1.51	1.56	2.16	2.15	2.18
$\mathbf{N_T}$	296	289	329	281	280	313	204	198	259	79	75	96	594	566	624
$\mathbf{N_T}^*$	951	920	1045	2271	2252	2582	319	306	328	80	76	81	2128	2006	2337
$\mathbf{log(N_T}^*\mathbf{)}$	2.98	2.96	3.02	3.36	3.35	3.41	2.50	2.49	2.52	1.91	1.88	1.91	3.33	3.30	3.37
$\mathbf{N_W}$	7313	6873	7249	10915	10504	11478	3588	3379	3451	128	123	144	16790	15078	13930
$\mathbf{log(N_W)}$	3.86	3.84	3.86	4.04	4.02	4.06	3.55	3.53	3.54	2.11	2.09	2.16	4.23	4.18	4.14
$\mu(\sigma_{\mathbf{DM}})$	5.4	5.4	4.8	4.2	4.2	4.0	4.6	4.5	3.9	0.7	0.7	0.6	11.2	11.2	10.4
$\mu(N_{\mathbf{T}}{}^*)$	6.0	5.9	5.2	3.9	3.8	3.5	5.1	5.1	4.4	1.9	1.9	1.8	11.4	11.2	9.8
$\mu(N_{\mathbf{W}})$	5.0	4.9	4.4	4.0	3.9	3.7	4.0	4.0	3.4	0.8	0.7	0.7	10.5	10.2	9.3

Table 5.2: As for table 5.1 but for Parsivel data.

The shape parameters are just over 1 and the root mean square errors aere less

than 0.1 indicating that the fit is very good. The excellent agreement in the spatial variability of LWC (figure 5.4b), which correlation distance is comparable with which obtained for RR, reflects in a very good agreement in mid-size drops measurements between the two disdrometers types.

Previous studies on spatial variability rely on rain gauge measurements where the gauge accumulations at different time integration periods were the input to derive the correlations. Moreover, the configuration of the gauges with minimum and maximum distances, gauge density, rainfall type, data collection and integration periods are different than in this study. As an example, Ciach and Krajewski (2006) found 7.7 km correlation distance and the shape parameter of 1.1 at 1-minute accumulation in Central Oklahoma, while Tokay and Ozturk (2012) found the correlation distance of 14 km and shape parameter of 0.37 at 5-minute accumulation from Wallops Island measurements. However, the correlation distances in the present work seem to be relatively short for late fall winter type of precipitation, but the maximum separation distance was relatively short and the data collected at high temporal scale of mm per hour.

For the reflectivity at K_a-, K_u- and S-band (Rayleigh), there is a worse agreement with respect to RR and LWC (especially for K_u band). This reflects in a correlation distance noticeably higher for 2DVD with respect to Parsivel (figures 5.4c- 5.4e), and generally higher than RR and LWC, ranging between 10 and 17 Km about. The quantization effect in Parsivel probably contributed to the relatively lower correlations. As highlighted, the bin width is over 0.5 mm between 2.6 mm and 5.3 mm and is over 1 mm between 5.3 mm and 10 mm. The large drops contribute to the reflectivity and the reflectivity calculated from the mid-size diameter may differ from that from the actual diameter of the raindrop. For instance, a drop at 5.35 mm in diameter is registered as 5.66 mm raindrop and the difference for a single drop is more than 1 dB. The spatial variability of Z_{dr} has a mixture of higher and lower correlations at a given distance in

Parsivel and the resultant fit is relatively poor where RMSE is just above 0.1 (figure 5.4f). The 2DVD, on the other hand, has a better fit and higher correlations.

Considering DSD parameters, the 2DVD based correlations are higher and uniformly decreasing with the distance resulting in better fit for the exponential function than in Parsivel for D_{mass} and D_{max} (figures 5.5a- 5.5b). The quantization error is the major error source in determining D_{max} using Parsivel database. Both high and low correlations were at distances comparable to each other resulting in higher RMSE values in Parsivel based fitting. The correlation distance for D_{mass} is approximately 20 km, based on 2DVD observations, while higher values are obtained for D_{max}. On the other side, the correlation distance obtained with Parsivel are lower for both parameters. D_{max} has also a value of the lowest for s_0, both for 2DVD and Parsivel, while for the most of parameters s_0 ranges between 0.35 and 0.90 and exceeds the value of 1.0 for RR.

The same features are also evident in spatial variability of normalized intercept parameters $N_T{}^*$, N_W (figures 5.5c- 5.5d) and N_T, $\log(N_T{}^*)$ and $\log(N_W)$ (not shown). The correlations are high (>0.85) even at the largest separation distance and do not show a significant decrease with distance when 2DVD database is used. This resulted in very high correlation distances, even equal to the maximum value set for d_0 for $N_T{}^*$. The correlation distances are 29 km and 27 km for $N_T{}^*$ and N_W respectively when Parsivel database is used. The shape parameters were less than 1 but quite different between 2DVD and Parsivel based fittings for both $N_T{}^*$ and N_W. While RMSE values are low, the fitting is better for 2DVD dataset.

The shape parameters that are derived from $N_T{}^*$ and N_W based gamma distributions showed significant differences between them and between the two disdrometer database. The correlation distances are noticeably lower in $\mu(N_W)$ than in $\mu(N_T{}^*)$ and in Parsivel database than in 2DVD database (figures 5.5e- 5.5f). Fits are good with low RMSE values for both parameters and for both disdrometer database. Unlike normalized inter-

cept parameters, the shape parameter is quite sensitive to the goodness of the gamma fit to the observed DSD. The shape parameters show the lowest s_0 values and this influences the trend of correlation function and, consequently, the obtained distance. Low s_0 values indicate low correlation at small distances and the corresponding relative high correlation distances reveal a negligible change of correlation coefficient as function of distance.

The correlations derived between the pair of measurements can be sensitive to the sample size. In this study, the dataset included the minutes where all six 2DVD and six Parsivel reporting rainfall for a given rain rate or minimum reflectivity thresholds. Unfortunately, the malfunctioning of disdrometers, particularly 2DVDs, is occasionally overlapped with non-rainy periods. It is rather difficult to separate the non-rainy periods from malfunction periods. This was the reason to include only the periods where all disdrometers reported rainfall. As a result, the sample size became somewhat limited especially if the interest is the spatial variability of a particular event.

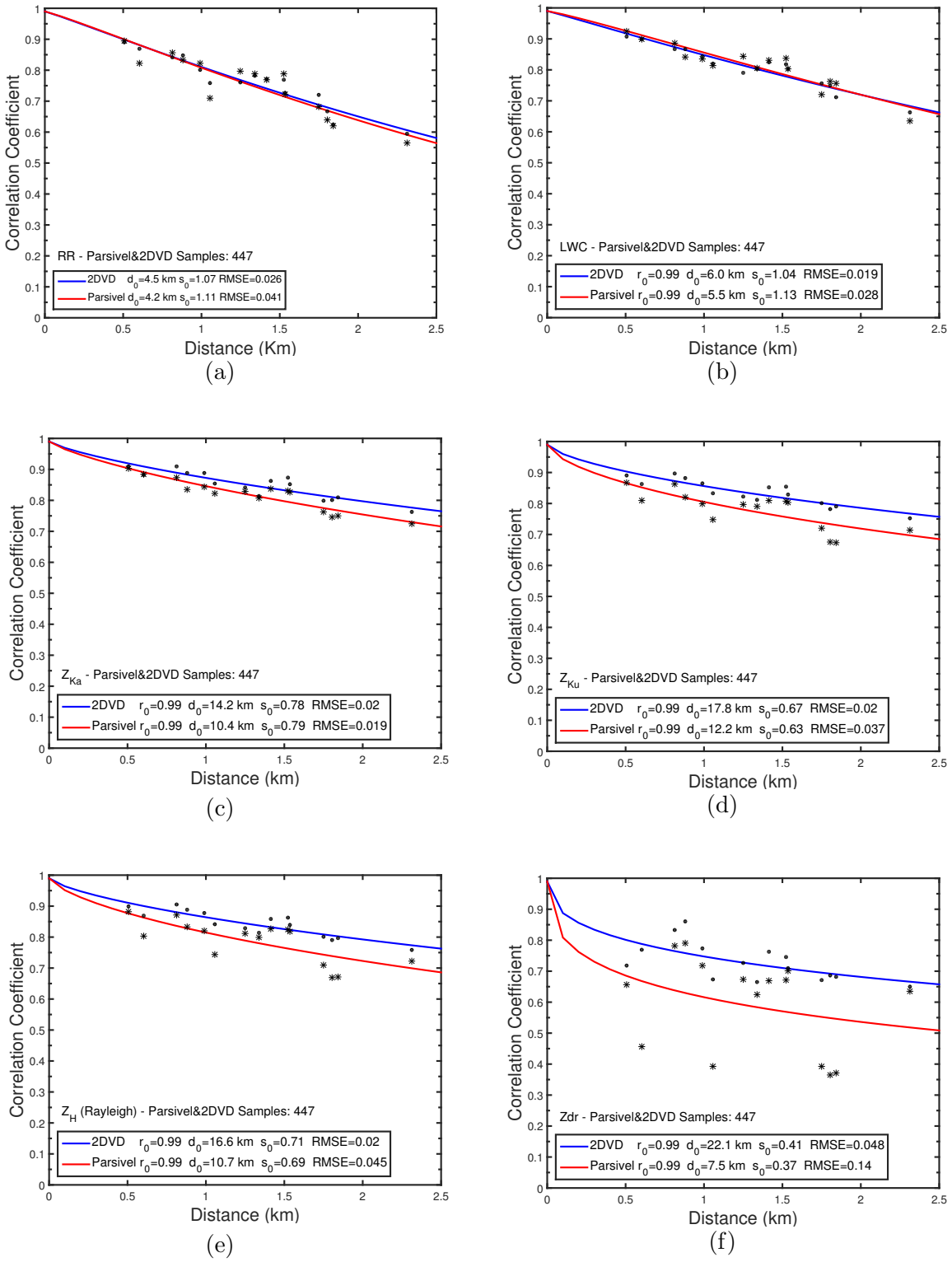

Figure 5.4: Three-parameter exponential function of 2DVD (blu line) and Parsivel (red line) for: (a) RR, (b) LWC, (c) Z_{K_a}, (d) Z_{K_u}, (e) Z_H and (f) Z_{dr}.

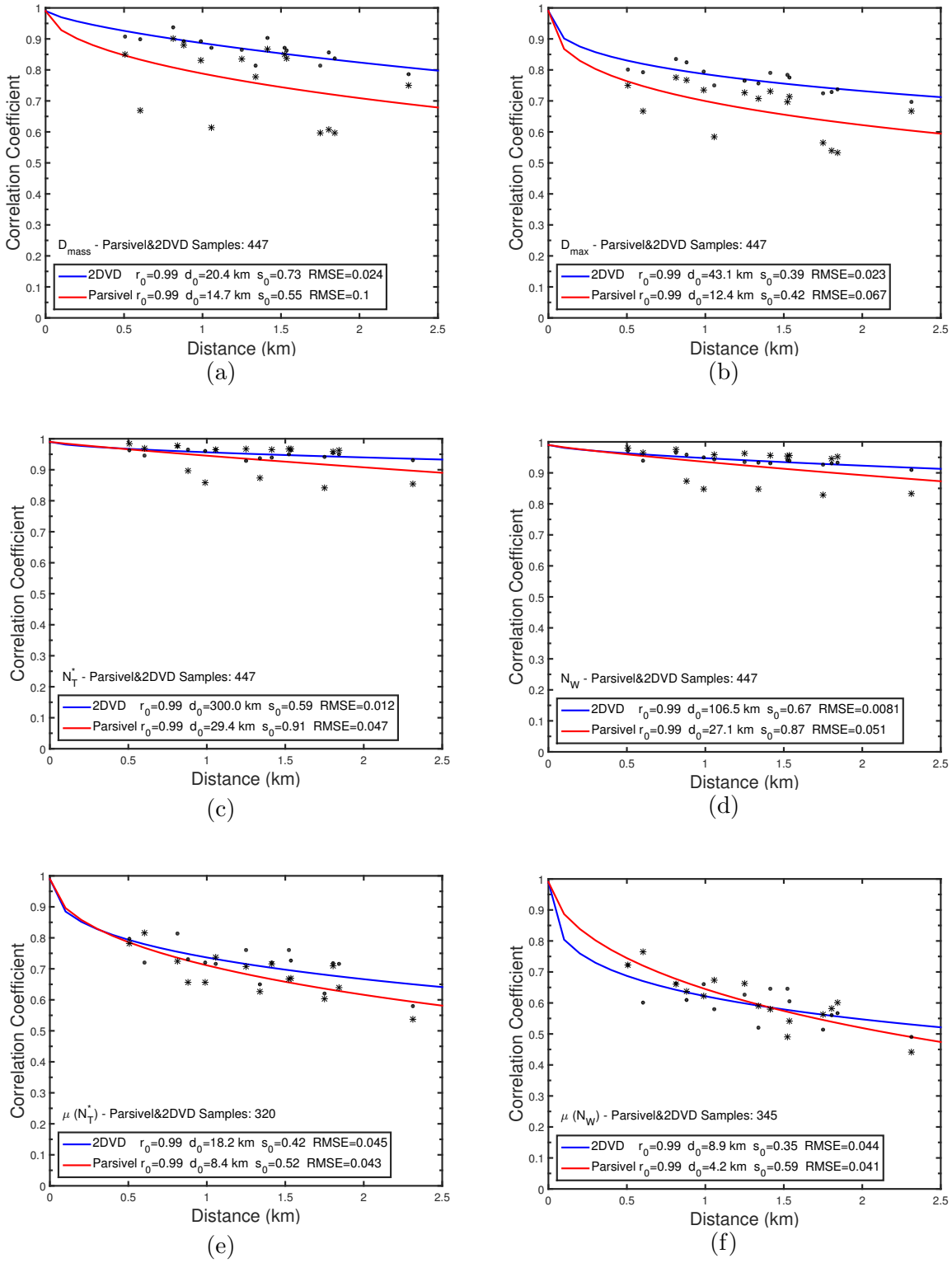

Figure 5.5: Three-parameter exponential function of 2DVD (blu line) and Parsivel (red line) for: (a) D_{mass}, (b) D_{max}, (c) $N_t{}^*$, (d) N_W, (e) $\mu(N_T{}^*)$ and (f) $\mu(N_W)$.

The figure 5.6 summarizes the correlation distance d_0 (5.6a), the shape parameter s_0 (5.6b) and the RMSE (5.6c) for all the 18 DSD and integral parameters that are derived from 2DVD (blue point) and Parsivel (red star) database.

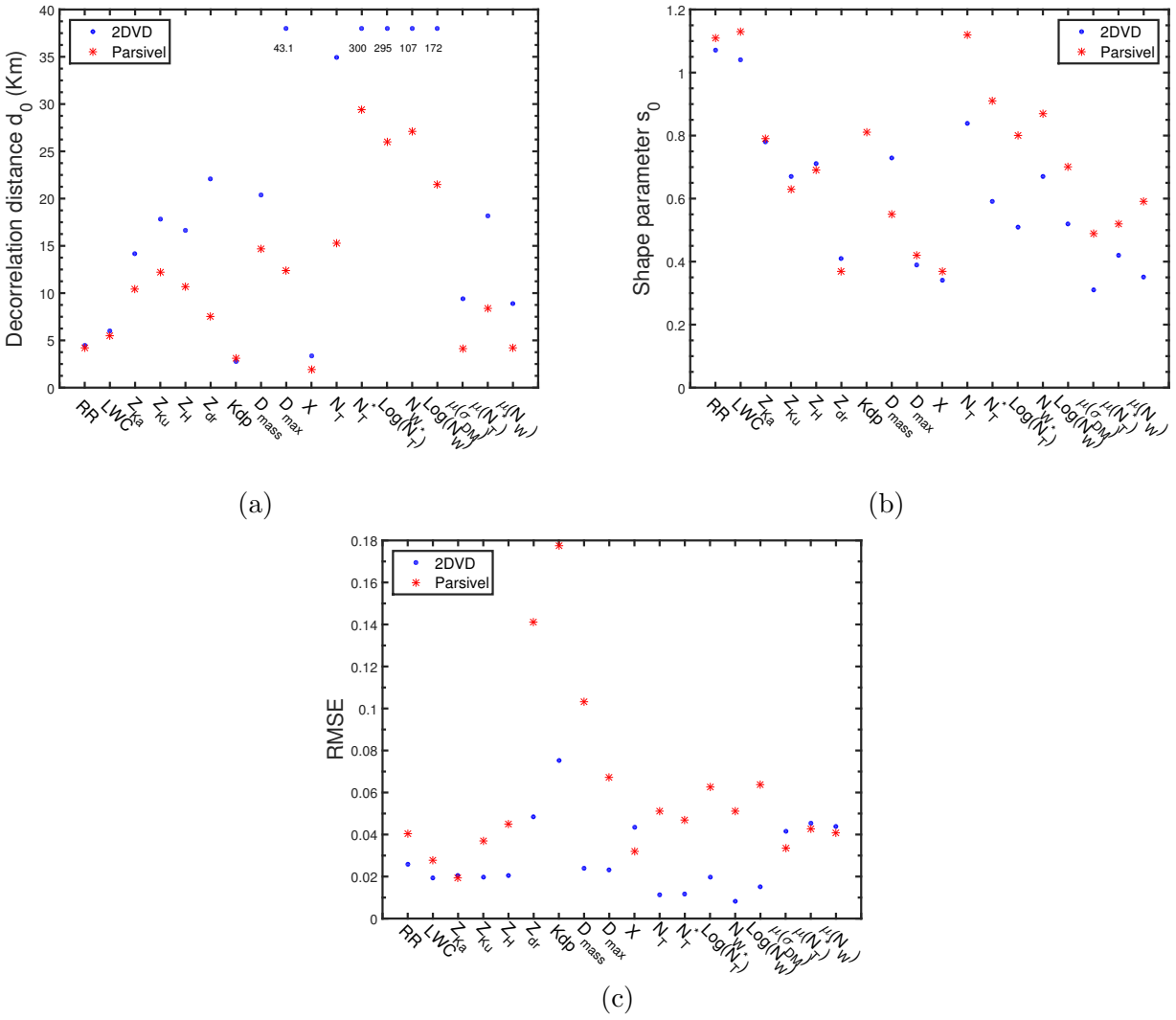

(a) (b)

(c)

Figure 5.6: The correlation distance d_0 (a), the shape parameter s_0 (b) and the RMSE (c) for all DSD parameters for 2DVD (blue point) and Parsivel (red star).

Both DSD and rain parameters are function of observed size spectra but have different sensitivity to the small, mid-size, and large drop size regimes. The comparison between the two disdrometers at a size range that mainly contributes to a particular DSD and/or rain parameters results in a very good agreement in d_0 and s_0 if the three-parameter fit is successful. The figures (5.6b) and (5.6c) generally show lower values for 2DVD with respect to Parsivel for both the parameters. The difference is more marked in the RMSE (figure 5.6c). The RMSE is the measure of goodness of the three-parameter fit and is relatively high when observed correlations of the two instruments at around the same distances are substantially different. In general, the RMSE has low values, less than 0.08 if Parsivel data are considered while the limit decreases to 0.05 with 2DVD data, demonstrating the high confidence on the goodness of the fit. Comparing the two instruments, the 2DVD has appreciably lower RMSE values than Parsivel for the most of the parameters. This is reflected in generally higher correlation distance (figure 5.6a) obtained with 2DVD. For a DSD or rain parameter where correlations are high and do not show significant decrease with distance, d_0 was high. For instance, d_0 is 300 km for $N_T{}^*$, which is the upper limit of initial guess.

Figure 5.7 shows the sensitivity of correlation distance and shape parameter of the exponential function to the choice of rain/no-rain threshold using 2DVD dataset. The parameters of exponential function have much less sensitivity to the rain/no-rain threshold than the disdrometer type. The dependence on the rain/no-rain threshold of the parameters of the exponential function is slightly greater for Parsivel (not shown) than 2DVD. The differences in rain/no-rain threshold do not alter the goodness of fit significantly as RMSE remained the same for all rain/no-rain thresholds.

In addition to the rain/no-rain thresholds, the parameters of exponential function are sensitive to many other factors and therefore it is difficult to compare the studies of the spatial variability. Each experimental study offers a different characteristic of

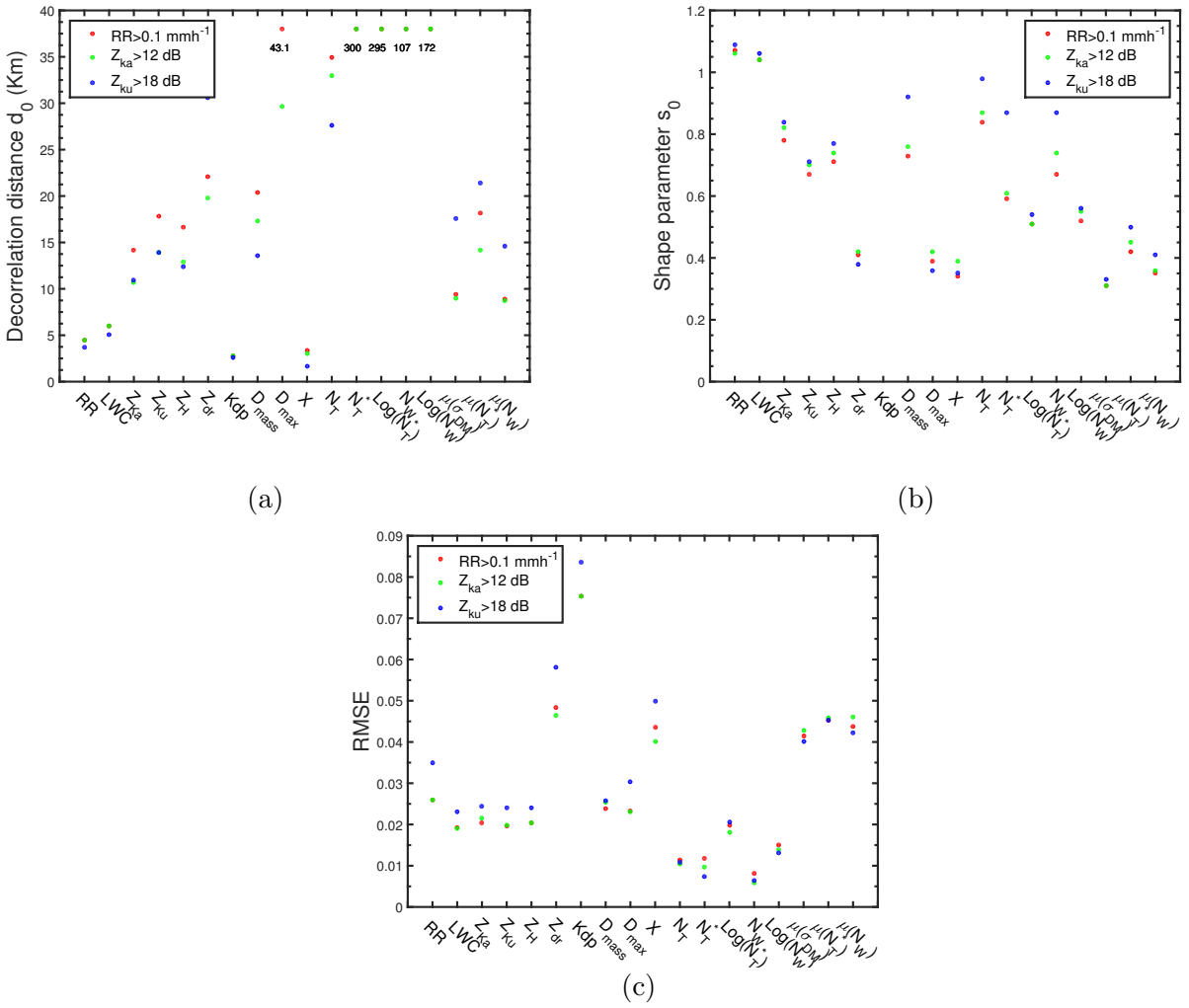

Figure 5.7: The correlation distance d_0 (a), the shape parameter s_0 (b) and the RMSE (c) for all DSD parameters for 2DVD as function of threshold.

the spatial variability. The dense gauge network was the key to have an excellent fit keeping RMSE very low. But disdrometers provide the spatial variability at high temporal resolution. It is a direct measurement of DSD and therefore provides much needed information beyond rain intensity within the domain of observations. Perhaps, the number of disdrometers available is questionable for the robustness of parameters

of exponential function.

5.2.3 Sensitivity Studies - Partial beam filling

In order to test the robustness of fit, an additional analysis is made. The analysis regards the estimation of the three-parameter exponential function, only for RR parameter, eliminating one of the stations (figure 5.8). This reduces the pair of correlations from 15 to 10. At some instances, the elimination of station reduced the minimum and maximum disdrometer separation distances. From theoretical point of view, this analysis tries to replicate partial beam filling of satellite footprint or radar pixel from DPR or a ground based radar. Both the correlation distance d_0 and the shape parameter s_0 and the RMSE do not show any significant changes for the exclusion of one of the sites and with respect to when all sites are considered. Moreover, spatial variability of rainfall do not show any significant differences between 2DVD and Parsivel. Likely, the dominance of frontal widespread rain during observation period and the condition of all twelve instruments reporting rainfall are perhaps the two important factors for the insensitivity of the correlation distances of RR to the exclusion of a site. Very similar results are obtained considering both 12 dB-Z_{K_a} and 15 dB-Z_{K_u}. Each plot reports the abbreviation of the instrument ("APU" for Parsivel and "SN" for 2DVD) with the serial number.

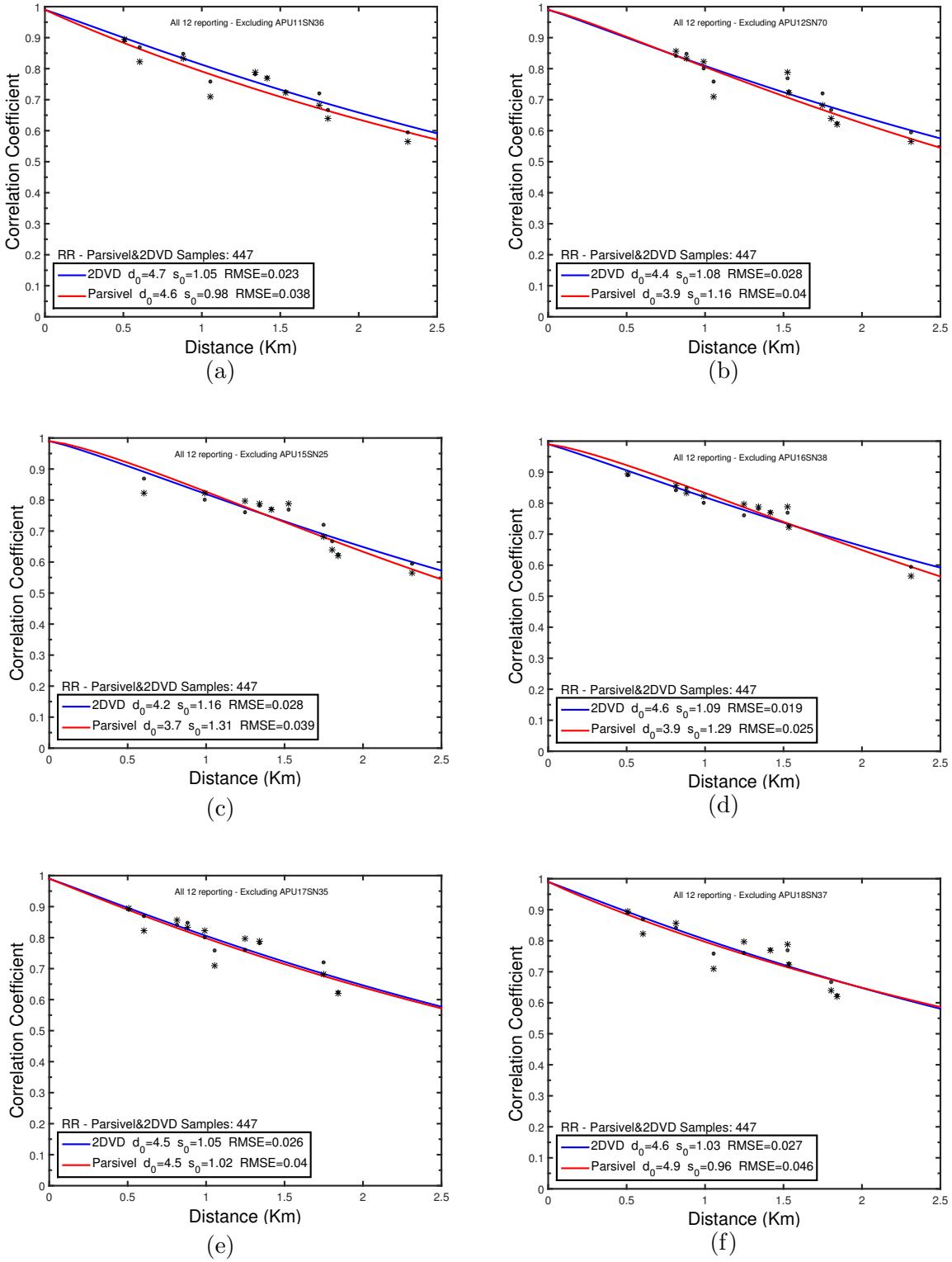

Figure 5.8: The RR three-parameter exponential function of 2DVD (blu line) and Parsivel (red line) excluding one couple of instruments: (a) APU11-SN36, (b) APU12-SN70, (c) APU15-SN25, (d) APU16-SN38, (e) APU17-SN35 and (f) APU18-SN37.

5.3 Results: MC3E dataset

5.3.1 Dataset description

The same analysis type made for Wallops data, has been made for MC3E data. Referring to the table 2.2 the data from seven 2DVD were collected during the MC3E campaign, so that a comparison 2DVD-Parsivel was not possible. The distance among the instruments ranges from 0.4 to 9.2 km, so that the measuring field is comparable with a satellite footprint or radar pixel, as for Wallops dataset. The larger distances among the instruments with respect to Wallops distances, allow to have an unprecedented comparison of the spatial variability at two different small scales using two disdrometric datasets. The measuring field is described in figure 5.9. The MC3E dataset for this study is obtained using the same rain/no-rain thresholds used for Wallops dataset. In this case, the dataset size according the different thresholds when all seven 2DVD exceed the considered threshold, results in:

- RR$>$ 0.1 mmh^{-1} (592 minutes);
- $Z_{K_a}>$ 12 dB (589 minutes);
- $Z_{K_u}>$ 12 dB (574 minutes);
- $Z_{K_u}>$ 15 dB (516 minutes);
- $Z_{K_u}>$ 18 dB (396 minutes);

The same eighteen DSD parameters are analyzed in terms of three-parameter exponential function. Since was not possible to compare two different instruments types as for Wallops (2DVD and Parsivel), the three-parameter exponential function was estimated

Figure 5.9: Measuring field of MC3E campaign.

as function of nugget parameter R_0, giving the same values of 0.90, 0.95 and 0.99 assigned also for Wallops analysis.

The mean RR is almost three times higher than Wallops dataset (ranges from 3.05 to 3.53 mmh^{-1} for 12 dB-Z_{K_a} and 18 dB-Z_{K_u} respectively), while the maximum RR measured was 92.8 mmh^{-1}. The reflectivity thresholds result in missing the 0.51% and 33% in rain occurrence, respectively, while the 1.3% and 23% of rain amount is missed.

The figure 5.10 shows the PDF and CDF for three different rain/no-rain threshold. In general, there is an excellent agreement considering the RR and 12 dB-Z_{K_a} threshold, but a slight difference for 18 dB-Z_{K_u} threshold for all the parameters considered. With respect to the Wallops data, is evident the influence of season (late spring for MC3E with respect to mainly fall-winter for Wallops) on the PDF and CDF. The distributions of both DSD integral parameters (figures 5.10a- 5.10c) and DSD parameters (figures

5.10d- 5.10f) move toward higher values. In particular, the D_{max} and D_{mass} show a greater contribution of larger diameter, that is reflected by a greater contribution of higher values for RR and reflectivity at K_a and K_u band (significant contribution for RR$>$ 5mmh^{-1} and Z_{K_a}-$Z_{K_u}>$ 35 dB. Less marked differences show the N_W distribution with respect to the 2DVD Wallops distribution.

The table 5.3 shows the statistical properties of PDF for all eighteen analyzed parameters for 2DVD data. As for the tables 5.1 and 5.2, the numeric values of threshold, as well the measurement units of parameters are not shown for a better visualization. Again, there is a very good agreement between the three rain/no-rain threshold. It is evident the different precipitation type from MC3E data with respect to Wallops data. The mean RR is almost three time higher than Wallops mean RR and also the reflectivity at different bands is generally 10 dB higher. The contribution to the DSD of larger drops is evident from D_{mass} and D_{max} values, and also from Z_{dr} values that are about double of Z_{dr} at Wallops. This reflects in lower values for $N_T{}^*$ and N_W (also for MC3E data maintains the marked difference between the two values).

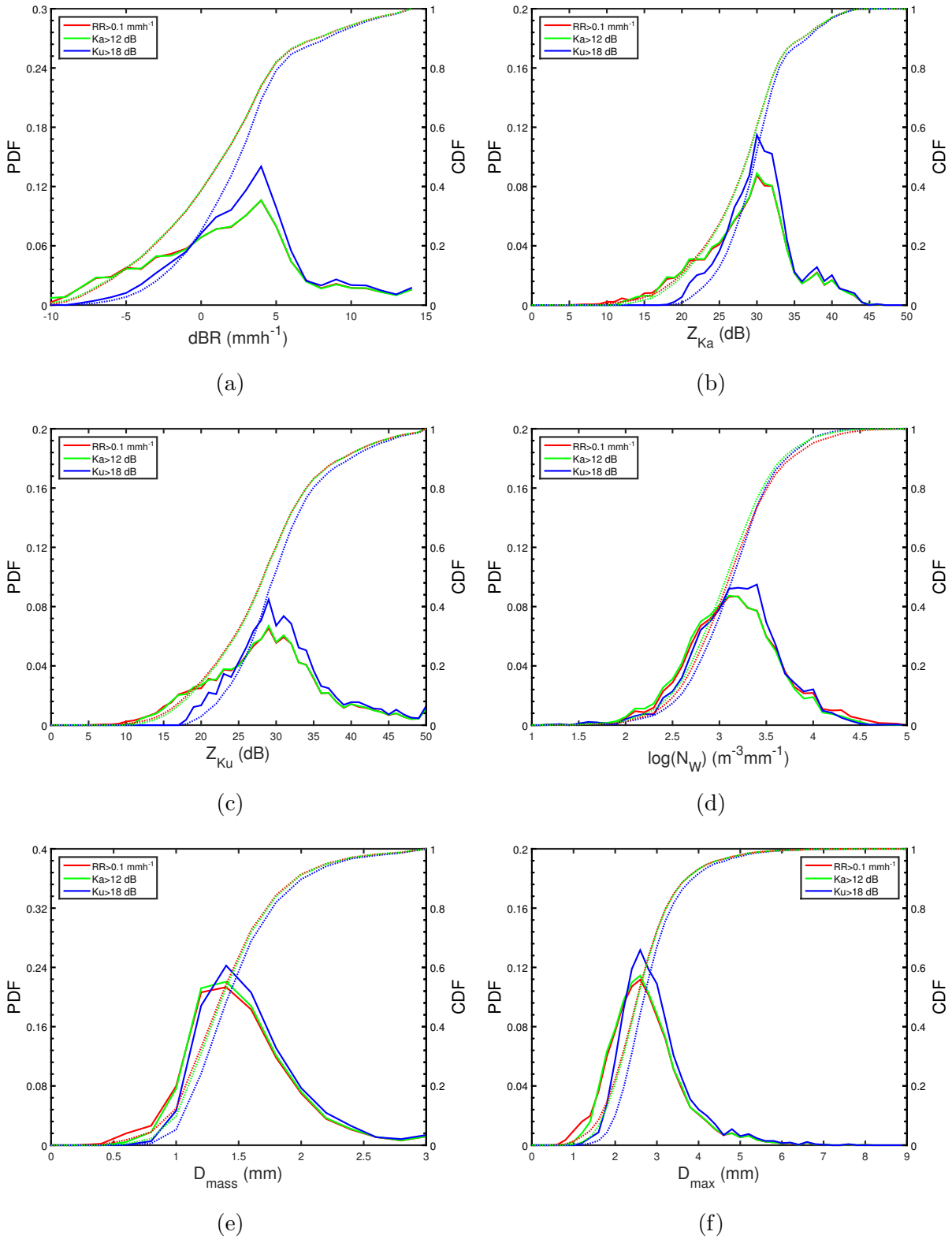

Figure 5.10: PDF and CDF of DSD integral parameters: (a) RR, (b) Z_{K_a}, (c) Z_{K_u}, (d) N_W, (e) D_{mass} and (f) D_{max} for 2DVD data.

	Mean			STD			Median			10th Percentile			90th Percentile		
	RR	$\mathbf{Z_{K_a}}$	$\mathbf{Z_{K_u}}$	**RR**	$\mathbf{Z_{K_a}}$	$\mathbf{Z_{K_u}}$	**RR**	$\mathbf{Z_{K_a}}$	$\mathbf{Z_{K_u}}$	**RR**	$\mathbf{Z_{K_a}}$	$\mathbf{Z_{K_u}}$	**RR**	$\mathbf{Z_{K_a}}$	$\mathbf{Z_{K_u}}$
RR	3.07	3.05	3.53	5.48	5.46	5.72	1.57	1.56	2.02	0.31	0.30	0.62	6.59	6.48	7.69
LWC	0.15	0.15	0.17	0.22	0.22	0.23	0.09	0.08	0.11	0.02	0.02	0.04	0.31	0.31	0.34
$\mathbf{Z_{K_a}}$	32.7	32.6	33.3	35.2	35.2	35.2	29.2	29.3	30.3	20.2	20.6	24.8	36.4	36.4	37.3
$\mathbf{Z_{K_u}}$	37.3	37.3	38.0	43.5	43.5	43.9	28.8	28.9	30.2	18.6	19.0	23.4	39.3	39.4	40.4
$\mathbf{Z_H}$	36.2	36.2	36.9	42.6	42.6	43.1	28.7	28.7	29.9	18.9	19.3	23.6	38.1	38.1	39.1
$\mathbf{Z_{dr}}$	0.74	0.75	0.82	-8.14	-8.16	-8.06	0.60	0.61	0.67	0.27	0.29	0.36	1.23	1.24	1.35
$\mathbf{Z_{dp}}$	0.051	0.051	0.059	0.144	0.144	0.156	0.017	0.017	0.022	0.002	0.002	0.006	0.104	0.103	0.122
$\mathbf{D_{mass}}$	1.51	1.54	1.59	0.44	0.42	0.41	1.46	1.47	1.51	1.06	1.10	1.16	2.05	2.06	2.11
$\mathbf{D_{max}}$	2.73	2.77	2.94	0.88	0.86	0.81	2.63	2.65	2.79	1.76	1.83	2.10	3.80	3.82	3.95
X	1.81	1.80	1.86	0.26	0.26	0.24	1.79	1.78	1.84	1.49	1.48	1.56	2.13	2.13	2.16
$\mathbf{N_T}$	465	443	513	536	524	541	306	288	362	77	69	111	1015	974	1042
$\mathbf{N_T}^*$	193	169	190	269	225	226	107	99	125	26	22	33	447	385	410
$\mathbf{log(N_T}^*\mathbf{)}$	2.29	2.23	2.28	2.43	2.35	2.35	2.03	2.00	2.10	1.41	1.35	1.52	2.65	2.59	2.61
$\mathbf{N_W}$	3087	2490	2671	5835	3992	3931	1439	1332	1574	373	332	439	6482	5359	5845
$\mathbf{log(N_W)}$	3.49	3.40	3.43	3.77	3.60	3.59	3.16	3.12	3.20	2.57	2.52	2.64	3.81	3.73	3.77
$\mu(\sigma_{\mathbf{DM}})$	5.0	4.9	4.3	3.7	3.7	3.3	4.1	4.1	3.5	1.1	1.1	1.0	10.1	10.0	8.7
$\mu(N_{\mathbf{T}}{}^*)$	3.9	3.8	3.2	3.1	3.0	2.6	3.1	3.1	2.7	0.9	0.9	0.7	7.9	7.6	6.4
$\mu(N_{\mathbf{W}})$	4.5	4.5	3.9	3.4	3.3	2.9	3.8	3.7	3.2	1.1	1.1	0.9	8.9	8.8	7.6

Table 5.3: As for table 5.1 but for 2DVD data of MC3E dataset.

5.3.2 Correlation distance analysis

The three-parameter exponential function has been calculated as function of R_0. The figures 5.11 and 5.12 show the correlation function for the selected DSD parameters calculated for three R_0 values for RR threshold. The difference among the three obtained functions is negligible and they are mostly overlapping. The RR correlation distance (figure 5.11a) is around 3.6 km for $R_0 = 0.99$ (ranges from 3.6 to 4.0 km using $R_0 = 0.99$ and $R_0 = 0.90$ respectively) and it is very similar to the LWC correlation distance (figure 5.11b), but above all, the results are very close to those obtained from Wallops data. The shape parameter is just over 1 also in this case both for RR and LWC, while higher values are obtained for RMSE (close or just over 0.1).

Slightly higher values, ranging from 5.5 and 6.0 km about, are obtained for reflectivity at K_a and K_u band (figures 5.11c- 5.11d). These values are generally lower than the corresponding obtained from Wallops dataset. As for RR and LWC, the shape parameter is over 1 and the RMSE is greater than the corresponding RMSE for Wallops dataset. Probably the greater contribution of larger drops has influence both on the correlation distance and on the goodness of data fit, that anyway remains good.

Negligible differences in terms of correlation distance and RMSE, with respect to reflectivity at K_a and K_u band, are found if Z_H and Z_{dr} parameters are considered. Although the correlation distances are lower than the ones found for the Wallops dataset, the DSD integral parameters are correlated with a radar pixel and satellite footprint.

Comparable correlation distance of RR, LWC, Z_{K_a} and Z_{K_u} are obtained for D_{mass} and D_{max} (figures 5.12a- 5.12b). The values range from 5 to 5.5 km and from 4.1 to 4.6 km for D_{mass} and D_{max}, respectively. The shape parameter is again close to 1, while the RMSE reaches lower values, especially for D_{mass}. The correlation distances for these parameter are sensibly lower than the founding for Wallops dataset.

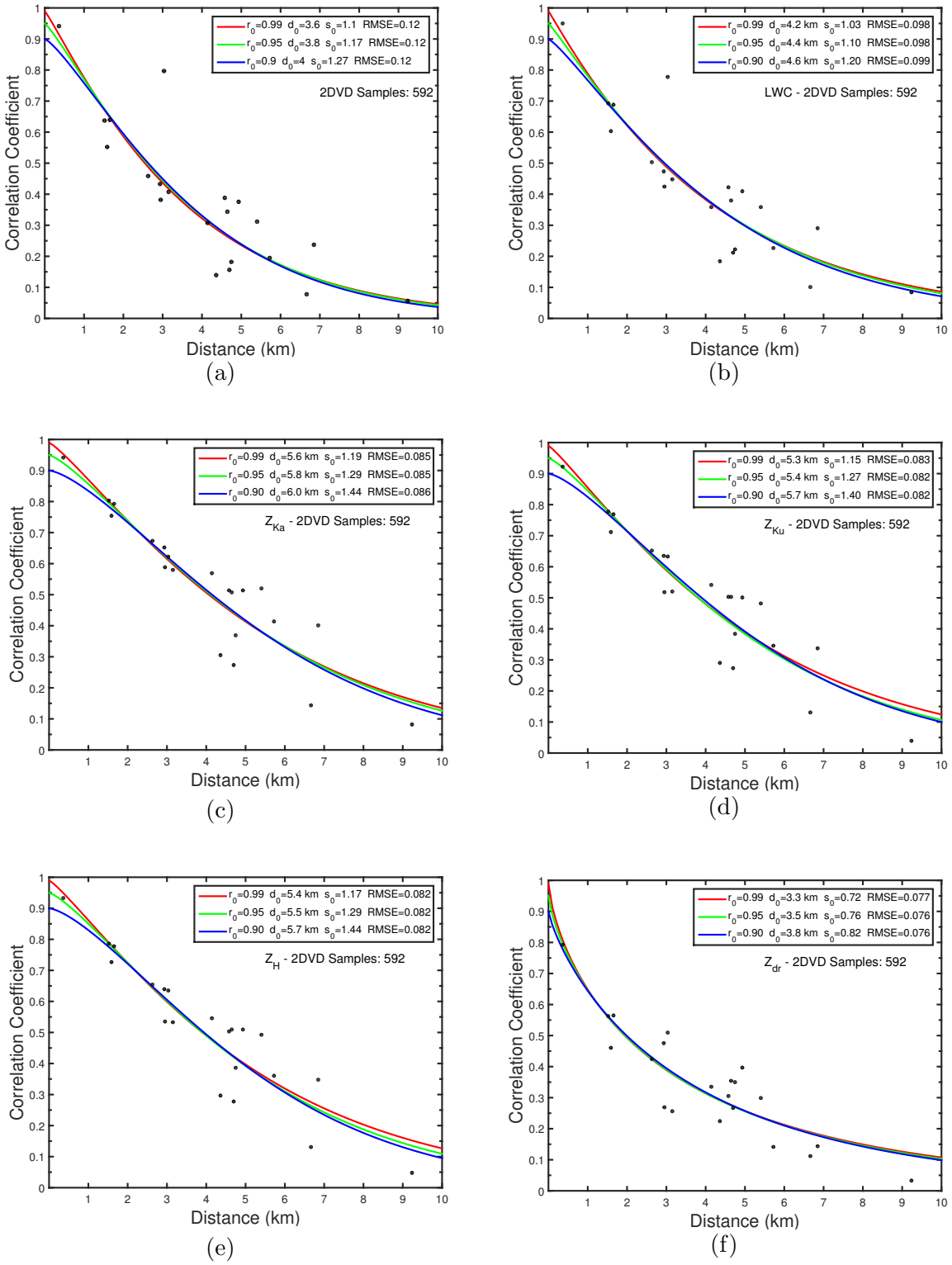

Figure 5.11: Three-parameter exponential function of 2DVD for: (a) RR, (b) LWC, (c) Z_{K_a}, (d) Z_{K_u}, (e) Z_H and (f) Z_{dr} as function of R_0.

Higher correlation distance are obtained for the intercept parameters $N_T{}^*$ and N_W (figures 5.12c- 5.12d). However, the values are different to each other, about 37 km for $N_T{}^*$ and 16 km for N_W. The correlation values are high, if compared with the that of the other parameters, but decrease more quickly with respect the Wallops data. The values indicate correlation distance larger than a satellite footprint or radar pixel, but generally smaller than correlation distance obtained for Wallops dataset. The difference is more marked if the comparison is made with respect to Wallops 2DVD data than Parsivel data. The shape parameter reaches low values, around 0.40 for both $N_T{}^*$ and (d) N_W, and non noticeable changing in RMSE are found. The same features can be observed for $\log(N_T{}^*)$ and $\log(N_W)$ with high correlation distance but very low RMSE values. Very low correlation distances are obtained for the gamma shape parameters derived from $N_T{}^*$ and N_W, that do not exceed 3.4 and 2.7 km for $\mu(N_T{}^*)$ and $\mu(N_W)$ respectively, even if the fit is good (the RMSE moves from 0.07 for $\mu(N_T{}^*)$ to 0.05 about for $\mu(N_W)$.

Figure 5.13 summarizes the results obtained for d_0, s_0 and RMSE as function of nugget parameters. For the most part of the analyzed parameters the correlation distance is lower than 10 km (figure 5.13a), except for the intercept parameters that reach correlation distance up to 40 km. Values of d_0 are not very sensitive to the nugget parameter. More sensitive to the nugget parameter is the shape parameter s_0, generally ranging between 0.40 and 1.20 (figure 5.13b). Both d_0 and s_0 values obtained for Wallops and MC3E data do not show very marked differences to each other. The difference becomes significant for RMSE, especially if the MC3E values (figure 5.13c) are compared with the 2DVD Wallops values (figure 5.6c). The values range between 0.05 and 0.10 for the most of the parameters (figure 5.13c), with a peak at 1.20 for RR, while 2DVD Wallops values are generally lower than 0.05 as well Parsivel values, that only for few parameter exceed the 0.05 value (figure 5.6c).

Anyway, the RMSE values show a good fit of the three exponential function with real data.

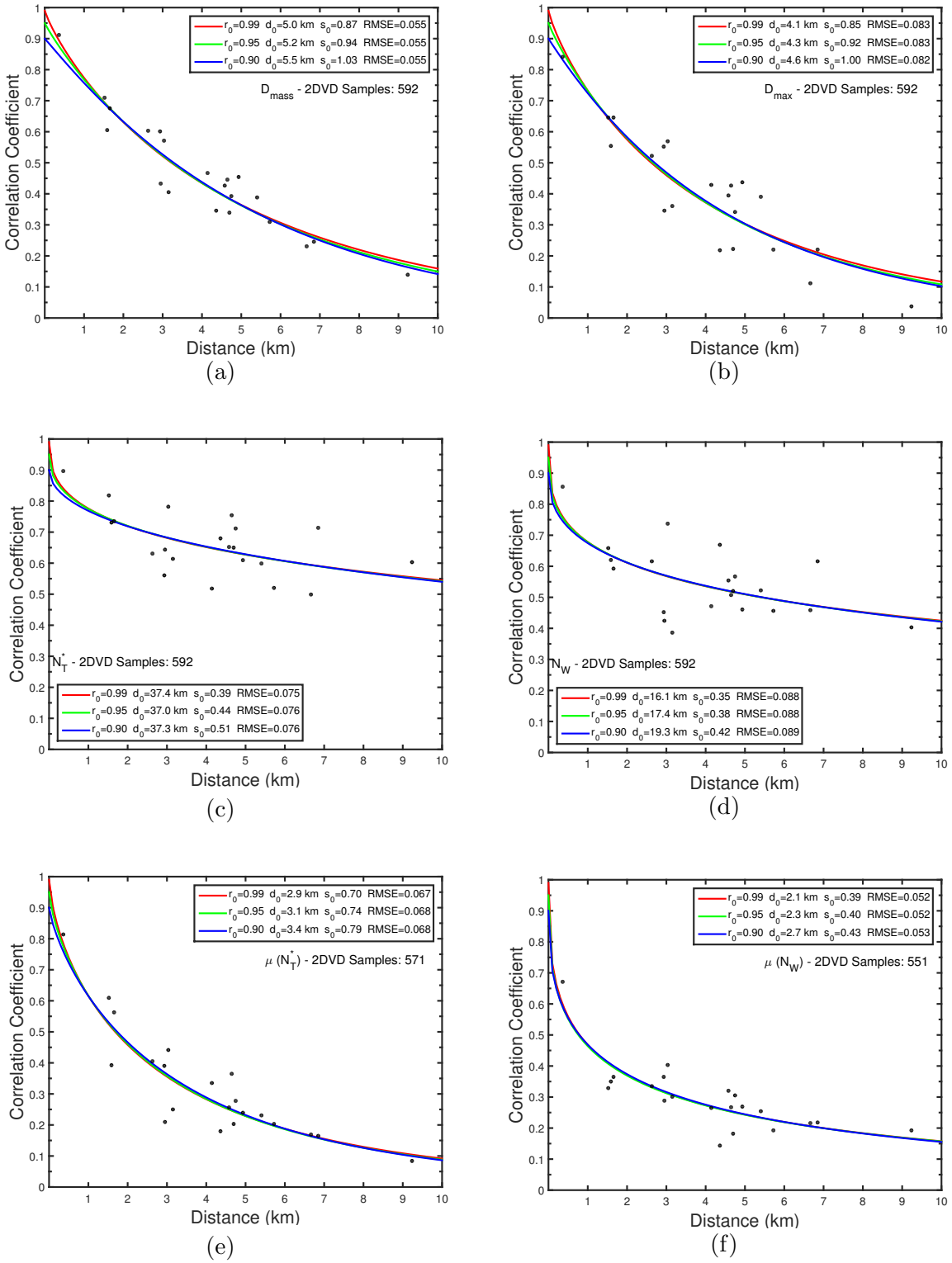

Figure 5.12: Three-parameter exponential function of 2DVD for: (a) D_{mass}, (b) D_{max}, (c) $N_T{}^*$, (d) N_W, (e) $\mu(N_T{}^*)$ and (f) $\mu(N_T{}^*)$ as function of R_0.

The figure 5.14 shows the sensitivity of the parameters of the exponential function to the choice of rain/no-rain thresholds. In general, the dependence on the choice of rain/no-rain threshold is negligible for all three parameters of exponential function. At Z_{K_u}-18dB threshold, the RMSE shows a slight gap, toward both higher and lower values, with respect the other two considered threshold. This does no affect the goodness of fit in either of two cases.

It has to be highlighted that the obtained results, from two different small scale networks with different number and also disdrometer types, show that most of the DSD parameters are correlated within a radar pixel or satellite footprint. Moreover, the dependence on the choice of rain/no-rain threshold is negligible.

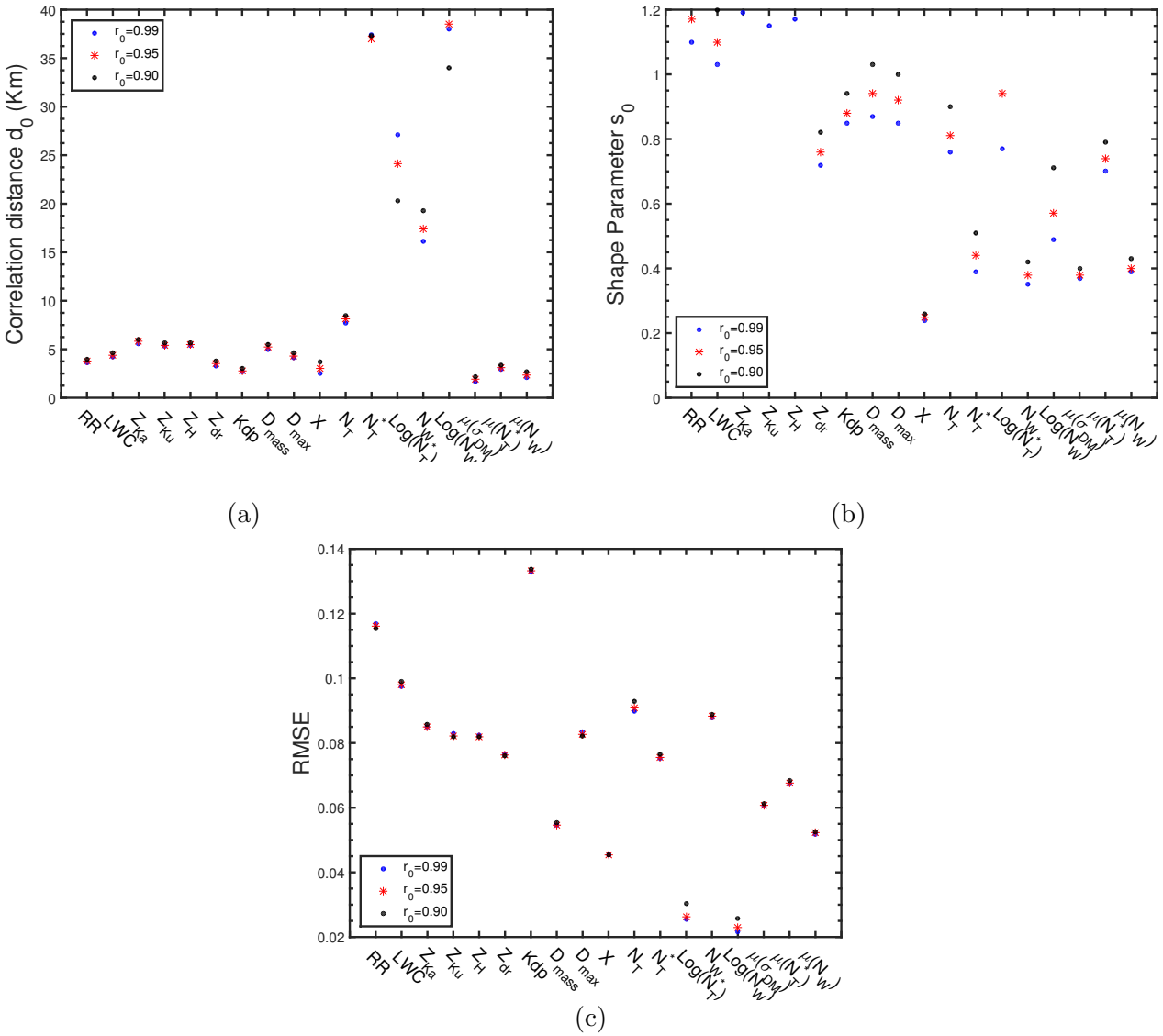

Figure 5.13: The correlation distance d_0 (a), the shape parameter s_0 (b) and the RMSE (c) for all DSD parameters as function of nugget parameter R_0.

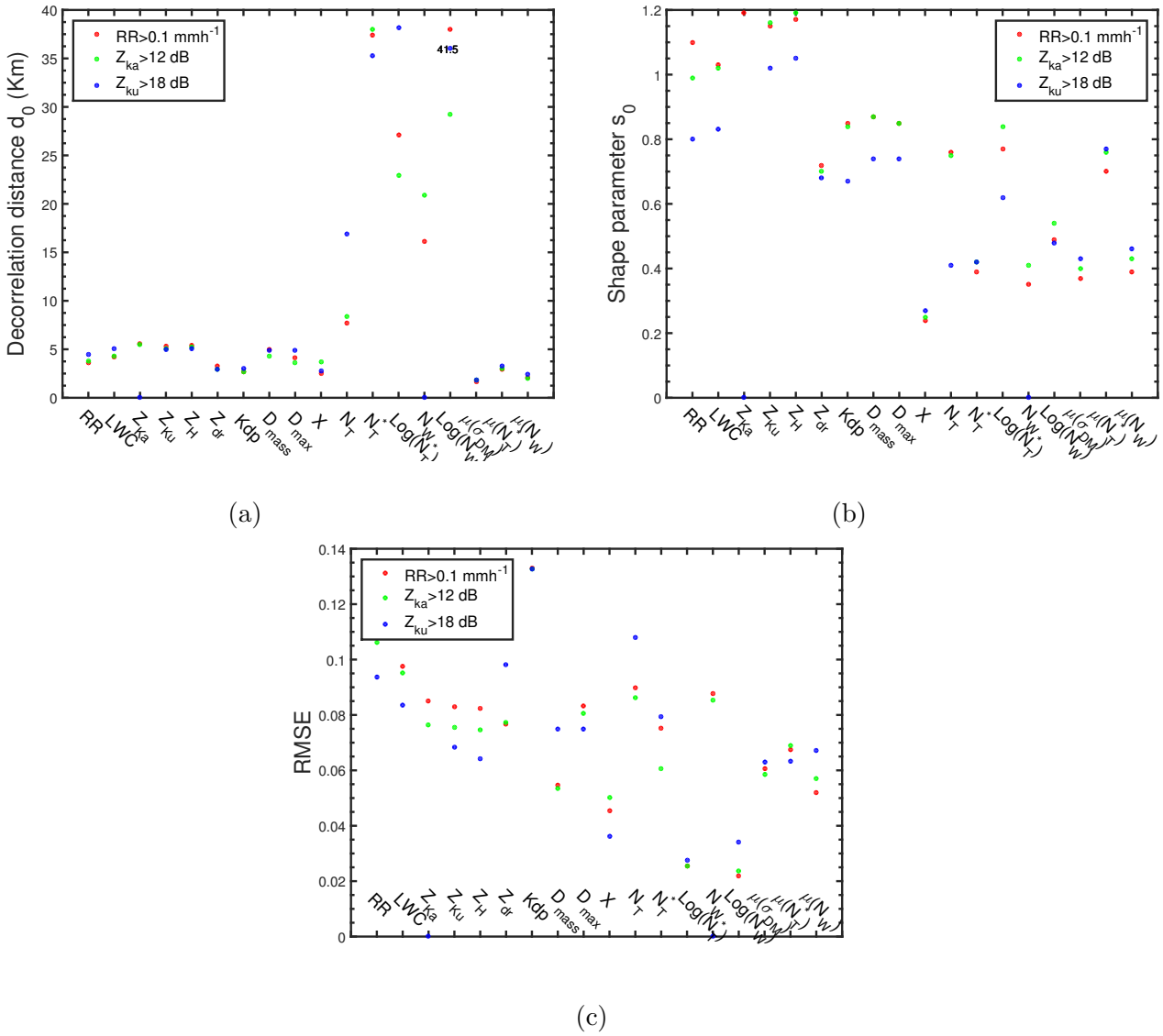

(a) (b)

(c)

Figure 5.14: The correlation distance d_0 (a), the shape parameter s_0 (b) and the RMSE (c) for all DSD parameters as function of nugget parameter threshold considered.

5.3.3 Sensitivity Studies - Partial beam filling

As well as for Wallops data, the three-parameter exponential function has been estimated, only for RR parameter, excluding one of the seven 2DVD when all the instruments exceed the considered threshold. In this case, the exclusion of a site results in six correlation less. The seven three-parameter exponential function obtained are split in the figures 5.15 and 5.16 for a better visualization. The exclusion of one site do not involve any changes in the resulting parameters of the exponential function. The correlation distance ranges always between 3 km and 4 km about for $R_0 = 0.99$ with the shape parameter just over 1 and RMSE around 0.1.

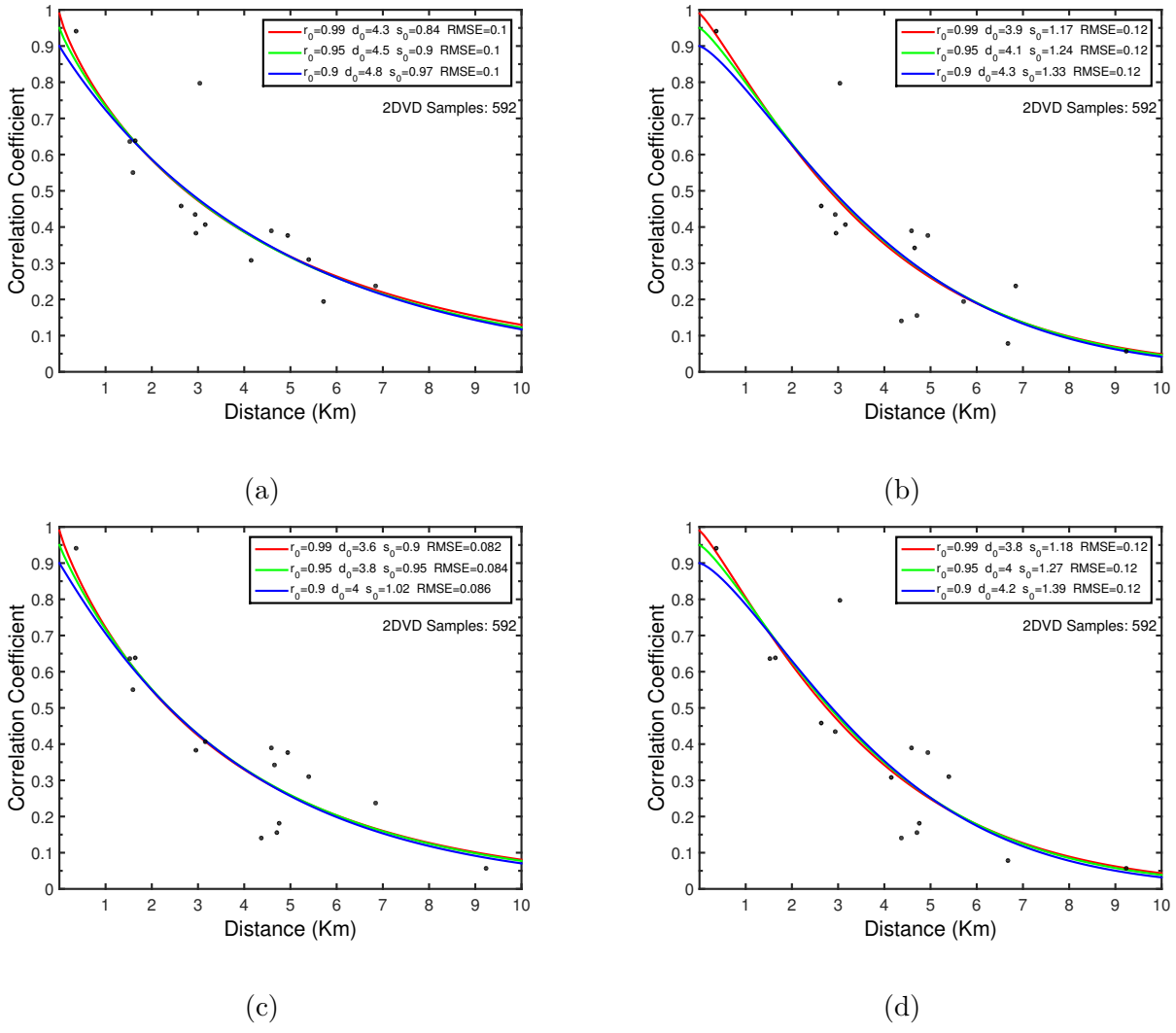

Figure 5.15: The RR three-parameter exponential function excluding one of the seven 2DVD: (a) SN25, (b) SN35, (c) SN36 and (d) SN37.

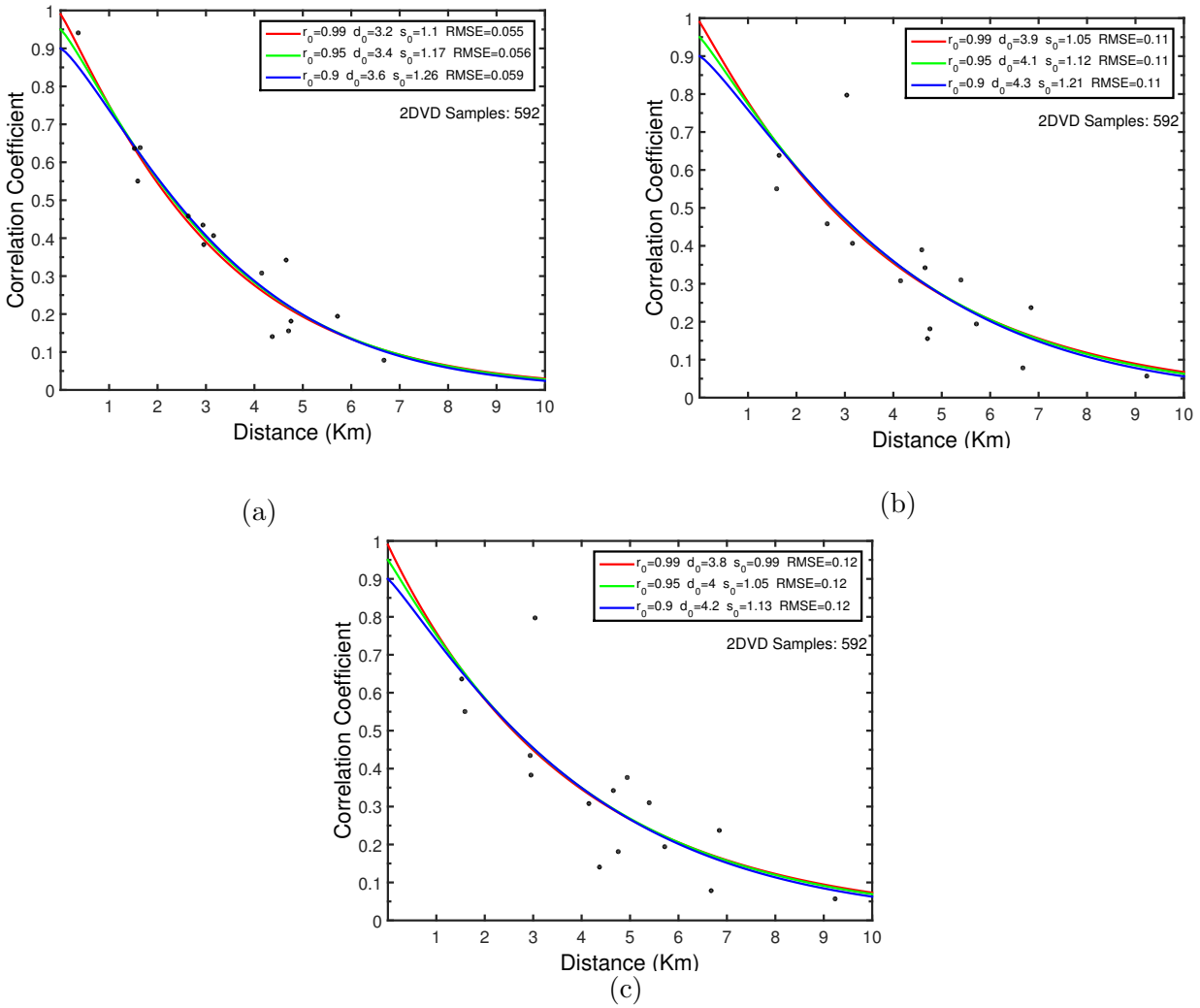

Figure 5.16: The RR three-parameter exponential function excluding one of the seven 2DVD: (a) SN38, (b) SN46 and (c) SN47.

Conclusions and Outlooks

The aim of this work is to describe microphysical characteristics of the structure of natural rain. In particular, the vertical and horizontal, small-scale, variability of DSD is analyzed, focusing on the effects of break-up occurrence, and its evolution to the equilibrium DSD. Unprecedented disdrometric datasets, for the high number and the high quality of instruments employed and also for geographic location (first DSD measurement over 3000 m a.s.l.) have been used to pursue the objectives of this Thesis.

The vertical variability of DSD has been studied thanks to the development of specific algorithms able to detect and characterize both the DSD affected by break-up and the equilibrium DSD. The algorithms are based on the analysis of the Doppler power spectrum and on the analysis of the DSD. The results show a decrease of break-up diameter with altitude, due to the reduction of air density that plays a critical role in the energetic balance of the collision between two raindrops. The analysis indicates that, regardless of the altitude, the collisional break-up occurs if the CKE exceeds 12.2 μJ. The results, together with the detailed analysis of some case study at high altitude (over the Tibetan Plateau), show also that the dominance of the break-up process is required to reach the equilibrium DSD.

The detection and the occurrence of equilibrium DSD and its variability at mid-latitude, are then assessed by using the great amount of high quality disdrometric data avail-

able from the datasets of GV program of NASA-GPM mission. The results show a good agreement between the experimental equilibrium DSD and the equilibrium DSD obtained by theoretical models. The analysis shows also that the equilibrium DSD is mainly reached during convective rain and its dependence on season and latitude (no equilibrium DSD is observed at high latitude - 60°N). The occurrence of equilibrium DSD is a rare event in natural rain (maximum 8% of selected minutes for MC3E data), while an increase is observed if transition situations are considered.

The low correlation between the experimental DSDs and the gamma distribution evidences that the gamma is not the best parametric form to fit the experimental equilibrium DSD. The rain and DSD parameters can be considered an additional indicators to screen out the situations that can not reach the equilibrium DSD.

The horizontal DSD spatial variability is also deeply studied by analyzing the correlation of rain and DSD parameters at small scale. The estimated correlation distance shows that the most of the rain and DSD parameters are correlated within a radar pixel or satellite footprint (generally the integral DSD parameters - RR, Z, LWC, etc. - are less correlated than the non integral DSD parameters - D_{mass}, D_{max}, $N_T{}^*$, etc.). The RMSE evidences a very good fit of the function used with respect the experimental data, indicating a good reliability of data.

The results presented in this Thesis: 1) increase the knowledge of break-up phenomenon and its effect on the DSD up to reach the equilibrium DSD, 2) can be used to improve the parameterization form for DSD affected by break-up and equilibrium DSD occurrence, 3) can be also used in the modeling of cloud and precipitation mechanisms, 4) give reliable indications about the spatial variability of the structure of precipitation within a radar pixel and/or a satellite footprint, 5) have an immediate application to the interpretation of remote sensing measurements to improve precipitation retrieval from radar/satellite measurements, especially for the recently launched DPR in the

frame of GPM mission.

The results obtained in this Thesis lead to the study of many other aspects that can be investigated to better characterize the precipitation. The time evolution of the precipitation with particular emphasis to the time necessary to the break-up to modify the DSD to reach equilibrium DSD can be investigated by using the algorithms proposed here. A new parameterization of DSD affected by break-up and of equilibrium DSD is necessary to improve the remote sensing of precipitation. Finally, a deeper study of DSD spatial variability is needed to have more information about rain structures at small/medium spatial scales, by different techniques and datasets in different season/location.

Acknowledgments

I thank the European Commission (Call FP7-ENV-2007-1 Grant no. 212921) as part of the CEOP-AEGIS project (http://www.ceop-aegis.org/) coordinated by the Universit de Strasbourg that financial supported a part of the work described here, and for the data on the Tibetan Plateau. The TP campaign would have been possible thanks the cooperation of a large number of people: L. Jia (University of Wageningen), J. Colin (University of Strasbourg), Y. Ma, K. Shichang and Y.Wang (ITPCAS), M. Marti and G. Trivellone (ISAC/CNR).

I also thank the HyMeX program that through SOP 1 provided a part of data used for this Thesis.

I acknowledge the NASA Global Precipitation Measurement (GPM) mission ground validation (GV) program, Matthew Schwaller (GPM ground validation manager) and Walter A. Petersen (GPM science manager) for providing most of the datasets used in this work. Thanks to Patrick Gatlin of NASA Marshall Space Flight Center and Matt Wingo of the University of Alabama at Huntsville for maintenance of 2DVD during all field campaigns of the GPM-GV program.

The funding of Bando per soggiorno allestero of the University Institute for Higher Studies, (IUSS - Ferrara 1391) of the University of Ferrara, made possible my visit to NASA-GSFC.

I want to express my gratitude to my tutor Dr. Federico Porcú for his great contribution for my scientific and professional growth and for the guide and the support in reaching the scientific results presented in this Thesis. The open and sincere discussion about topics to investigate, objectives to seek and methods to use, is what I appreciate mostly, besides his high skill and scientific knowledge.
My gratitude also goes to my co-tutor, Dr. Ali Tokay of NASA-GSFC where I spent three matchless months from scientific point of view. His excellent contribution and the introduction in a working environment where the Atmospheric Physics is really taken into account were a fundamental step for the success of this work. I hope to can continue to work with both of them.
A thought of gratittude also goes to Prof. Franco Prodi, which introduced me to the microphysics from my first academic studies.

Outside of the working environment, the only two persons that I have to thank are my parents, which supported me in this as exciting as "risky" choice. I hope to not frustrate their help and their pains.

Bibliography

Alusa, A. and D. Blanchard (1971). Drop size distribution produced by the breakup of large drops under turbulence. *J. Recherches Atmos. VII*(1-9).

Battaglia, A., E. Rustemeier, A. Tokay, U. Blahak, and C. Simmer (2010). Parsivel snow observations: A critical assessment. *J. Atmos. Oceanic Technol. 27*(333-344).

Battan, L. (1973). *Radar observation pf the atmosphere*. University of Chicago press.

Beard, K. (1977). Terminal velocity adjustment for cloud and precipitation drops aloft. *J. Atmos. Sci. 34*(1293-1298).

Beard, K. and H. Pruppacher (1969). A determination of the terminal velocity and drag of small water drops by means of a wind tunnel. *J. Atmos. Sci. 5*(1066-1072).

Bentley, W. (1904). Studies of raindrops and raindrop phenomena. *Mon. Weather Rev. 32*(450-456).

Best, A. (1950). Empirical formulae for the terminal velocity of water drops falling through the atmosphere. *Quart. J. Roy. Meteor. Soc. 76*(302-311).

Blanchard, D. and A. Spencer (1970). Experiments on the generation of raindrop-size distributions by drop breakup. *J. Atmos. Sci. 27*(101-108).

Bloemink, H. and E. Lanzinger. Precipitation type from the thies disdrometer. In *TECO-2005*, Bucharest, Romania.

Cao, Q. and G. Zhang (2009). Errors in estimating raindrop size distribution parameters employing disdrometer and simulated raindrop spectra. *J. Clim. Appl. Meteorol. 48*(406-425).

Cheng, L. and M. English (1983). A relationship between hailstone concentration and size. *J. Atmos. Sci. 40*(204-213).

Ciach, G. and W. Krajewski (2006). Analysis and modeling of spatial correlation structure in small-scale rainfall in central oklahoma. *Adv. Water Resour. 29*(1450-1463).

Clardy, D. E. and C. Tolbert (1961). Electronic disdrometer. *Rev. Sci. Instrum. 32*(916-920).

Feingold, G., S. Tzivion, and Z. Levin (1988). Evolution of raindrop spectra. part i: Solution to the stochastic collection/breakup equation using the method of moments. *J. Atmos. Sci. 45*(3387-3399).

Fernandez-Raga, M., C. Palencia, C. Tomas, A. I. Calvo, A. Castro, and R. Fraile (2011). Rain research with disdrometers: a bibliometric review. *J. HydrometeorAtmos. Meas. Tech. Discuss. 4*(6041-6068).

Foote, G. and P. du Toit (1969). Terminal velocity of raindrops aloft. *J. Appl. Meteorol. 8*(249-253).

Gorgucci, E., V. Chandrasekar, and G. Scarchilli (1995). Radar and surface measurement of rainfall during cape: 26 july 1991 case study. *J. Appl. Meteorol. 34*(1570-1577).

Gunn, R. and G. Kinzer (1949). The terminal velocity of fall water drops in stagnant air. *J. Met. 6*(243-248).

Habib, E. and W. F. Krajewski (2002). Uncertainty analysis of the trmm ground-validation radar-rainfall products: Application to the teflun-b field campaign. *J. Appl. Meteorol. 41*(558-572).

Hou, A. Y., R. Kakar, S. Neeck, A. Azarbarzin, C. Kummerow, M. Kojima, R. Oki, K. Nakamura, and T. Iguchi (2014). The global precipitation measurement mission. *Bull. Amer. Meteor. Soc. 95*(701-722).

Houze, R. A. J. (1993). *Cloud Dynamics*. Academic Press, Inc.

Jaffrain, J., A. Studzinski, and A. Berne (2011). A network of disdrometers to quantify the small]scale variability of the raindrop size distribution. *Water Resour. Atm. 47*(W00H06).

Jones, D. (1959). The shape of raindrops. *J. Meteorol. 16*(504-510).

Joss, J. and A. Waldvogel (1967). A spectrograph for raindrops with automatic interpretation. *Pure Appl. Geophys. 68*(240-246).

Journel, A. G. and C. Huijbregts (1978). *Mining Geostatistics*. Academic Press, London.

Kessler, E. (1969). On the distribution and continuity of water substance on atmospheric circulation. *Meteorol. Monogr. 10*(84).

Knight, N. and A. Heymsfield (1983). Measurement and interpretation of hailstone density and terminal velocity. *J. Atmos. Sci. 40*(1510-1516).

Kruger, A. and W. Krajewski (2002). Two-dimensional video disdrometer: A description. *J. Atmos. Oceanic Technol. 19*(602-617).

Kulieu, M., R. Bennartz, T. Greenwald, Y. Chen, and F. Weng (2010). Uncertainties in microwave properties of frozen precipitation: Implications for remote sensing and data assimilation. *J. Atmos. Sci. 67*(3471-3487).

Laws, J. O. and D. Parsons (1943). The relation of raindrop size to intensity. *Trans. Amer. Geophys. Union 24*(452-460).

Lee, C. K., G. Lee, I. Zawadzki, and K. Kim (2009). A preliminary analysis of spatial variability of raindrop size distributions during stratiform rain events. *J. Appl. Meteorol. Climatol. 48*(270-283).

Li, X., W. Tao, A. Khain, J. Simpson, and D. Johnson (2009). Sensitivity of a cloud-resolving model to bulk and explicit bin microphysical schemes. part ii: Cloud microphysics and storm dynamics interactions. *J. Atmos. Sci. 66*(22-40).

List, R., N. Donaldson, and R. Stewart (1987). Temporal evolution of drop spectra to collisional equilibrium in steady and pulsating rain. *J. Atmos- Sci. 44*(362-372).

List, R., R. Nissen, and F. C. (2009). Effects of Pressure on Collision, Coalescence, and Breakup of Raindrops. Part II: Parameterization and Spectra Evolution at 50 and 100 kPa. *J. Atmos. Sci. 66*(2204-2215).

Löffler-Mang, M. and J. Joss (2000). An optical disdrometer formeasuring size and velocity of hydrometeors. *J. Atmos. Oceanic Technol. 17*(130-139).

Loth, E. (2008). Quasi-steady shape and drag of deformable bubbles and drops. *Intern. J. of Multiphase Flow 34*(523-546).

Low, T. B. and R. List (1982a). Collision, coalescence and breakup of raindrops. part i: Experimentally established coealescence efficencies and fragment size distributions in breakup. *J. Atmos.Sci. 39*(1591-1606).

Low, T. B. and R. List (1982b). Collision, coalescence and breakup of raindrops. Part II: Parameterizations of fragment size distributions. *J. Atmos.Sci. 39*(1607-1618).

Lozowski, E. and A. Beattie (1979). Measurements of the kinematics of natural hailstones near the ground. *Quart. J. Roy. Meteor. Soc. 105*(453-459).

Magarvey, R. and G. Geldart (1962). Drop collisions under conditions of free fall. *J. Atmos. Sci. 19*(107-113).

Mahadi, L. Y., Y. Zulkifli, and Y. Fadhilah (2014). The modelled rain drop size distribution of skudai, peninsular malaysia, using exponential and lognormal distributions. *The Scientifi World Journal Volume 2014*(ID 361703).

Marshall, J. S., R. Langille, and W. M. Palmer (1947). Measurement of rainfall by radar. *J. Meteor. 4*(186-192).

Marshall, J. S. and W. M. Palmer (1948). The distribution of raindrops with size. *J. Meteor. 5*(165-166).

McFarquhar, G. (2004). A new representation of collision-induced breakup of raindrops and its implications for the shapes of raindrop size distributions. *J. Atmos. Sci. 61*(777-794).

McTaggart-Cowan, J. and R. List (1975a). An acceleration system for water drops. *J. Atmos. Sci. 32*(1395-1400).

McTaggart-Cowan, J. and R. List (1975b). Collision and breakup of water drops at terminal velocity. *J. Atmos. Sci. 32*(1401-1411).

Miriovsky, B., A. Bradley, W. Eichinger, W. Krajewski, A. Kruger, B. Neslon, J. Creutin, J. Lapetite, G. Lee, and I. Zawadzki (2004). An experimental study of small scale variability of radar reflectivity using disdrometer observations. *J. Appl. Meteorol. 43*(106-118).

Montero-Martnez, G., A. Kostinski, R. Shaw, and F. Garca-Garca (2009). Do all raindrops fall at terminal speed? *Geophys. Res. Lett. 36*(L11818).

Montgomery, D. N. (1971). Collisions and coalescence of water drops. *J. Atmos Sci. 28*(291-293).

Morrissey, M. L., J. A. Maliekal, J. S. Greene, and J. Wang (1995). The uncertainty of simple spatial averages using rain gauge networks. *Water Resour. Res. 31(8)*(2011-2017).

MRR Instruction Manual (2004). *Micro Rain Radar Physical Basis version 1.3*. MRR Instruction Manual.

Nespor, V., W. Krajewski, and A. Kruger (2000). Wind-induced error of rain drop size distribution measurement using a two-dimensional video disdrometer. *J. Atmos. Oceanic Technol. 17*(1483-1492).

Niu, S., X. Jia, J. Sang, X. Liu, C. Lu, and Y. Liu (2010). Distributions of raindrop sizes and fall velocities in a semiarid plateau climate: convective versus stratiform rains. *J. Appl. Meteorol. Climatol. 49*(632-645).

Porcú, F., L. DAdderio, F. Prodi, and C. Caracciolo (2013). Effects of altitude on maximum raindrop size and fall velocity as limited by collisional breakup. *J. Atmos. Sci. 70*(1129-1144).

Porcú, F., L. DAdderio, F. Prodi, and C. Caracciolo (2014). Rain drop size distribution over the tibetan plateau. *Atmos. Res. 150*(21-30).

Prat, O. and A. Barros (2007). A robust numerical solution of the stochastic collectionbreakup equation for warm rain. *J. App. Meteor. Climatol 46*(1480-1497).

Prat, O. and A. Barros (2009). Exploring the transient behavior of zr relationships: Implications for radar rainfall estimation. *J. Appl. Meteor. Climatol. 48*(2127-2143).

Prodi, F. and A. Battaglia (2002). *Meteorologia: Parte 2^a Microfisica*.

Prodi, F., C. Caracciolo, L. D'Adderio, M. Gnuffi, and E. Lanzinger (2011). Comparative investigation of pludix disdrometer capability as present weather sensor (pws) during the wasserkuppe campaign. *Atmos. Res. 99*(162-173).

Prodi, F., O. Sturniolo, R. Medini, and A. Battaglia (1999). Radar parameter simulation for populations of spherical and non-spherical hydrometeors: dependence on size distributions, shapes and composition. *J. Quant. Spectrosc. Radiat. Transfer 63*(677-699).

Prodi, F., A. Tagliavini, and R. Medini (2000b). Time variability in rainfall events observed by pludix. *Phys. Chem. Earth, Part B Hydrol. Oceans Atmos 25 (1012)*(959963).

Prodi, F., A. Tagliavini, and F. Pasqualucci (2000a). Pludix: an x-band sensor for measuring hydrometeors size distributions and fall rate. *Proc. 13th ICCP* (338-339).

Pruppacher, H. and J. Klett (1969). *Microphysucs of Clouds and Precipitation*. Atmospheric and Oceanic Science Library.

Rodríguez-Iturbe, I. and J. M. Mejía (1974). The design of rainfall networks in time and space. *Water Resour. Res. 10(4)*(713-728).

Schlottke, J., W. Straub, K. Beheng, H. Gomaa, and B. Weigand (2010). Numerical investigation of collision-induced breakup of raindrops. part i: Methodology and dependencies on collision energy and eccentricity. *J. Atmos. Sci. 67*(557-575).

Schonhuber, M., G. Lammer, and W. Randeu (2007). One decade of imaging precipitation measurement by 2d-video-disdrometer. *Adv. Geosci. 10*(85-90).

Sheppard, B. E. (1990). Measurement of raindrop size distributions using a small doppler radar. *J. Atmos. Ocean. Tech. 7*(255-268).

Spilhaus, A. (1948). Raindrop size, shape and falling speed. *J. Meteor. 5*(108-110).

Srivastava, R. C. (1971). Size Distribution of Raindrops Generated by their Breakup and Coalescence. *J. Atmos Sci. 28*(410-415).

Straub, W., K. Behenga, A. Seifert, J. Schlottke, and B. Weigand (2010). Numerical investigation of collision-induced breakup of raindrops. part ii: Parameterizations of coalescence efficiencies and fragment size distributions. *J. Atmos. Sci. 67*(576-588).

Sutton, O. (1942). Investigations on falling drops carried out at the chemical defence experimental station, porton. *Air Minist. Met. Res. 40*.

Tokay, A. and P. Bashor (2010). An experimental study of small-scale variability of raindrop size distribution. *J. Appl. Meteor. Climatol. 49*(2348-2365).

Tokay, A., A. Kruger, W. Krajewski, P. Kucera, and A. Pereira Filho (2002). Measurements of drop size distribution in the southwestern amazon basin. *J. Geophys. Res. 107*(LBA 19-1 - BA 19-15).

Tokay, A. and K. Özrtük (2012). An experimental study of the small-scale variability of rainfall. *J. Hydrometeorol. 13*(351-365).

Tokay, A., W. Petersen, W. Gatlin, and M. Wingo (2013). Comparison of raindrop size distribution measurements by collocated disdrometers. *J. Atmos. Oceanic Technol. 30*(1672-1690).

Tokay, A., R. J. Roche, and P. G. Bashor (2014a). An experimental study of spatial variability of rainfall. *J. Hydrometeor. 15*(801-812).

Tokay, A., D. Wolff, and W. Petersen (2014b). Evaluation of the new version of the laser-optical disdrometer, ott parsivel^2. *J. Atmos. Oceanic Technol. 31*(1276-1288).

Twomey, S. (1965). Computations of rain formation by coalescence. *J. Atmos. Sci. 23*(405-411).

Ulbrich, C. W. (1983). Natural variations in the analytical form of the raindrop size distribution. *J. Clim. Appl. Meteorol. 22*(1764-1775).

Ulbrich, W. and D. Atlas (1982). Hail parameter relations: A comprehensive digest. *J. Appl. Meteor. 21*(22-43).

Villarini, G. and W. Krajewski (2008). Empirically-based modeling of spatial sampling uncertainties associated with rainfall measurements by rain gauges. *Adv. Water Resour. 31*(1015-1023).

Villarini, G., P. Mandapaka, W. Krajewski, and R. Moore (2008). Rainfall and sampling uncertainties: a rain gauge perspective. *J. Geophys. Res. 113*(D11102).

Villermaux, E. and B. Bossa (2009). Single-drop fragmentation determines size distribution of raindrops. *Nature Physics 5*(697-702).

Vivekanandan, J., G. Zhang, and E. Brandes (2004). Polarimetric radar estimators based on a constrained gamma drop size distribution model. *J. Appl. Meteorol. 43*(217-230).

Waldvogel, A. (1974). The n_0 jump of raindrop spectra. *J. Atmos. Sci. 31*(1068-1078).

Weisner, J. (1895). Bietraege zur Kenntniss, des tropi Regens. *K. Akad. Will. Math.-Naturw. Klesse 104*(1397-1434).

Willis, P. and P. Tattelman (1989). Drop-size distributions associated with intense rainfall. *J. of App. Meteor. 28*(3-15).

Zawadzki, I. (1973). Errors and fluctuations of raingauge estimates of areal rainfall. *J. Hydrol. 18*(243-255).

Zawadzki, I. and M. De Agostinho Antonio (1988). Equilibrium raindrop size distributions in tropical rain. *J. Atmos- Sci. 45*(3452-3459).